

Microscopic Perspective of Polymer Glasses During Physical Aging and Mechanical Deformation

A computational study of dynamical
heterogeneity, plasticity, and soft vibrational
modes as the link to the molecular structure.

by

Anton Smessaert

Diplom-Physiker (M.Sc. equivalent), Technical University Berlin, 2010

A THESIS SUBMITTED IN PARTIAL FULFILLMENT OF
THE REQUIREMENTS FOR THE DEGREE OF

DOCTOR OF PHILOSOPHY

in

The Faculty of Graduate and Postdoctoral Studies

(Physics)

THE UNIVERSITY OF BRITISH COLUMBIA

(Vancouver)

April 2015

© Anton Smessaert 2015

Abstract

Microscopic dynamics and mechanical response of polymer glasses are studied in four projects using molecular dynamics simulations of a simple bead-spring model. The first project studies the interplay between physical aging and mechanical perturbation. Structural, dynamical and energetic quantities are monitored in the recovery regime following aging and uniaxial tensile deformation periods. The total engineering strain is found to control a continuous transition from transient to permanent mechanical rejuvenation: After deformation in the pre-yield regime all quantities quickly reset to pre-deformation values, while deformation around the yield point results in the erasure of aging history. Deformation in the post-yield regime, however, drives the system into a distinct thermodynamic state.

In the second project, I introduce an efficient algorithm that detects microscopic relaxation events, which are the basis of aging dynamics and plasticity. I use this technique to calculate the density-density correlations from the spatio-temporal distribution of so called hops in quiescent polymer glasses at different temperatures and ages. Correlation ranges are extracted and I analyze the size distributions of collaboratively rearranging groups of particles. Furthermore, I spatially resolve dynamical heterogeneity (DH) as hop-clusters, and I compare cluster growth, as well as volume distribution during aging with the four-point dynamical susceptibility χ_4 as the established measure of DH.

The third and fourth project use the hop detection technique to investigate the link between relaxation events and local structure. Quasi-localized low-energy vibrational modes, called soft modes, are found to correlate with the location and direction of hops. In the third project, I analyze the temperature- and age-dependence of this correlation in quiescent polymer glasses, and I show that the soft modes are long lived structural features. The fourth project extends the analysis to mechanically deformed polymer glasses. I find that the spatial correlation of hops and soft modes is reduced to pre-aging values after deformation in the strain softening regime. This

Abstract

reveals an additional perspective on mechanical rejuvenation and substantiates the findings from the first project. In the strain hardening regime the correlation increases, and this novel effect is linked to a growing localization of the soft modes.

Preface

A version of chapter 3 has been published as A. Smessaert, and J. Rottler, *Recovery of Polymer Glasses from Mechanical Perturbation*, *Macromolecules* 45, 2928 (2012) [84]. The thesis author was responsible for all of the numerical work as well as the analysis of the results. Prof. Rottler provided the initial idea for the project and he gave suggestions for the analysis and interpretation of the results. The thesis author wrote the manuscript which was then edited by Prof. Rottler.

A version of chapter 4 has been published as A. Smessaert, and J. Rottler, *Distribution of local relaxation events in an aging three-dimensional glass: Spatiotemporal correlation and dynamical heterogeneity*, *Physical Review E* 88, 022314 (2013) [85]. The thesis author initiated the development of the hop detection algorithm and he was responsible for all of the numerical work as well as the analysis of the results. Prof. Rottler provided suggestions for the analysis and interpretation of the results. The thesis author wrote the manuscript which was then edited by Prof. Rottler.

A version of chapter 5 as well as part of chapter 7 have been published as A. Smessaert, and J. Rottler, *Structural relaxation in glassy polymers predicted by soft modes: a quantitative analysis*, *Soft Matter* 10, 8533 (2014) [86]. The thesis author initiated the analysis of the alternative softness field definitions and he was responsible for all of the numerical work as well as the analysis of the results. Prof. Rottler provided the initial idea for the project and he gave suggestions for the analysis and interpretation of the results. The thesis author wrote the manuscript which was then edited by Prof. Rottler.

A manuscript for a peer refereed journal is being prepared from the results in chapter 6. The thesis author was responsible for all numerical work as well as the analysis of the results. Prof. Rottler was involved in the analysis and interpretation of the results. The manuscript is being written primarily by the thesis author with contributions by Prof. Rottler.

Table of Contents

Abstract	ii
Preface	iv
Table of Contents	v
List of Tables	vii
List of Figures	viii
List of Abbreviations	xvii
List of Symbols	xviii
Acknowledgements	xx
Dedication	xxi
1 Introduction	1
1.1 The glass transition	3
1.2 Key features of glassy matter	6
1.2.1 Intermittent microscopic dynamics: the caging effect	6
1.2.2 Non-equilibrium effects: aging	9
1.2.3 Heterogeneous dynamics	13
1.2.4 Soft modes	16
1.3 Polymer glasses under deformation	19
1.4 Objectives of this work	22
2 Simulation and measurement techniques	25
2.1 Polymer model	25
2.2 Molecular dynamics simulations	29

Table of Contents

2.3	Mechanical deformation	33
2.4	Preparing the polymer glass	34
2.5	Interpreting simulation results	37
2.6	Hop detection	38
2.7	Vibrational modes and the softness field	43
2.7.1	Alternative definitions	45
3	Recovery from mechanical deformation	47
3.1	Immediate impact of creep	48
3.2	Recovery of the relaxation time	51
3.3	Recovery of the local structure	57
3.4	Recovery in the potential energy landscape	60
3.5	Recovery after constant strain rate deformation	61
3.6	Conclusions	63
4	Spatio-temporal correlation of structural relaxation events	65
4.1	Statistical properties of hops	67
4.2	Dynamical heterogeneity and clustering of hops	74
4.3	Conclusions	82
5	Soft modes predict structural relaxation	85
5.1	Softness field	86
5.2	Spatial correlation	90
5.3	Directional correlation	94
5.4	Conclusions	96
6	Soft modes and local plastic events during deformation	98
6.1	Correlation between hops and softness field	100
6.2	Examining the strain hardening regime	102
6.3	Conclusions	106
7	Conclusions	108
	Bibliography	116

List of Tables

2.1	Reduced units used in this work in terms of bead diameter a , bead mass m as well as the characteristic energy u_0	29
2.2	Densities in the melt used for the different target temperatures in the glass state. Densities in the left two columns are used in the projects discussed in chapters 3 and 4, while the right two columns are the parameters used in chapters 5 and 6. . . .	34
2.3	Hop identifier function thresholds used for the different target temperatures in the glass state.	41

List of Figures

1.1	(a) Sketch of viscosity as function of temperature when approaching T_g from above. Viscosity is shown on a logarithmic scale and temperature is rescaled such that 1 indicates $T = T_g$. (b) Sketch of volume and enthalpy dependence as function of temperature. Melting and glass transition temperatures are indicated with vertical dashed lines.	3
1.2	(a) Sketch of a typical mean square displacement in glassy matter. Ballistic, caging and diffusive regimes are indicated and cartoons illustrate caging effect and hop process. (b) Square displacement of individual particles measured in simulations of the model polymer glass introduced in section 2.1. Particles mostly vibrate around fixed mean positions and the sharp changes are indications for hops.	7
1.3	Sketch of the potential energy landscape in the glass state. The x-axis represents all configurational coordinates.	10
1.4	Sketch of the PEL in the quiescent state and during external deformation. The x-axis represents all configurational coordinates.	13
1.5	Snapshot of the simulated model polymer glass, see section 2.1. The coloring indicates the squared displacement measured over a time interval $\tau_\alpha/5$, here τ_α is the structural relaxation time. On the right side only the 15% fastest particles are shown. . .	14
1.6	The upper half of the figure shows the eight lowest energy vibrational modes of an example polymer glass simulation, and the participation ratio is indicated above each snapshot. The modes are visualized by their polarization vector fields and coloring indicates depth. (a) Density of states as function of the mode frequency, rescaled to reveal the boson peak. (b) Participation ratio as function of mode frequency. The curve is an average over 20 independent realizations of the system. .	17

List of Figures

1.7	Stress versus strain observed in our polymer glass model. The deformation regimes are indicated (left to right): Elastic, yield, strain softening, strain hardening. The horizontal dashed line indicates steady state flow of a non-polymeric glass.	21
2.1	Visualization of a bead-spring polymer and the filled simulation box. The beads are indicated as spheres.	26
2.2	The LJ-potential between non-bonded beads is given by the blue curve, with energy- and force-shifted corrections in red and orange. For better comparison, the FENE spring potential is scaled by a factor of 10^{-2} and indicated by the green curve.	27
2.3	Sketch that illustrates periodic boundary conditions and minimum image convention. The central square with the blue particles is the simulation box, while image-particles are shown in gray. The arrow illustrates the position update of the particle. The dashed lines indicate the distance vectors from the central particle to all particles within a cut-off (dashed circle).	30
2.4	Mean square internal distance at different times during the equilibration run, as indicated in the legend.	36
2.5	Sample trajectory of a particle and hop identifier function P_{hop} . (a) shows the localization into two cages and the 'hop' is marked by rapid changes in the trajectory (e). Corresponding to this, P_{hop} in (d) is sharply peaked at the transition and the maximum defines the hop time t_{hop} . Plots (b) and (c) are overlays of P_{hop} and the trajectory just before and after the hop (z-comp. only for better visibility). The colored fields (A and B) in both plots indicate the evaluation window for P_{hop} [see eq. (2.5)]. Initial and final positions are calculated from time averages of the trajectory parts that are highlighted as zoom, i.e., (b) initial position (orange) and (c) final position (cyan).	39

List of Figures

- 2.6 Histograms of hop identifier P_{hop} peak heights calculated at glass temperature $T = 0.3$ and time window parameters (order of legend): $(N_{hist}, N_{obs}) = (20, 100), (40, 50), (10, 200), (10, 100), (40, 100)$. The data for the three parameter sets with $t_{eval} = 15$ are nearly identical (blue \diamond overlay other markers). The solid line is an exponential fit of the distribution tail and the dashed line indicates the resulting parameter choice P_{th} . The inset shows the mean square displacement as function of time and P_{th} is indicated by the horizontal line. 42
- 2.7 Distribution of softness in the system $T = 0.3, t_{age} = 750$ for three definitions of the softness field. The softness is rescaled in terms of the mean softness to allow an easier comparison. . . 45
- 3.1 Schematic protocol of the simulation with waiting time period t_w , uniaxial tensile creep (a) or fixed strain rate (b) deformation period t_s , and recovery period t_r 48
- 3.2 Panel (a) shows the creep compliance of a glass with age $t_w = 75000$ for different external stresses σ . The indicated strains are calculated at $t_s = 15000$. Panel (b) shows the intermediate scattering function C_q^S of the perturbed glasses shown in (a) in the recovery regime together with a just-quenched glass (\star). The main graph shows C_q^S just after unloading ($t_r = 0$) and the inset is calculated at $t_r = 75000$. The dashed lines define the α -relaxation time. 49
- 3.3 Evolution of α -relaxation time of a just-quenched “new” glass compared to those of mechanically perturbed glasses in the recovery regime. The glasses are identical in the initial aging regime $t_w = 75000$, the creep time is $t_s = 15000$, and the time regimes are indicated by the dashed lines. Other results from simulations with these parameters are shown in fig. 3.2. 51
- 3.4 Relaxation time dynamics of unperturbed glasses with a range of wait times $10^3 \leq t_w \leq 10^5$ in a double logarithmic plot. The continuous black line is the “generic” aging dynamics τ_α^0 and in the inset (axes: τ_α over t_r) I show the shift of τ_α with increasing t_w . The main graph shows a data collapse with t_r measured in units of glass age $t_a = t_w$ and τ_α being rescaled by $\tau_\alpha^0(t_a)$. The dashed lines are guides to the eye. 52

List of Figures

3.5	Relaxation time of mechanically perturbed glasses in the recovery regime. The coloring represents the total strain at time of unloading. The continuous line indicates the generic aging dynamics and the dashed lines are guides to the eye.	53
3.6	Sketch of possible recovery paths of the α -relaxation time. Line (o) is the path of an unperturbed glass and lines (a)-(c) are possible paths of glasses after mechanically perturbation. The diagonal black line indicates the generic aging dynamics. .	55
3.7	Percentage change of the rescaled average Voronoi cell volume with respect to the “generic” value $\Delta\langle V_v \rangle = \langle V_v(t) \rangle - \langle V_v^0(t_a) \rangle$ at glass age $t_a = t_w + t_s$. Shown in the main graph is the evolution of mechanically perturbed glasses in the recovery regime. The coloring represents the total strain at time of unloading. The continuous line indicates the generic aging dynamics and the dashed lines are guides to the eye. The inset shows the evolution of the average cell volume for just-quenched glasses and the black line is a logarithmic fit that yields the generic aging dynamics.	56
3.8	(a) Difference in the coordination number $\Delta\langle c_v \rangle = \langle c_v(t) \rangle - \langle c_v^0(t_a) \rangle$, (b) triangulated surface order parameter $\Delta\langle S \rangle = \langle S(t) \rangle - \langle S^0(t_a) \rangle$, and (c) evolution of the eigenvalue difference $\Delta\langle \lambda_{1,3} \rangle = \langle \lambda_{1,3}(t) \rangle - \langle \lambda_{1,3}^0(t_a) \rangle$. All three quantities are rescaled percentage changes with respect to the “generic” value at glass age $t_a = t_w + t_s$. The coloring represents the total strain at time of unloading (see e.g., fig. 3.7). The continuous line indicates the generic aging dynamics and the dashed lines are guides to the eye.	58
3.9	Percentage change of the difference between the minimized potential energy of a mechanically perturbed glass $\Delta\langle u_{min} \rangle = \langle u_{min}(t) \rangle - \langle u_{min}^0(t_a) \rangle$ and the “generic” behavior at glass age $t_a = t_w + t_s$. Shown is the evolution of the potential energy landscape in the recovery regime. The coloring represents the total strain at time of unloading. The continuous line indicates the generic aging dynamics and the dashed lines are guides to the eye.	60

List of Figures

3.10	Evolution of (a) α -relaxation time, (b) Voronoi cell volume, and (c) inherent structure energy in the recovery regime after deformation with constant strain rates $\dot{\epsilon} = 10^{-5}$ and 10^{-6} and two waiting times (glass age $t_a = t_w + t_s$). (b) and (c) are percentage changes as defined in fig. 3.7 and fig. 3.9, and the coloring represents the total strain at time of unloading. The continuous lines indicate the generic aging dynamics and the dashed lines are guides to the eye.	62
4.1	Snapshots of a single configuration showing (a) all particles and (b) only those particles that are in the middle of a hop. There are only four hops at that time step and their positions are highlighted by arrows. (c) shows all hops that are detected in a time window of $3000\tau_{LJ}$. The configurations are taken from a glass at $T = 0.2$ and age $t_a = 20000$	66
4.2	(a) Distribution of persistence time τ of cages at three temperatures. The solid lines indicate power laws. (b) Distribution of hop distances $ d $, i.e., the distance between old and new cage. Exponential fits are indicated by the solid lines and the vertical dashed lines indicate $\sqrt{P_{th}}$ and $2\sqrt{P_{th}}$ for the respective temperatures; see legend in panel (a). Error bars in both plots are smaller than the markers and are omitted for visibility.	67
4.3	The hop frequency f_{hop} in units $1/\tau_{LJ}$ over the duration of the simulation run in a log-log plot. Solid lines indicate power-law fits with exponents μ given in the legend.	68
4.4	Hop displacement autocorrelation for three glass temperatures at age $t_{age} = 10^5$ (a) as function of number of hops separation and (b) as histogram, that is calculated using normalized displacement vectors ($T = 0.25$ and age as above) and reveals an anisotropy in the direction of consecutive hops. The lines are guides to the eye.	69

4.5	(a) Probability density surface for spatio-temporal separation of two different hopping particles based on Eq. (4.3) for a glass at $T = 0.25$ and $t_{age} = 10^5$. The color scale is logarithmic (scale at the top-right corner) and the dashed lines indicate integration limits used to calculate the one-dimensional probability functions (b,c). Center plots show the probability function of (b) separation and (c) time delay between hops for $T = 0.2$ (blue \bigcirc), $T = 0.25$ (green ∇), and $T = 0.3$ (red \diamond) at the same age. The gray vertical dashed lines in (b,c) illustrate the correlation ranges and the black dashed curve in (b) indicates the radial distribution function. (d) Probability density surface following Eq. (4.3) for the same glass as the left panel, but with r^* calculated from initial position (at the origin) to the final position of the second particle after the hop. The color scale is again logarithmic.	71
4.6	Size distribution of cooperatively rearranging particles. The main panel shows distributions at six ages for a glass at temperature $T = 0.3$; see legend in fig. 4.7. The inset shows the size distribution of three glasses at age $t_{age} = 10^5$ and temperatures $T = 0.2$ (blue \bigcirc), 0.25 (green ∇), 0.3 (red \diamond). Both plots have the same axes ranges, and the solid black lines indicate $P(s) \propto \exp(-s)$	74
4.7	The top panel shows the number of caged, i.e. not yet hopped, particles N_{caged} averaged over independent simulations as a function of time for six glass ages. The four-point susceptibility χ_4 shown in the bottom panel is calculated from the variance of N_{caged} , eq. (4.4).	75
4.8	Snapshots of the growth of a single cluster over time. The particles are visualized at their initial positions (before the hop) and the coloring indicates depth. The plot on the right shows the cluster volume of 15 example clusters as a function of time. Examples were recorded at glass age $t_{age} = 10^5$	77
4.9	Mean cluster volume (top) given as a fraction of the total simulation box volume and the number of simultaneous clusters (bottom) as a function of time. Results for six ages are shown, see legend in fig. 4.7. The insets show data collapse when time is rescaled by the time of the χ_4 peak.	78

List of Figures

4.10	Mean hole volume (top) given as a fraction of the total simulation box volume and the number of simultaneous holes (bottom) as a function of time. Results for six ages are shown, see legend in fig. 4.7. The insets show data collapse when time is rescaled by the time of the χ_4 peak.	79
4.11	Collection of cluster volume distributions of a glass at age $t_{age} = 10^5$ measured at various times in double-log scale. Each distribution is plotted in the $V_{cl}-p(V_{cl})$ plane and placed along the t axis according to the size of the time window used for the cluster analysis. The back wall shows an overlay of distributions at small times in a single plane. I include data at times $\lesssim 10^3$ (up to and including the second blue distribution) and the same colors as the separate distributions are used to indicate the origin of the data points. The solid line on the back wall indicates a power law with exponent -2 . The black solid curve on the floor wall indicates χ_4 as a function of time.	80
4.12	Main panel shows the mean fractal dimension of the hop clusters over time for six ages, see legend in fig. 4.7. The inset shows data collapse when time is rescaled by the time of the χ_4 peak.	82
5.1	(a) Snapshot of the softness field. The right side shows only the 10% softest regions and the solid black spheres (size equals particles) indicate the first 100 hopping particles detected after the measurement of the softness field. (b) Distribution of the softness field for three temperatures and three ages. Error bars are omitted and smaller than the symbols.	86
5.2	Autocorrelation of the softness field for three temperatures (a-b) and three ages (c-d). Panel (a)[(c)] shows C_a as function of time, and the dotted lines indicate the ISF for the same temperatures [ages]. Panel (b)[(d)] shows C_a as function of number of hopped particles N_h , with dotted lines again indicating the ISF and dashed lines mark when 50% of the system has hopped. Error bars are omitted and smaller than the symbols.	87

5.3	Number of holes as a function of the fraction of hopped particles. The sketch illustrates the definition of a hole: a continuous volume (green) that is surrounded by the union of spheres that approximates the cages that hopping particles have escaped and are “broken”. The dashed line indicates 50% of the system has undergone rearrangements, and the solid lines are guides to the eye. See fig. 5.1 for a legend.	89
5.4	Cross-correlation between softness field and cumulative map of hopped particles (a) as function of time and (b) as function of number of hopped particles. See fig. 5.1 for a legend, and error bars are omitted and are smaller than the symbols. . . .	91
5.5	(a) Probability of a particle to hop as function of its softness, rescaled by the average hop probability. The solid lines indicate the averaged saturation probability and the dotted line is a guide to the eye. Success rate of predicting hops to occur in the softest regions of the system Θ (b) as function of coverage fraction of the softest region f and (c) as function of time rescaled to the number of hopped particles at constant coverage fraction of $f = 30\%$. The solid lines in (b,c) indicate the success rate based on randomly chosen regions and the dashed line indicates 50% of the system has undergone rearrangements. To evaluate (a) and (b) the first 100 (1%) hopping particles after the softness field measurement were used. See fig. 5.1 for legend, and error bars are omitted when smaller than symbols.	93
5.6	Directional correlation between softness field and hops (a) as function of softness and (b) as function of time rescaled to the number of hopped particles. The dashed line indicates 50% of the system has undergone rearrangements and the hop direction is measured as the vector between initial and final position of the particle. To evaluate (a) the first 100 (1%) hopping particles after the softness field measurement were used. See fig. 5.1 for a legend.	95

List of Figures

6.1	Snapshots of the system are shown at beginning (a) and end (b) of the deformation. To better visualize polymer configurations, 15 polymers are colored separately and only beads that belong to these polymers are displayed on the right side of the simulation box. (c) Stress along the deformation axis as function of total strain. Vertical colored lines indicate the investigated deformation states $\epsilon = 0.0, 0.04, 0.1, 0.5, 1.0, 2.0, 3.0, 4.0$ and the inset shows the peak at the yield point in more detail.	99
6.2	(a) Fraction of hops in soft spots as function of the coverage fraction of soft spots measured in three deformation regimes: elastic ($\epsilon = 0.0$), strain softening ($\epsilon = 0.1$), and strain hardening ($\epsilon = 4.0$). The dashed line indicates no correlation. The evolution of the predictive success rate reached at $f = 0.3$ is shown during aging (b) and during deformation (c) - the dashed lines are guides to the eye.	100
6.3	Mean inherent structure energy during aging (a) and (b) as function of strain during deformation.	102
6.4	(a) Mean participation ratio as function of eigenfrequency. (b) Mean participation ratio of all N_m modes used for the softness field calculation as function of total engineering strain.	103
6.5	Relative change observed during deformation in the strain hardening regime. Lines are guides to the eye.	105

List of Abbreviations

DH	Dynamical Heterogeneity
FENE	Finitely Extensible Nonlinear Elastic bead-spring polymer model
IC	Iso-Configurational ensemble
ISF	self-part of the Intermediate Scattering Function
LJ	Lennard-Jones
LT	Langevin Thermostat
MD	Molecular Dynamics
MSD	Mean Square Displacement
MSID	Mean Square Internal Distance
NHT	Nosé-Hoover Thermostat
NPT	Isothermal-isobaric ensemble
NVT	Canonical ensemble
PEL	Potential Energy Landscape
PMMA	. . .	Poly(methyl methacrylate), e.g. Plexiglas
PVC	PolyVinyl Chloride
SD	Square Distance

List of Symbols

H	Hessian matrix
N	number of particles
N_h	Number of hops
N_{hist}	hop detection trajectory length parameter
N_m	number of vibrational modes parameter
N_{obs}	hop detection observation frequency parameter
P	Participation ratio
P_{hop}	hop identifier function
P_{th}	hop identifier function threshold parameter
T	temperature
T_g	glass transition temperature
U	potential energy
$U_{LJ}(r)$. . .	6-12 Lennard-Jones potential
$U_{bond}(r)$. . .	bond potential
$U_{pair}(r)$. . .	pair potential
Δt	time step
χ_4	dynamical susceptibility
\mathbf{d}	hop displacement vector

List of Symbols

\mathbf{e}	polarization vector
\mathbf{r}	location in space
\mathbf{r}_{final}	final particle position after a hop
\mathbf{r}_{init}	initial particle position before a hop
\mathcal{P}	pressure
ω	angular frequency
ϕ	softness field
ρ	density
σ	stress
τ_α	structural α -relaxation time
$\theta(f)$	predictive success rate of a softness field
f	coverage fraction of soft regions
m	particle mass
r_c	cut off distance
t	time
t_a, t_{age} . . .	glass age
t_s	deformation time
t_w	waiting time
t_{eval}	hop detection time window parameter
u_0	Lennard-Jones energy well depth
u_{min}, U_{IS} . .	Inherent structure energy

Acknowledgements

I thank my supervisor Prof. Jörg Rottler, who helped me develop and shape my professional abilities as a researcher and physicist. I am grateful for his guidance and continuous support as well as for giving me the freedom to develop my own research path and goals.

I thank the members of my supervisory committee James Feng, Scott Oser and Steven Plotkin for providing feedback and benchmarks during the progression of my research. My fellow graduate students and friends Darren Smith, Amanda Parker and Kevin Whyte I thank for sharing in the frustrations and successes of my research.

For creating and maintaining the balance between professional and personal life that allowed me to succeed in my research and to draw strength and happiness from my work, I thank my heroes and unicorns. For unending support, love and friendship I thank Lisa Hansen, my sister Angela as well as my parents Ute and Pieter Smessaert.

To my dad.

Chapter 1

Introduction

In the last century a new class of matter has become a key manufacturing material: polymer glasses also known as plastics. Rather than a specific material, the term encompasses a variety of polymeric substances in the same state, the *glass state*. The glass state is reached by cooling a glass forming material below a characteristic, material dependent temperature that is called glass transition temperature T_g . Already in Roman times glassy matter was known in the form of silicon dioxide SiO_2 (window glass), which is a non-polymeric glass former. Nowadays, especially plastics are of enormous industrial importance, because they are cheap and easy to produce. Furthermore they are easy to manipulate and shape by exploiting the glass transition, i.e. a plastic is poured at high temperature into a mold and then cooled to below T_g . Polymers are often used in the glass state, and prominent examples of polymer glasses are Nylon, PVC (polyvinyl chloride) and other carbon-hydrogen based polymers like polyethylene (shopping bags), polyethylene terephthalate (PET - bottles) and polypropylene (PP - packaging). Not all plastics are in a purely glassy state, but rather contain a degree of crystallinity which is introduced to alter the material characteristics. Although the use of glasses permeates most manufacturing branches, from water bottles and office material to medical instruments, houses and aircraft, our knowledge of the physical processes governing this state of matter is limited. Key mechanical properties like the yield point and onset of flow in Plexiglas (PMMA) or for a rope of Nylon are estimated largely based on empirical data. In contrast to crystalline solids, we do not have access to theoretically well founded models for the propagation and interaction of structurally weak regions. We can therefore not predict at which location in the material critical failure might occur. Furthermore, the mechanical properties of glasses are changing over time. A plastic ruler will be more brittle in a year than it is today, yet we have no model that describes this evolution. This lack of knowledge stands in the way of confidently utilizing glasses in critical components. Furthermore, a better understanding of the

processes in the glass state might give new insights into how to better utilize or manipulate the material in order to perform new tasks or increase its efficiency.

This thesis explores the underlying physics in the glass state. This is done by analyzing the molecular scale behavior of a model polymer glass using computer simulations in order to better understand the processes that control macroscopic behavior like mechanical failure under load. In this chapter I introduce the conceptual ideas behind our current understanding of the glass state and I highlight how this work contributes to open questions. My research focuses on the more specific class of polymer glasses, which includes industrially important plastics, and I elaborate on specific properties of polymer glasses.

Plasticity of glasses Why can we not describe plasticity in glasses in the same way in that we understand it in crystalline solids? Crystalline solids undergo a phase transition upon cooling below the melting temperature, where the material rearranges on the atomic level into an ordered lattice. This long-range order is the basis of our understanding of plasticity in crystalline solids: The solid is modeled as a set of springs that attach atoms to their lattice positions. Elastic, or reversible deformation is understood as small displacement of atoms from the lattice and the resulting pendulum-like relaxations back towards the equilibrium positions. Plastic, or irreversible deformation is modeled as irregularities in the long-range order, where the lattice symmetry is locally broken. An example is the so called edge-dislocation which is located at the end of an extra plane that extends into one half-space and ends in the lattice. The dynamics and interactions of such dislocations is the basis of plasticity models in crystalline solids.

The glass state combines rigidity and mechanical properties of a solid with a liquid-like structure. Unlike the freezing phase transition, the glass transition is not accompanied by long-range ordering on the atomic scale. In the liquid phase, molecules do not form a lattice but are essentially randomly distributed in space. Repulsive and attractive interactions (typically van-der-Waals interactions) drive the self-organization of nearest neighbor shells, yet this ordering is only short-range. As the temperature is lowered below T_g , the material vitrifies and the molecules are stabilized in their current positions, i.e. the liquid-like structure is preserved in the solid. The transition is discussed in more detail below, yet the key point is that without long-

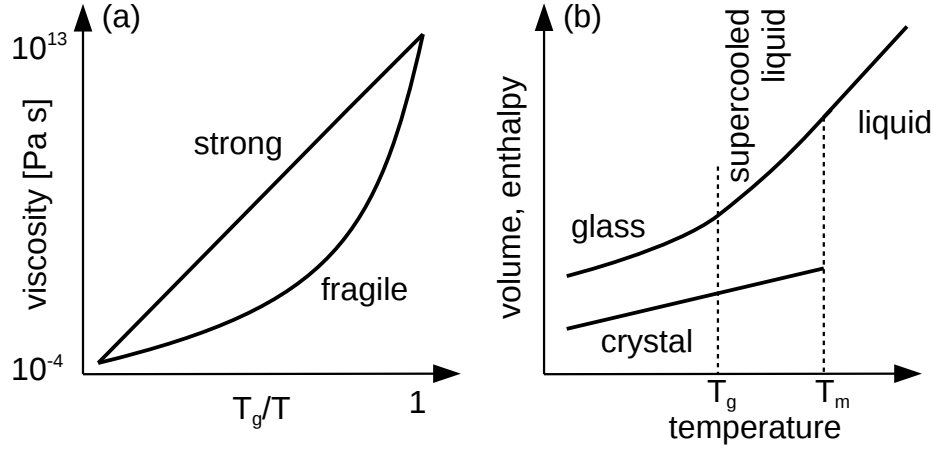


Figure 1.1: (a) Sketch of viscosity as function of temperature when approaching T_g from above. Viscosity is shown on a logarithmic scale and temperature is rescaled such that 1 indicates $T = T_g$. (b) Sketch of volume and enthalpy dependence as function of temperature. Melting and glass transition temperatures are indicated with vertical dashed lines.

range order plastic deformations can not be understood in terms of lattice defects. In the absence of a lattice, dislocations can not be defined and the machinery developed for plasticity in crystalline solids is incompatible with glasses. Indeed, being mechanically solid without long-range ordered structure is the defining feature of a larger class of matter called *amorphous solids*. Polymer glasses are amorphous solids with disorder on the nanometer scale, yet the term also encompasses systems like colloidal glasses, foam and granular media that show disorder on the micro- to millimeter scale and even tectonic faults on the kilometer scale. All of these systems share a common dynamical behavior that arises from the absence of long-range order, and the results of this work can be considered in the context of this broader class of materials.

1.1 The glass transition

The glass state is reached by cooling a glass forming material in the liquid state to the glass transition temperature T_g . As the temperature approaches

1.1. The glass transition

T_g one observes a sharp increase in the viscosity by many orders of magnitude. The viscosity η measures the ability of a liquid to withstand shear or tensile stress, i.e., a liquid with large viscosity requires a large force to create flow. The glass transition is reached when the viscosity is $10^{13} Pa \cdot s$, which is an empirical threshold that originates from practices in (silicon based) glass-manufacturing. Figure 1.1(a) shows a sketch of the viscosity as function of temperature in a semi-log plot. The temperature is rescaled by T_g and decreases from left to right. Two types of behavior are distinguished: measurements of SiO_2 show exponential behavior $\eta \propto \exp(E/k_B T)$ known from thermally activated processes with activation energy E , k_B is the Boltzmann constant and T is the temperature. Materials that exhibit such Arrhenius-type behavior are known as strong glass formers. The second type of behavior is called super-Arrhenius, because of the much steeper increase of viscosity near T_g . It can be expressed with the empirical Vogel-Tammann-Fulcher equation $\eta \propto \exp[E/(k_B T - k_B T_0)]$ [14]. The polymer glasses discussed in this work fall into this category and are called fragile glass formers. The reasons underlying this separation of glasses into two groups is still actively discussed [30]. The research presented in this work is based on a fragile glass model and generalization of the results to strong glass formers should be considered with care. However, the exponential dependence on temperature indicates that thermally activated processes dominate structural relaxation and molecular mobility in the glass state.

Fingerprints of the glass transition can also be found in the change of slope at T_g of state variables like volume or enthalpy, as sketched in fig. 1.1(b). A similar behavior is known from first order phase transitions, yet the change of slope is continuous in case of the glass transition. The crossover between liquid- and glass-slope is often used to measure the glass transition temperature more accurately than based on the threshold criterion of the viscosity.

The glass state is furthermore characterized by another feature: thermodynamic state variables and mechanical properties are time- and history dependent. In other words, a glass is not in thermodynamic equilibrium, because its state variables and properties do not fluctuate around history independent mean values, but change over time. Glasses are therefore non-equilibrium systems, and an alternative definition of the transition is when a glass former falls out of equilibrium upon cooling. The reason behind the loss of equilibrium is connected to the mobility in the glass state. As the mobility decreases, the system requires more time to find its optimal configuration, which is the thermodynamic mean. Upon cooling, the system is eventually

unable to keep up with the change of this optimal configuration, and the non-equilibrium glass state is reached. This inability to fully explore the accessible configurational- or phase-space is also called a loss of ergodicity.

Glass forming matter To understand which materials are glass formers, it is helpful to contrast the glass transition with the freezing transition of crystalline solids, where the material self-assembles on an atomic-scale lattice. This process is driven by the existence of an ordered ground state that is energetically favorable. The crystallization transition is sharp, meaning that a material will rapidly transform from an unordered liquid-like structure with high entropy to an energetically stable structure with long-range order. In contrast to this, the glass transition is not sharp, but gradual. Motion on the atomic scale rapidly slows until diffusion becomes negligible and the atoms become arrested in their current position. The unordered liquid-like structure is essentially frozen into the material. Why does the competition between a thermally stabilized high entropy state and an energetically favorable ground state not result in a first order phase transition? There are two possible reasons: Either such a ground state does not exist, or the temperature quench is too rapid for the system to self-assemble onto a lattice before the existing structure is frozen into place. Both possibilities are observed in nature. From a simplified perspective, order on a lattice requires that the atomic interactions are dominated by a common length scale, which becomes the lattice constant. Systems that exhibit two competing length scales might not have a well defined ground state, because no structure supports both lengths at the same time. Many polymers are such systems, with PMMA (Plexiglas) being a prominent example: the average distance between bonded monomers along the backbone is different from the average distance between non-bonded monomers. Systems without a well defined crystalline state are also known as good glass formers, because the cooling rate does not play a critical role. However, it is also possible to produce a glass state by cooling a liquid so rapidly, that crystallization is avoided. Without going into any detail, the dynamics in first order phase transitions requires nucleation processes. If nucleation does not occur, then one can cool a liquid to temperatures below its freezing point and the system is then called a *supercooled liquid*. Nucleation is a diffusive process, and further cooling reduces the mobility on the atomic scale and stabilizes the supercooled state. The glass transition occurs when the system falls out of equilibrium (see above).

Nature of the glass transition Whether the glass transition can be understood as a phase transition is still a matter of active research [11]. One prominent microscopic theory is the Mode Coupling Theory [6, 39, 60] (MCT), which predicts a phase transition from a liquid state to a dynamically arrested state where particles stop diffusing and an amorphous density profile is frozen into the system. The theory successfully describes aspects of the super-cooled liquid state, yet it fails to predict the Arrhenius-type behavior of the viscosity near T_g and leads to a complete freezing of the particle configuration which is clearly not observed in glasses. Another view on the glass transition is given by kinetically constrained models (KCM, see ref. [23] for a review), which assume that dynamical activity is facilitated by nearby dynamical events and does not decay or arise spontaneously. This leads to the propagation of dynamical activity via “defect-like” objects, and such models successfully predict Arrhenius and super-Arrhenius behavior [11]. One drawback of this approach is the lack of a microscopic derivation and that details of different models lead to different qualitative features. Rather than adding to the debate about the glass transition, this thesis aims at exploring the physical processes inside the glass state. I use computer simulations as numerical experiments that give insights into dependences, correlations and trends, rather than providing accurate quantitative estimates for specific material properties.

1.2 Key features of glassy matter

1.2.1 Intermittent microscopic dynamics: the caging effect

The molecular scale dynamics in glasses is separated into three regimes: the ballistic regime at small timescales, the caging regime at intermediate timescales and the diffusive regime at large timescales. Figure 1.2(a) shows a sketch of the mean square displacement (MSD) $\langle(\mathbf{r}(t_0) - \mathbf{r}(t_0 + t))^2\rangle$ typically found in glasses, which measures the average distance that a particle moves between times t and t_0 . The three regimes are visible in the MSD: On very small time scales a particle moves ballistically, like a free particle in empty space. When the corresponding length scales become of order the mean separation between particles, the MSD flattens to a plateau that is characteristic for the glass phase. On these intermediate time scales a par-

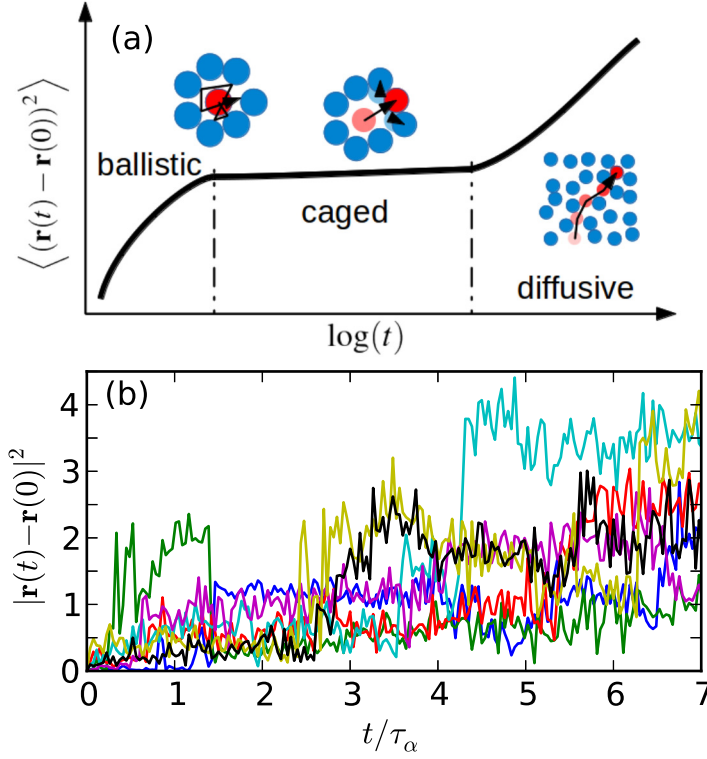


Figure 1.2: (a) Sketch of a typical mean square displacement in glassy matter. Ballistic, caging and diffusive regimes are indicated and cartoons illustrate caging effect and hop process. (b) Square displacement of individual particles measured in simulations of the model polymer glass introduced in section 2.1. Particles mostly vibrate around fixed mean positions and the sharp changes are indications for hops.

ticle becomes effectively trapped by the shell of neighboring particles due to high densities at which the glass state exists. The surrounding particles act as a cage that confines the motion of the central particle to vibrations around the center of that cage. The left sketch in fig. 1.2(a) illustrates this caging effect. The MSD does not increase until such times at which the probability for a particle to escape the cage becomes large. The cage escape is a cooperative and therefore nonlinear process, since particles in the neighboring shell have to move to “open the cage” and allow the central particle to escape. I call this process a *hop* and it is visualized in the central sketch of fig. 1.2(a). Indications of particle hops can be found by inspecting the squared displacement (SD) of individual particles as shown in fig. 1.2(b). The SD has long periods of relative stagnation where the particle is caged that are interrupted by short jumps in the SD that correspond to hop events. Finally, at large time scales diffusive motion is realized as a succession of hops as indicated by the right sketch in fig. 1.2(a). The MSD shows a departure from the caging plateau and a transition to diffusive behavior. Vollmayr-Lee [95] was amongst the first to exploit this essential feature of glassy dynamics to measure the effective motion in a glass and additional detection methods for hops have been developed for glasses [98] and amorphous solids [19]. A key technical accomplishment of this work is the improvement of an algorithm introduced by Candelier et al. [19] such that hop events can be measured during computer simulations of glasses with high spatial and temporal resolution. The hop detection algorithm is discussed in detail in section 2.6.

Hop events are of key importance not only to explain motion in glasses on the molecular scale, but they are also vital for the understanding of plasticity in glasses. Plastic events are irreversible rearrangements of atoms driven by external mechanical deformation. Vibrational motion is not irreversible, since particles merely fluctuate around their static mean positions and stay within their cages. Plastic events can therefore be identified with changes of the configuration of cages. Assuming that in the presence of external load the molecular mobility remains dominated by the caging effect, then hops are elementary plastic events. In the absence of mechanical load, hop events play the role of structural relaxation events. The non-equilibrium nature of the glass state drives such structural relaxation processes to evolve the glass into more favorable configurations. Hops are therefore also at the center of non-equilibrium effects discussed in the next section.

1.2.2 Non-equilibrium effects: aging

Matter in the glass state is not in thermodynamic equilibrium but slowly changes its properties over time. The state of the system can therefore not be described by a small set of equilibrium mean values and fluctuations around them. The reason for this is that the molecular mobility has decreased so far at the glass transition, that the glass can not explore phase space sufficiently to relax to the equilibrium state. Instead, the glass becomes trapped in the transition, resulting in a non-equilibrium system that is slowly evolving towards an “ideal equilibrium state”. This time evolution is known as physical aging, which I simply call *aging* in this work. The dynamical processes governing aging are of key importance in making reliable predictions of mechanical and other properties of glasses. Aging effects are particularly important in polymer glasses [48]: density, enthalpy and yield stress increase, but also the tendency for shear localization, which limits the lifetime to failure. The seminal work of Struik [88] is a striking presentation of the age-dependence of mechanical properties of polymer glasses. Struik performed creep experiments (deformation at constant stress, see next chapter) of PVC, Polystyrene (PS) and other glass samples repeatedly over up to four years of time between measurements. He measured the creep compliance, which is the ratio of strain over the applied stress as function of time during deformation. His results show a shift towards smaller compliance for increasing age, indicating that the plastics become stiffer with time. The size of this shift increases like a power law with the glass age with exponent $\lesssim 1$. In other words, the mechanical response of plastic to an applied stress is strongly dependent on aging effects.

Potential energy landscape To better understand the aging dynamics and indeed glasses themselves, it is helpful to describe the state of a system as a single point on a potential energy landscape (PEL). For a 3D system with N particles, the landscape exists in a $dim = 3N + 1$ dimensional space with the added dimension representing the current total potential energy. A sketch of the PEL in the glass state is shown in fig. 1.3. While all particles are trapped in their respective cages in the glass state, the system resides in a minimum in the PEL. A hop event changes the local structure and with it the potential energies, which moves the system from the original minimum into another one close by. In the remainder of this work, I will therefore refer to hops as structural relaxation events.

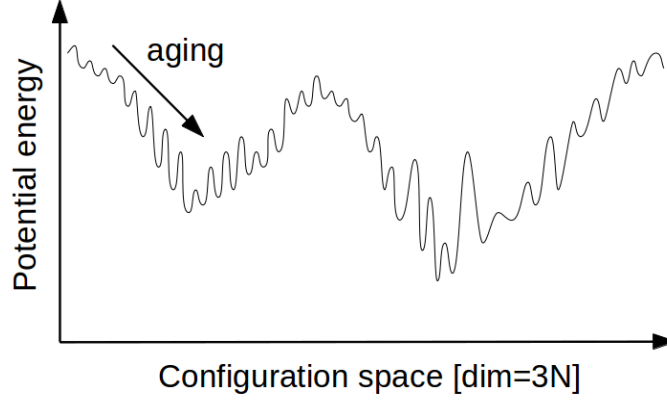


Figure 1.3: Sketch of the potential energy landscape in the glass state. The x-axis represents all configurational coordinates.

Let us first consider the glass transition from the PEL perspective. At temperatures much higher than T_g , the kinetic energy in the system is higher than the maxima in the PEL and the system is in a molten state. When cooled into the supercooled regime $T \gtrsim T_g$, then the kinetic energy becomes so low, that the system evolves by switching from one minimum to another. The transitions are thermally activated, which corresponds to the exponential behavior of the viscosity discussed above. At the glass transition, the thermal transition processes become sufficiently unlikely, that the system can no longer fully explore the PEL on experimental timescales. The dynamics become non-ergodic and the system gets stuck in the process of finding the equilibrium state. It falls out of equilibrium and the material transitions into the glass state. The key reason for this is that the PEL is very rough, with many metastable states. Inside the glass state, the process of finding the equilibrium state continues, and the glass evolves towards regions of lower potential energy and higher barriers between minima. This non-equilibrium relaxation is the process causing physical aging or structural recovery.

Hops are processes that allow the system to explore the PEL. Vollmayr-Lee et al. [95, 97] measured hops directly during aging, finding indications for an age- and temperature-independent distribution of persistence times, i.e. times that particles stay inactive between hops. A closer investigation of the persistence time distribution by Warren and Rottler in quiescent poly-

mer and binary Lennard-Jones glasses [98] showed that physical aging can indeed be explained by hops on the microscopic level. They found that the persistence times are distributed following a broad power-law with exponent $\mu \sim -1.3$ that is independent of the age of the glass. Power-law distributions with exponent $\mu > -2$ have no defined mean value, which means that with increasing number of draws from the distribution the mean persistence time increases. During the evolution of a glass, hops occur and because of the broad power-law, the persistence times increase with age. This increase was directly measured as an age-dependence of the time distribution until the first hop occurs for all particles. Hops are therefore intimately tied to the non-equilibrium dynamics in glasses. Chapter 4 explores the hop process beyond the level of persistence time distributions by investigating spatio-temporal correlations between hop events.

Mechanical rejuvenation Mechanical deformation interacts with the intrinsic relaxation (non-equilibrium) dynamics in complicated ways. Numerous experimental observations [40, 42, 88, 89, 93] suggest that the history of a glass can be altered by mechanical perturbation in such a way that the material appears “younger”. Struik [88] observed that after a short but strong tensile stress pulse the creep compliance of PVC was shifted towards larger compliance, thereby effectively reversing effects of previous aging. Continued measurements of the creep compliance after the pulse then showed shifts with age that paralleled that of a younger glass. Mechanical deformation therefore “erased” part of aging and the phenomenon was coined *mechanical rejuvenation*. However, the nature and extent of this “mechanical rejuvenation” in aging glasses is far from understood and frequently debated [64]. The often reported [22, 59, 61, 74, 75] increase of molecular mobility during deformation may suggest that a “material clock” has indeed been turned back, but the thermodynamic state reached by mechanical perturbation could be very different from that of a younger version of the system. In other words, is the “rejuvenated” state indeed comparable to a younger glass with measures other than molecular mobility and mechanical response?

Studies of “rejuvenation” tend to differentiate between deformation in the sub-yield regime, without yield and material flow, and the post-yield regime, where the material has undergone significant plastic deformation (the deformation regimes are discussed in more detail further below). Experiments in the sub-yield regime observe an initial increase in mobility in agreement

with the rejuvenation hypothesis [56, 79]. However, further measurements after the deformation has ended indicate that the mobility rapidly returns to values found for samples of the same age but without deformation. It is therefore often suggested that sub-yield deformation only transiently perturbs the aging dynamics and that there is no direct connection to changes in material properties [56, 64, 79]. For post-yield deformation, however, rejuvenation experiments on polystyrene [42] and polycarbonate [40, 93] glasses demonstrate more convincingly thermal and yield stress properties akin to a much younger glass.

A recent series of experiments on PMMA glasses by Lee and Ediger provides a very detailed insight into the interaction between physical aging and plastic deformation [57, 58]. These authors employ a fluorescence microscopy technique that permits measurements of segmental relaxation times simultaneously with macroscopic mechanical response [59]. During creep deformation at constant stress, they report significantly increased molecular mobility indicating partial erasure of aging. Full erasure, however, was only found in the post-yield regime [57]. In a second study the authors went a step further, and performed detailed measurements of the molecular mobility in the recovery regime immediately following the deformation. Their results qualitatively distinguish two impacts of deformation: in the pre-flow regime only transient rejuvenation effects were found and relaxation times rapidly returned to those of an unperturbed glass. Glasses that experienced post-yield however, did not return to the pre-deformation aging trajectory but were instead found to age in the same way as a thermally quenched glass. Based on these observations, the authors suggest that mechanical rejuvenation does occur in the post-yield regime [58].

From the perspective of PEL, mechanical deformation can be abstracted to a tilting of the PEL towards the directions that are favored by the deformation, see fig. 1.4. Barriers and adjacent minima are lowered by the deformation, and the system evolves away from the aging-favored region in the PEL. At the end of the deformation, the tilt is removed and the system state in the PEL is in a region with higher potential energy and lower barriers. The system again begins evolving towards lower minima and higher barriers, which manifests as a renewed physical aging. Simulations that investigate the energy landscape of strongly deformed glasses [54, 62, 92] find indeed that the material has been taken to higher inherent structure energies. The deformation trajectory, however, does not appear to return the material to the exact same position on the landscape as a thermal quench, but rather to a

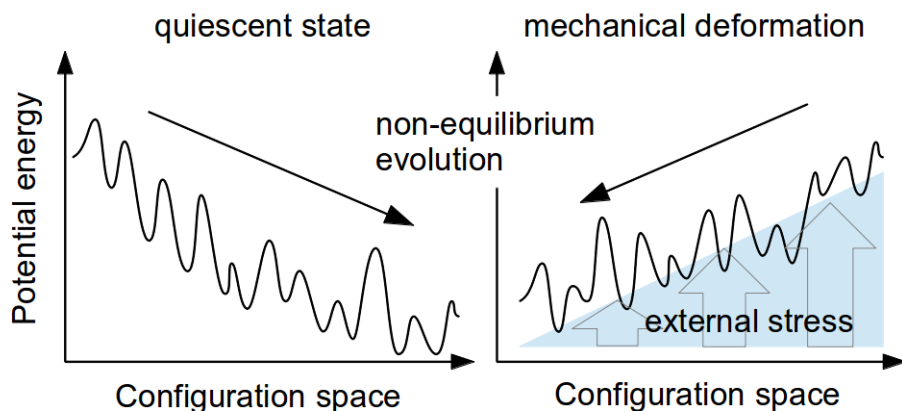


Figure 1.4: Sketch of the PEL in the quiescent state and during external deformation. The x-axis represents all configurational coordinates.

different state. One focus of this work is to investigate mechanical rejuvenation on the molecular level, see chapters 3 and 6. Computer simulations give access to experimentally inaccessible quantities like local structural features, and this allow me to quantify whether a deformed system is indeed similar to an equivalent glass of less or equal age. Furthermore, I explore the transition from transient to permanent impact of deformation, and which deformation variable is governing this transition.

1.2.3 Heterogeneous dynamics

The rapid slowing of the molecular mobility that is observed when approaching the glass transition is accompanied by a characteristic feature that further distinguishes glasses from other systems. Instead of a homogeneous distribution of the particle mobility known from simple liquids, the dynamics of glasses are spatially heterogeneous. This *dynamical heterogeneity* (DH) manifests itself as “fast” regions in a glass sample with dynamics that are orders of magnitude faster than other “slow” regions which are only a few nanometers apart [34]. Computer simulations are especially useful to visualize DH, and fig. 1.5 shows an example snapshot of a simulated model polymer glass with squared displacements indicated by the coloring (blue - slow, red - fast). In the left half of the simulation box one can see large areas of blue particles

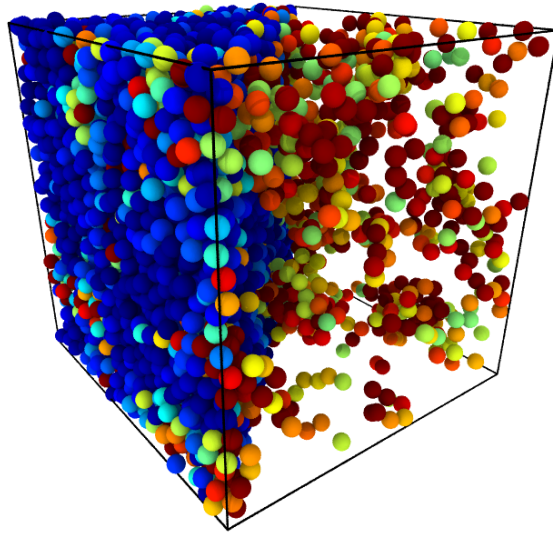


Figure 1.5: Snapshot of the simulated model polymer glass, see section 2.1. The coloring indicates the squared displacement measured over a time interval $\tau_\alpha/5$, here τ_α is the structural relaxation time. On the right side only the 15% fastest particles are shown.

indicating slow regions with a largely static structure. In the right half of the simulation box I only show the 15% fastest particles. One can see that these fast particles are clustered in small fast regions that undergo substantial structural relaxation.

Dynamical heterogeneity in glasses is now supported by a large number of experimental [9, 28, 34] as well as computational results [24, 47, 51, 53], and it explains the non-exponential structural relaxation observed for example in fluorescence microscopy experiments [57, 58]. It furthermore directed the search for growing correlation effects near T_g away from static correlation functions known from conventional phase transitions, towards the study of dynamical correlations. Since fast and slow particles spatially cluster into distinct groups, such a correlation is present in glassy systems. First insights were gained by computational studies that monitored a subset of “fast” particles, which revealed a heterogeneous distribution and string-like cooperative motion [33, 51]. The dynamical correlation itself can be directly measured by calculating a four-point correlation function [7] that quantifies how many pairs of particles (two points in space) have moved by a similar distance over the same time window (two points in time). This allows the measurement of a “dynamical susceptibility” χ_4 [9, 53]. Strikingly, it was found that χ_4 increases when T_g is approached from above, indicating a growing correlation length. Diverging correlation lengths play a crucial role in phase transition theory, and it is currently believed that the correlation between the dynamics of particles is driving the glass transition [11, 12]. The measurement of the distribution of hops gives a direct picture of DH on the level of structural relaxation events. In chapter 4, I explore this strategy of observing DH with high spatial and temporal resolution. My analysis focuses on the spatio-temporal correlation between hops and the aggregation of hops into clusters that as the system evolves grow until percolation and bulk structural relaxation is reached.

As a consequence of DH, structural relaxation is concentrated in some regions and this has important consequences for the plasticity of glasses. Microscopic plastic events are structural relaxation events under external load, and one can therefore expect that DH leads to a partition of glassy matter into soft (hard) regions of fast (slow) particles. In order to create predictive models of plasticity, it is of key importance to understand what makes certain regions structurally weaker than others. In crystalline solids, the location of plastic events is intimately tied to the local structure via dislocations. In glasses, the situation is less clear and conventional structural indicators like

local geometric order (e.g. hexagonal order) or density fail to correlate well to the location of plastic events. A first key insight that a link between structure and dynamics exists was found using computer simulations in the iso-configurational (IC) ensemble [101]. In the IC ensemble the kinetic contribution to DH is suppressed by averaging displacement maps over many realizations of a system, where the same spatial configuration of particles is used with velocities drawn at random from the appropriate Maxwell-Boltzmann distribution. The resulting map for the propensity of motion, that depends only on the initial structure, still shows DH with distinct regions of high and low likelihood of particle rearrangements. In a later study [13] the relative impact of kinetic and structural contributions to DH were quantified for a simple metallic glass model, and the results suggest that on the order 50% of DH is linked to the molecular structure. Understanding this link in terms of structural features that determine whether a certain region in a glass is soft or hard is an important open question that is addressed in chapter 5 for the case of a quiescent glass during aging and in chapter 6 for a glass under load.

1.2.4 Soft modes

A promising candidate of a structural feature that predicts relaxation and plastic events are anomalous modes in the vibrational spectrum of glasses. The vibrational motion in a solid can be understood in terms of normal modes, which describe vibration of particles as a collective dynamical process. The modes are given by the eigenmodes of the Hessian

$$H_{(\mathbf{r}_i)_k(\mathbf{r}_j)_l} = \frac{\partial^2 U(\{\mathbf{r}_i\})}{\partial(\mathbf{r}_i)_k \partial(\mathbf{r}_j)_l} . \quad (1.1)$$

Here $U(\{\mathbf{r}_i\})$ is the interaction potential between pairs of particles and $(\mathbf{r}_i)_k$ is the k 'th component of the position of particle i . For the case of crystalline solids the Debye model describes vibrational modes via planar waves known as phonons. In amorphous solids the description of vibrational properties is less understood, yet the spectrum characteristically shows an excess of modes in the low energy range when compared to the Debye expectation, which is known as the Boson peak [18, 31, 83, 105].

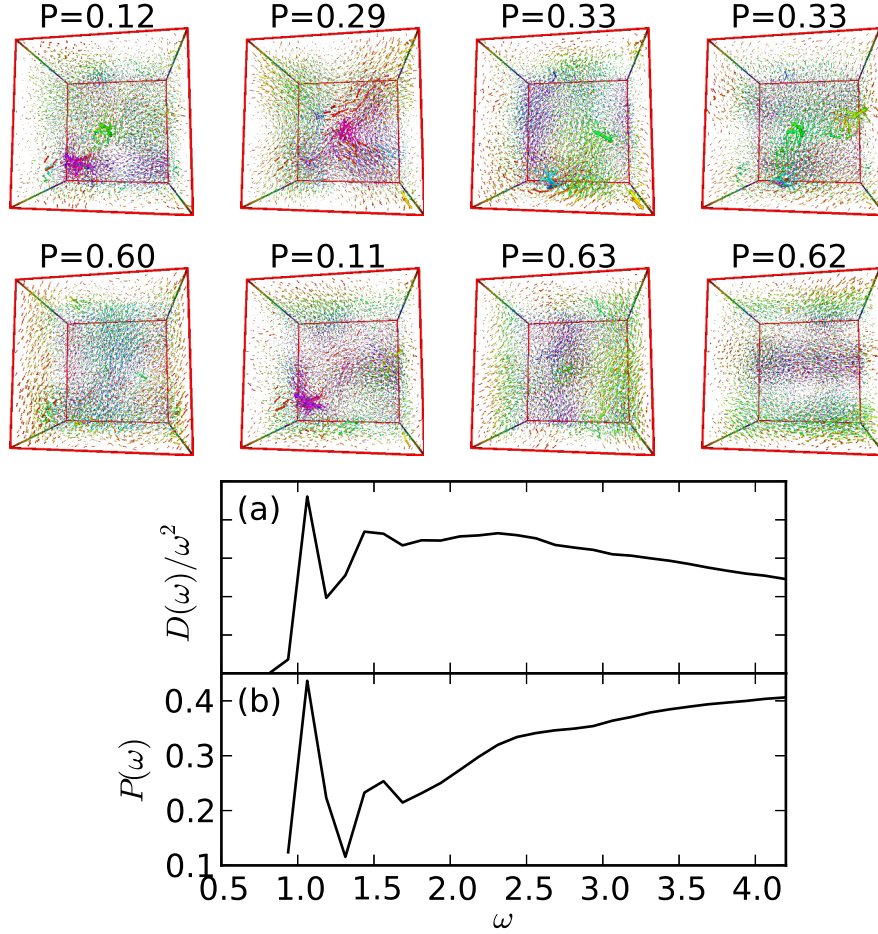


Figure 1.6: The upper half of the figure shows the eight lowest energy vibrational modes of an example polymer glass simulation, and the participation ratio is indicated above each snapshot. The modes are visualized by their polarization vector fields and coloring indicates depth. (a) Density of states as function of the mode frequency, rescaled to reveal the boson peak. (b) Participation ratio as function of mode frequency. The curve is an average over 20 independent realizations of the system.

Already over 20 years ago [55], it was observed that many modes in the low energy range are “quasi-localized” in the sense that most of the activity is concentrated on a small number of particles that are clustered in space. This is caused by the scattering of phonons at the local structure. Quasi-localized modes have been observed in a variety of glasses and super-cooled liquids in computer simulations [55, 80] as well as experiments [18], and they have been linked to the Boson peak [31]. At the top of fig. 1.6 I show the eight lowest energy eigenmodes of an example simulation of a polymer glass (details of the model and simulation are discussed in the next chapter). In each mode j a particle i is represented by the polarization vector $\mathbf{e}_j^{(i)}$, which is the projection of the eigenvector on the degrees of freedom of particle i . The extent of localization of mode j can be calculated via its participation ratio

$$P_j = \frac{\left(\sum_{i=1}^N (\mathbf{e}_j^{(i)})^2\right)^2}{N \sum_{i=1}^N (\mathbf{e}_j^{(i)})^4} ,$$

where N is the total number of particles in the system. A small participation ratio indicates that only few particles are active and that the mode is therefore quasi-localized, while $P = 0.66$ is the value found for a planar wave. The participation ratio of each mode in fig. 1.6 is indicated above the snapshot, and localized as well as planar waves are shown. Figure 1.6(a) shows the density of state rescaled by the Debye-expectation, and the Boson peak is located at $\omega \sim 2.3$. The peaks at $\omega \sim 1.0$ and $\omega \sim 1.3$ are due to the finite volume of the simulation box. In fig. 1.6(b) I show the participation ratio as the function of eigenfrequency, and one can see that the low participation modes are concentrated before and around the Boson peak and that at higher frequencies the modes are less localized.

In 2008, Widmer-Cooper et al. [102] reported a qualitative spatial correlation between quasi-localized, low energy vibrational modes or *soft modes* and irreversible molecular rearrangements. The correlation was observed in computer simulations of a metallic glass model in 2D [102] and 3D [103] in the supercooled regime, and it successfully linked DH to a structural property, the vibrational spectrum. Further indications for this link were found in simulations of hard spheres [16], a kinetically constrained lattice glass [3], a quasi-statically sheared binary glass in 2D [90], and experiments on colloidal glasses [27]. Indications for the reason behind the connection of curvature in the PEL (Hessian, see eq. (1.1)) and particle rearrangements in amor-

phous solids was identified in a study of a binary mixture of jammed packed spheres [104]. The authors found that soft modes identify the directions in the PEL with the lowest-energy barriers to adjacent minima. This links the harmonic vibrational modes to the anharmonic event of particle rearrangements.

A striking quantitative correlation between soft modes and rearrangement events was verified by Manning and Liu [63] in a study from 2011. In computer simulations of a metallic glass in 2D they calculated the lowest energy vibrational modes and derived a map of “soft spots” by overlaying the most participating particles of the lowest modes in a binary map. Starting from the initial configuration for which the soft spot map was calculated, the authors applied very small step strains using a quasi-static shear protocol while monitoring where the first rearrangements would occur. They found that the rearrangements strongly overlap with one of the identified soft spots. This correlation between soft spots and plastic events was recently found to hold also in thermal binary glasses at finite shear rate [81]. Chapters 5 and 6 discuss in how far this correlation holds in the case of a more realistic thermal polymer glass in 3D.

1.3 Polymer glasses under deformation

Polymers are macromolecules that consist of many individual segments that are chemically bonded via covalent bonds. Due to their importance in industrial applications, a multitude of polymers have been developed, especially in the family of oil-based carbon-hydrogen polymers. If upon cooling of a polymer melt no chemical crosslinks are formed, then the polymer is *thermoplastic* and it undergoes a glass transition into a polymer glass.

In this work, I study an idealized model of such polymer glasses in order to better understand these crucial manufacturing materials in particular and glassy matter in general. Besides their huge practical importance, I chose to focus on polymer glasses, because they are good glass formers without tendencies to poly-crystallization. It is important to note, that having the chain topology of polymers in our model does introduce characteristic processes linked to polymer physics into the analysis of the glass state, specifically in the context of mechanical deformation. This section discusses the origin and importance of these processes in the context of this work.

Reduced mobility in the melt To understand the dynamics of polymers, the Rouse model [32] proposes a simple view on polymers as a set of N_c beads that are connected via N_c-1 linear springs. This is also known as the Gaussian chain model. The connectivity between the beads constrains the diffusive motion, and one finds that the mean square displacement (MSD) of the polymer increases more slowly in time ($\propto t^{1/2}$) than a single bead based on Brownian motion ($\propto t$). However, this behavior is only observed for small chain lengths. As the number of beads increases, multiple chains become *entangled*, meaning that they are wrapped around each other. Since polymers can not cross through one another, this further constrains the chain motion to a process called reptation [32]. De Gennes showed that at chain lengths beyond a material dependent entanglement length the MSD is reduced to $\propto t^{1/4}$ [29]. The dependence of the diffusion coefficient to chain length N_c also changes from $\propto N_c$ in the Rouse model to $\propto N_c^3$ for entangled chains [32].

Mobility in the glass state As discussed above, the dynamics in the glass state is dominated by the caging effect and the MSD exhibits a characteristic plateau beyond the ballistic time scale. In glassy matter, the important dynamical processes are cage-escapes that I call hop events. Although diffusive motion is possible as a series of hops by the same particle, the key glassy features of aging and heterogeneous dynamics are governed by the hop process and not by very long time scale diffusion. The diffusion constraining effects of polymer topology are therefore unimportant for the glassy dynamics [1]. This is true for polymer glasses in the quiescent state, yet one has to be more careful in the case of mechanical deformation.

Mechanical response A schematic stress-strain curve of a polymer glass is shown in fig. 1.7. The first three regimes are common to all glassy matter and amorphous solids: First, at small strains the stress increases linearly with the strain. In crystalline solids this linear response is a consequence of displacements of particles away from their lattice positions without rearrangements to other lattice points. When the external load is removed, the system returns to its original state and the deformation is elastic. In amorphous solids this *elastic regime* is marked by an analog linear macroscopic response, yet close observation reveals some plastic activity even at very small strains [10]. Viewed from the perspective of hops as elementary plastic events, this is not surprising however, since hops are present even in

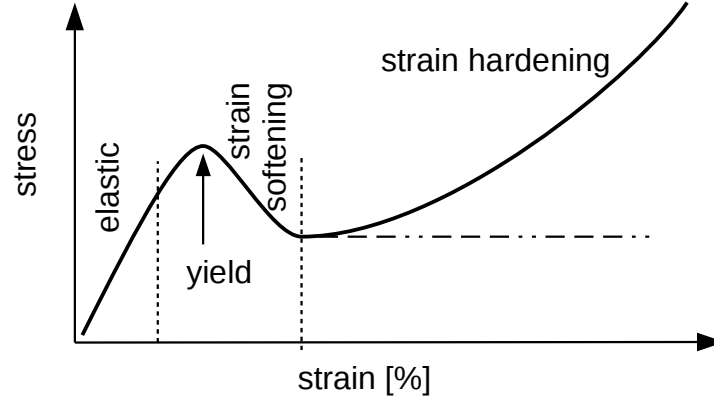


Figure 1.7: Stress versus strain observed in our polymer glass model. The deformation regimes are indicated (left to right): Elastic, yield, strain softening, strain hardening. The horizontal dashed line indicates steady state flow of a non-polymeric glass.

the quiescent state (no external load) due to the non-equilibrium dynamics.

As the strain increases the linear response smoothly transitions to a maximum stress, the *yield point*. This is accompanied by an increase in plastic events until the yield stress is reached and the system begins to flow. The height of the yield stress indicates the stiffness of the glass, is history dependent and increases during aging. The onset of flow is followed by a *strain softening regime*, where the stress decreases with increasing strain. The steepness of this decrease is again dependent on the material history and aging.

In non-polymeric glasses, flow drives the system to a steady state and the stress reaches a plateau value. In polymer glasses, the situation is different due to the chain-topology, and polymeric effects become important for the macroscopic mechanical response. As shown in fig. 1.7, instead of a steady state plateau, polymer glasses enter the *strain hardening regime*, where the stress increases non-linearly with strain. To increase the strain, the orientation of the polymer backbones have to more and more align with the deformation axis. As this happens an increasing amount of stress is stored in the bond interactions along the polymer backbone, which are much stronger than the monomer pair-interactions. Furthermore, if the chains are sufficiently long, entanglement effects come into play which further increase

the stress necessary to apply additional strain on the system.

1.4 Objectives of this work

The central goal of this thesis is to illuminate the microscopic processes that govern the mechanical properties of glassy matter in general, and polymer glasses in particular. Although plastics are ubiquitous industrial materials, our understanding of their plasticity is limited. The macroscopic response can be measured in experiments, yet the underlying microscopic processes have proven difficult to resolve. To bridge the gap between the microscopic behavior, the mesoscopic phenomena of dynamical heterogeneity and the macroscopic response, I performed large scale molecular dynamics simulations of a widely used polymer model. The computer simulations allow the observation of each particle with perfect detail and are therefore uniquely positioned to provide insights on the microscopic level. In chapter 2, I explain in detail the simulation techniques and the polymer model, as well as the measurement techniques used to identify the driving processes. In the remainder of this chapter, I highlight the individual questions that I am addressing in this work. The results of the four projects are discussed in chapters 3-6. This is followed by concluding remarks in the final chapter.

Recovery from mechanical deformation The design of my first project is inspired by the recent experimental study of Lee and Ediger [58] of polymer glasses in the recovery regime, discussed in detail in section 1.2.2. I give a complementary picture of the recovery regime by simultaneously measuring a variety of structural quantities that are inaccessible to experimental studies. To this end, I mirror the creep experiment in computer simulations as well as performing constant strain rate deformation. In addition to structural quantities I monitor the structural relaxation time (molecular mobility) as well as the inherent structure energy in the recovery regime. The key question is, whether mechanical deformation indeed leads to erasure of aging and to an “as newly quenched” glass *beyond* the perspective of molecular mobility. Computational studies of the PEL [54, 62] suggest that deformation leads to a state that is distinct from that of a younger glass. This study provides new insights by comparing the full aging behavior in the recovery regime with that of undeformed glasses. Furthermore, I explore the transition from transient to permanent rejuvenation and which deformation parameter is controlling

this transition. This question is important, since the driving deformation parameter has to play a prominent role in any theory of plasticity and there is a debate whether stress, strain or strain rate should be considered.

Spatio-temporal correlation between structural rearrangements

The aim of the second project is to spatially resolve DH and to quantify the correlated dynamics for a 3D glass in the aging regime, where only a few studies exist [71]. Does physical aging change DH in terms of correlation range or geometry of the regions that undergo significant structural relaxation? To perform our study on large-scale systems over extended simulation periods that are sufficient to analyze aging effects, I implement a novel hop detection algorithm that is based on a technique introduced by Candelier et al. [19]. This new algorithm allows the monitoring of hop events for all particles in large scale computer simulations with high spatial and temporal resolution. I use this method to create a detailed map of hops and to directly quantify the density-density correlation between hops. I study dependence on temperature, aging and infer correlation ranges. In the second part of this study, I focus on DH in the aging regime. This regime has only recently been explored using three- and four-point correlators [17, 71], and indications were found for an increase of dynamical correlation with age. The detailed map of hops allows me to spatially resolve DH and to measure its evolution as growing clusters of hops. A cluster algorithm is used to calculate the cluster volume distribution and I compare its evolution directly with the four-point dynamical susceptibility χ_4 as the standard measure for DH.

Soft modes link structure and rearrangements in polymer glasses

The third project broadens the understanding of the link between the location of rearrangements and the local structure. Recent studies [63, 81] showed that quasi-localized modes in the vibrational spectrum of glasses identify soft spots in model binary glasses, discussed in much detail in section 1.2.4. To fully understand the role of soft spots in plasticity of amorphous solids, it is important to test the robustness of the soft spot picture in other glass formers. For the first time, I quantify this link in the more realistic and industrially relevant case of a thermal polymer glass in 3D. Are particle rearrangements indeed predominantly occurring at soft spots and what is the impact of temperature and aging on this correlation? Furthermore, do soft modes hold additional information about the direction of individual rear-

1.4. Objectives of this work

rangements, and what is the lifetime of soft spots? As a first step, I explore different approaches on how to extract a map of the structural softness from the soft modes. In this third project, I focus on the quiescent state and I analyze the correlation between the calculated *softness field* with the likelihood to undergo hops. My results show that a positive correlation exists not only between the location of hops and soft modes, but also that the hop direction is correlated to the soft mode direction. Systems above (supercooled regime) and below (aging regime) the glass transition temperature are analyzed, and I discuss the impact of temperature as well as aging on the correlation. Furthermore, I analyze the lifetime of the softness field and my results show that the identified “soft” and “hard” regions are long lived compared to elementary vibrational timescales. This is important, because it shows that the softness field is a meaningful structural variable that could play a role in plasticity of amorphous solids similar to dislocations in the case of crystalline solids.

Predicting plastic events with structural features As a fourth and final project, I investigate the robustness of the found link between soft modes and hops in the case of deformed polymer glasses. The hops represent local plastic events and predicting their location based on the softness map is a central result of this project. Is this correlation affected by mechanical deformation and what are the processes underlying such a change in the correlation? To answer these questions, I quantify the correlation of softness field and hops at different points during uniaxial tensile deformation, from the elastic regime immediately after loading until far into the strain hardening regime. Prior to the deformation the polymer glass is aged for an extended time period, and I investigate indications for mechanical rejuvenation in the spatial correlation between softness field and hops. Interestingly, I find that the spatial correlation is increasing with growing strain in the strain hardening regime, and I explore possible explanations of this novel polymeric effect.

Chapter 2

Simulation and measurement techniques

The results of this thesis are based on molecular dynamics (MD) simulations with a simple glass-forming polymer model. The simulation approach has the advantage of giving access to microscopic details that are inaccessible via experimental techniques. Many experiments only give access to bulk averaged quantities, and this makes the study of inherently local phenomena like dynamical heterogeneity and plastic events challenging. With computer simulations it is possible to measure the microscopic dynamics with perfect detail, so that connections between microscopic processes and macroscopic response can be explored.

In the first half of this chapter, I introduce the polymer model, and elaborate on the MD techniques, the simulation of mechanical deformation, and the preparation of glass states. I also discuss general issues of this type of computer simulations, and how to interpret the results correctly. In the second half of this chapter, I explain the key measurements that I use to probe the polymer glass: First, I give details on the hop detection algorithm and second, I elaborate how vibrational modes are calculated and how the softness field is defined.

2.1 Polymer model

This work is based on a coarse-grained bead-spring polymer model that captures the chain-topology of a linear polymer without including the full atomistic detail. The polymer is represented as a sequence of identical beads, and neighboring beads are bonded to a linear chain that forms the polymer backbone. Figure 2.1 shows an example polymer and simulation box. Orientational correlations along the polymer backbone decay with increasing separation, and the characteristic decay length is called persistence length [32]. A polymer can therefore be partitioned into segments that are independent

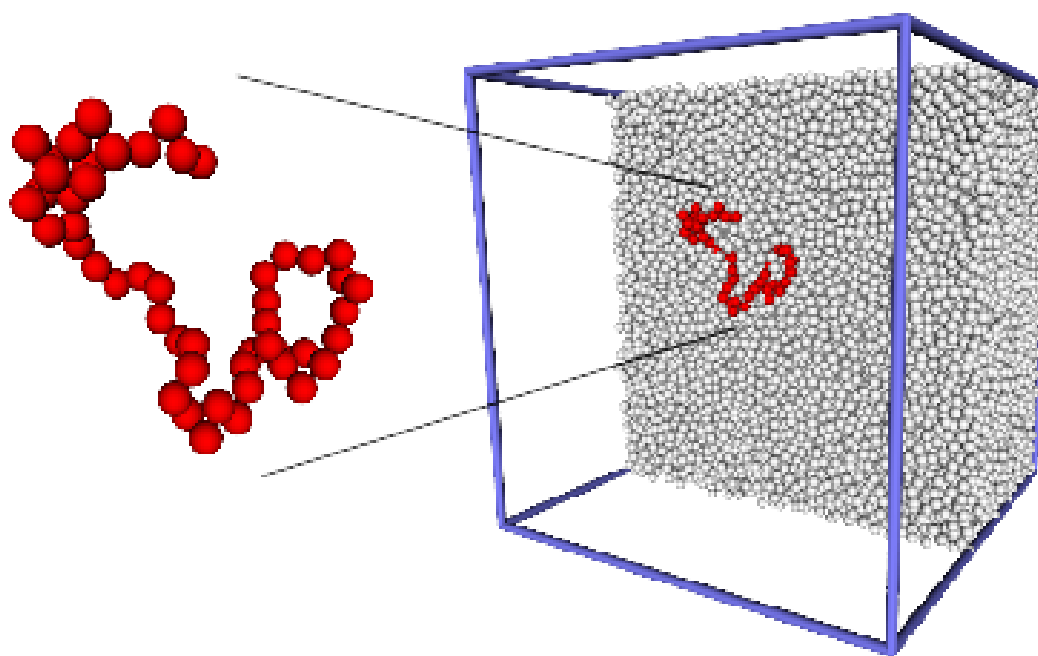


Figure 2.1: Visualization of a bead-spring polymer and the filled simulation box. The beads are indicated as spheres.

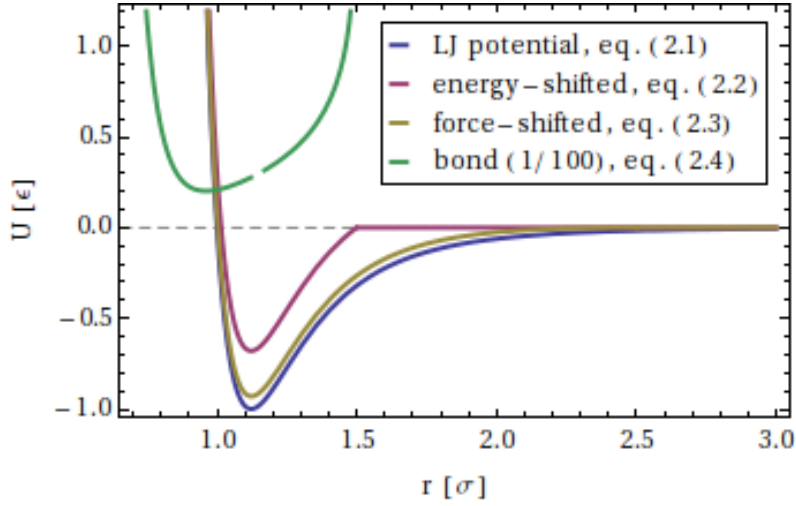


Figure 2.2: The LJ-potential between non-bonded beads is given by the blue curve, with energy- and force-shifted corrections in red and orange. For better comparison, the FENE spring potential is scaled by a factor of 10^{-2} and indicated by the green curve.

from each other. In the present model a single bead represents such a segment.

In a classical MD simulation, one defines potentials that describe the interaction between beads, as well as the covalent bonds along the polymer backbone. This work uses the finitely extensible nonlinear elastic (FENE) bead-spring polymer model [52]. It has been studied extensively in the glass state and shows the characteristic behavior expected for polymer glasses [8, 38, 70, 76, 94, 99]. The pair-potential between non-bonded beads is modeled as a 6-12 Lennard-Jones (LJ) potential

$$U_{LJ}(r_{i,j}) = 4u_0 \left[\left(\frac{a}{r_{i,j}} \right)^{12} - \left(\frac{a}{r_{i,j}} \right)^6 \right]. \quad (2.1)$$

Here, a is the bead diameter, u_0 is the depth of the LJ energy-well and $r_{i,j}$ is the distance between beads i and j . To simplify the notation, I neglect this index in the following. The potential is shown in fig 2.2. It has a repulsive part at short range $r < 2^{1/6}a$, which ensures that beads don't occupy the same volume. For $r > 2^{1/6}a$ the potential becomes attractive and it models the

2.1. Polymer model

van der Waals force. To improve computational efficiency [2], the potential is cut off and set to zero for distances $r > r_c$ together with an energy shift, which ensures that the potential is continuous at r_c . In the projects discussed in chapters 3 and 4 the pair potential is given by

$$U_{pair}(r) = \begin{cases} U_{LJ}(r) - U_{LJ}(r_c) & r < r_c \\ 0 & r \geq r_c \end{cases} \quad (2.2)$$

with $r_c = 1.5a$ chosen at the first minimum in the radial distribution function, i.e., only particles that are neighboring each other are interacting. The projects that study soft modes, chapters 5 and 6, require the calculation of second derivatives of the potentials. To ensure that the forces are differentiable at r_c I include a force-shift term

$$U_{pair}(r) = \begin{cases} U_{LJ}(r) - U_{LJ}(r_c) + (r_c - r) \cdot F_{LJ}(r_c) & r < r_c \\ 0 & r \geq r_c \end{cases} \quad (2.3)$$

In this case I use the cut-off $r_c = 2.5a$, which is beyond the second minimum of the radial distribution function. This choice makes the potential more numerically comparable to eq. (2.1), and both energy- and force-shifted versions are compared to eq. (2.1) in fig. 2.2. The main difference between both models is the extended attractive range of eq. (2.3), which results in small differences in the glass transition temperature and densities (see below).

A non-linear stiff spring-like interaction

$$U_{bond}(r) = \begin{cases} \frac{K R_0^2}{2} \ln [1 - (r/R_0)^2] + U_{LJ} + \epsilon & r < 2^{1/6}a \\ \frac{K R_0^2}{2} \ln [1 - (r/R_0)^2] & r \geq 2^{1/6}a \end{cases} \quad (2.4)$$

acts as covalent bonds along the polymer backbone and it consists of two parts: The last two terms are the repulsive part of the energy-shifted LJ potential with a cut-off $r_c = 2^{1/6}a$. The first term is attractive and diverges at a distance R_0 , which models unbreakable chains. My choice of $K = 30 u_0$ and $R_0 = 1.5a$ [52] ensures that chains can not cross through each other.

Reduced units The above defined potentials allow a scaling of distances and energies with the bead diameter a and energy-well depth u_0 respectively. In this thesis all results are given in reduced LJ-units [2] that are listed in table 2.1. For simplicity the * is omitted henceforth.

2.2. Molecular dynamics simulations

length	$\mathbf{r}^* = \frac{\mathbf{r}}{a}$	density	$\rho^* = \rho a^3$
energy	$U^* = \frac{U}{u_0}$	temperature	$T^* = \frac{k_B T}{u_0}$
time	$t^* = t \sqrt{\frac{u_0}{ma^2}}$	pressure	$\mathcal{P}^* = \mathcal{P} \frac{a^3}{u_0}$
force	$\mathbf{F}^* = \mathbf{F} \frac{a}{u_0}$		

Table 2.1: Reduced units used in this work in terms of bead diameter a , bead mass m as well as the characteristic energy u_0 .

2.2 Molecular dynamics simulations

The principal idea behind MD simulations is to solve Newtons equations of motion simultaneously for N particles in a fixed volume. The simulations for this thesis were done with the open-source package LAMMPS [72] that uses the velocity-Verlet algorithm [2]. The key approximation is the discretization of time, and the simulation updates particle locations $\mathbf{r}(t)$, velocities $\mathbf{v}(t)$, and accelerations $\mathbf{a}(t)$ to the next time step $t + \Delta t$ in four stages:

1. Velocities are updated to their mid-step values

$$\mathbf{v}(t + \Delta t/2) = \mathbf{v}(t) + \mathbf{a}(t)\Delta t/2 .$$

2. New positions are calculated

$$\mathbf{r}(t + \Delta t) = \mathbf{r}(t) + \mathbf{v}(t)\Delta t + \mathbf{a}(t)\Delta t^2/2 .$$

3. New forces and accelerations are calculated for all particles i with mass m using the model potentials and Newtons 2nd law

$$m \mathbf{a}_i(t + \Delta t) = \sum_{j \neq i} \mathbf{F}_{ij}(t + \Delta t) = - \sum_{j \neq i} \nabla U(\mathbf{r}_{ij}(t + \Delta t))$$

4. The velocity-step is completed

$$\mathbf{v}(t + \Delta t) = \mathbf{v}(t + \Delta t/2) + \mathbf{a}(t + \Delta t)\Delta t/2 .$$

This procedure is repeated to evolve the system of N particles forward in time. For the simulation results shown in this thesis I used $\Delta t = 0.0075$.

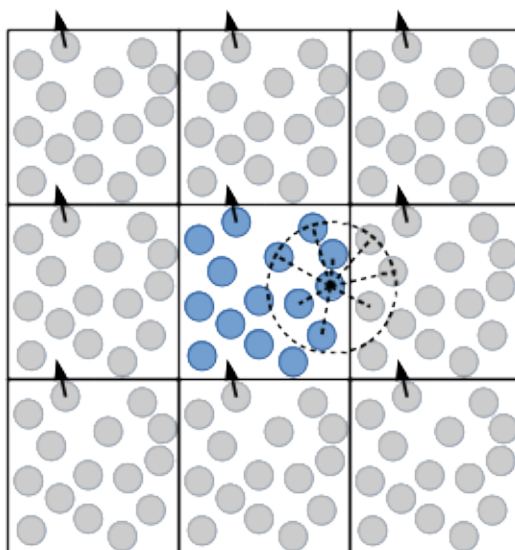


Figure 2.3: Sketch that illustrates periodic boundary conditions and minimum image convention. The central square with the blue particles is the simulation box, while image-particles are shown in gray. The arrow illustrates the position update of the particle. The dashed lines indicate the distance vectors from the central particle to all particles within a cut-off (dashed circle).

Boundary conditions This thesis explores the physics of polymer glasses in the bulk, and confinement effects near the edges of the simulation volume are avoided by imposing periodic boundary conditions. When a particle leaves the rectangular simulation box through one surface, a copy of it (an image-particle) reenters on the opposite surface. This effectively creates an infinite lattice of simulation boxes as indicated in fig. 2.3. As sketched in the same figure by a circle, particle interactions and other distance dependent calculations are performed by considering image-particles whenever they are closer than the particles in the simulation box. This technique is known as minimum image convention.

Thermostat Conventional MD simulations are energy conserving, since they are based on Newtons equations of motion. Under experimental conditions, however, the polymer glass is interacting with its environment. It is therefore more realistic to simulate the system at constant temperature. A variety of approaches have been developed to constrain the kinetic temperature in the system in agreement with the NVT ensemble (constant number of particles, volume and temperature). These methods are called “thermostats”, and I use the LAMMPS [72] implementation of two algorithms. I am using the *Langevin thermostat* [2] during equilibration in the melt, the temperature quench and during mechanical deformation. The *Nosé-Hoover thermostat* [46, 69] is used during the simulation of a quiescent glass.

The *Langevin thermostat* (LT) simulates the existence of a heat bath by introducing random and dissipation forces into the equations of motion, which become Langevin equations

$$m \mathbf{a}(t) = \mathbf{F}(t) - m \gamma \mathbf{v}(t) + \mathbf{f}_r .$$

Here, γ is a dampening constant and I used $\gamma = 1$. The random forces are independent for each particle as well as time step and have zero mean. They couple the system to a fixed external temperature T via a fluctuation-dissipation relation and the variance of the random force is $2 m k_B T / \gamma \Delta t$, with k_B being the Boltzmann constant.

In the *Nosé-Hoover thermostat* (NHT), the heat bath is introduced as an additional degree of freedom, that controls the flow of energy between the system and the reservoir. This approach leads to an additional friction force

$$m \mathbf{a}(t) = \mathbf{F}(\mathbf{t}) - m \xi \mathbf{v}(t) ,$$

with a coefficient ξ that is coupled to the fixed external temperature [2] via

$$\dot{\xi} = \frac{1}{Q} \left(\sum_i m v_i^2 - f k_B T \right) .$$

Here, the dot above ξ represents a time derivative, $f = 3N$ is the number of degrees of freedom in the system, and $Q = f k_B T \tau_{NH}^2$ controls the strength of the coupling via a relaxation time τ_{NH} . The simulations discussed in this thesis were performed with $\tau_{NH} = 0.5$.

The preparation of the polymer glass and mechanical deformation (discussed in the next two sections) as well as all simulations for the project discussed in chapter 3 were performed using the LT. During the implementation of the hop detection algorithm (see below) I realized that the LT can have a diminishing impact on the spatially heterogeneity of the dynamics in the glass state. The LT applies to each particle an independent random force and thus has a homogenizing effect on the dynamics. In contrast to this, the friction coefficient ξ of the NHT is a global property of the system (there is only one degree of freedom added for the heat bath), and in this sense the thermostat affects all particles in the same way. A comparison of the hop frequency and cluster size measured in the glass state shows that simulations with the NHT have slightly more hops that are more clustered in space. I emphasize that the observed differences are small, and to assess which simulation describes the glassy dynamics more accurately goes beyond the scope of this thesis. However, for the projects discussed in chapters 4-6 I chose to simulate the quiescent glass state (no external deformation) using the NHT, because I believe it to be the “safer” alternative that avoids to artificially drive the system into a dynamically less heterogeneous state.

Barostat The pressure is controlled by a Nosé-Hoover barostat [45], which adds an additional degree of freedom that simulates a pressure-bath [2]. This allows simulations in the NPT ensemble (constant number of particles, pressure and temperature). The bath couples to the pressure by rescaling the simulation box $\dot{L}_\alpha = \nu_\alpha L_\alpha$ in dimension α with coefficient ν_α that acts as a strain rate. Physically, the coupling resembles the action of a piston, which adjusts the accessible volume depending on the balance between internal and

2.3. Mechanical deformation

external pressure. The equations of motion are modified to

$$\begin{aligned}\dot{r}_\alpha(t) &= v_\alpha(t) + \nu_\alpha(r_\alpha - R_{0,\alpha}) \\ m a_\alpha(t) &= F_\alpha(t) - m \nu_\alpha v_\alpha(t) ,\end{aligned}$$

and in analogy to the thermostat discussed above, the coupling coefficient evolves according to [65]

$$\nu_\alpha = \frac{1}{\tau_B^2 N k_B T} V (\mathcal{P}_{\alpha\alpha}(t) - \mathcal{P}_{ext,\alpha\alpha}) .$$

Here, $\mathcal{P}_{\alpha\beta}(t) = (\sum_i^N v_{i,\alpha} v_{i,\beta} m / 2 + \sum_i^N r_{i,\alpha} F_{i,\beta}) / 3V$ is the instantaneous pressure tensor, while \mathcal{P}_{ext} is the fixed external pressure. All deformation simulations are performed with a relaxation time $\tau_B = 7.5$, and I use the LAMMPS [72] implementation of the algorithm that controls each dimension independently.

2.3 Mechanical deformation

Uniaxial tensile deformation is simulated with two different protocols. In both protocols the pressure perpendicular to the deformation axis is kept at $\mathcal{P}_{xx} = \mathcal{P}_{yy} = 0$. A creep experiment is simulated by applying a *constant stress* σ_z in the z-direction for a time period t_s , using the barostat with $\mathcal{P}_{zz} = -\sigma_z$. To avoid discontinuities, the pressure is ramped to $-\sigma_z$ over the time period 37.5. At the end of the deformation period, the pressure is ramped back to zero in the same way. This creep-protocol is used in the project discussed in chapter 3. A limitation of this protocol is that deformation can only be simulated up to the yield point. At the onset of flow the barostat becomes numerically unstable, since it cannot keep up with the rapid response of the system to the applied stress.

An alternative protocol that allows the simulation of mechanical deformation beyond the yield point is the deformation at *constant strain rate* $\dot{\epsilon} = \dot{L}_z / L_z$, where strain is defined as engineering strain $\epsilon = \Delta L_z / L_z$. The simulation box size along the z-direction is continuously increased at a constant rate for a time period t_s by directly rescaling space in that dimension. During the deformation period, the z-component of the pressure is not controlled by the barostat, while the other pressure components remain fixed at zero.

2.4. Preparing the polymer glass

Energy-shifted model, eq. (2.2)		Force-shifted model, eq. (2.3)	
T	ρ	T	ρ
0.2	1.005	0.2	1.059
0.25	0.995	0.3	1.043
0.3	0.983	0.4	1.023

Table 2.2: Densities in the melt used for the different target temperatures in the glass state. Densities in the left two columns are used in the projects discussed in chapters 3 and 4, while the right two columns are the parameters used in chapters 5 and 6.

2.4 Preparing the polymer glass

The polymer glass is prepared in two steps [99]: First, I create and equilibrate a polymer melt at the temperature $T = 1.2$. Second, this melt is quenched at a rate $6.7 \cdot 10^{-4}$ to below the glass transition temperature T_g . In the projects discussed in chapters 3 and 4 I simulated chains of length $N_c = 50$ beads with a total number of beads in the simulation $N = 50,000$. The simulation box volume was chosen such that the pressure at the end of the quench is close to $P = 0$, and the densities used for the different final temperatures are given in the first two columns of table 2.2. The calculation of the soft modes (see further below) in chapters 5 and 6 is computationally expensive and required a reduction of the system size to $N = 10,000$. The changes in the model potential discussed above result in slightly different melt densities and are given in the two right columns in table 2.2. The spatial size of the system is around 20 particle diameters in each dimension (for $N = 10,000$, otherwise larger), which is much larger than the physically important length scales. As discussed in section 1.2.1, glassy dynamics are dominated by the caging effect caused by neighboring particles, and particle distances are on the order of the particle diameter. The largest length scale present in the system is the end-to-end distance of a polymer, which is around 8.5 particle diameters (see fig. 2.4 below).

Polymer melt The creation of the polymer melt closely follows the procedure introduced in Ref. [4]. The positions of the beads of each polymer are initialized as a random walk in the simulation box with step length $0.92a$, and consecutive steps are constrained by $\|\mathbf{r}_i - \mathbf{r}_{i+2}\| \geq 1.02a$ [4]. This results in polymer configurations that are close to the equilibrium statistics, yet it allows beads to overlap, which is unphysical and result in diverging forces due to the repulsive part of the LJ potential (see eq. (2.1)). This problem is resolved in two stages:

1. Slow push - Instead of using the LJ pair-potential from the beginning, one simulates the first 3000 time steps using the soft potential

$$U_{pair}(r) = A [1 + \cos(\pi r/r_c)] \text{ , if } r < r_c \text{ .}$$

The coefficient A is increased linearly $1 \leq A \leq 100$ over the run, driving a reduction of the overlap.

2. Fast push - The soft potential is now replaced by the LJ potential and the simulation is run for an additional 3000 time steps. To keep the particle velocities from diverging due to the remaining overlap, one rescales the velocities every 50 time steps such that the temperature is $\sum_{i=1}^N v_i^2 / 2m = 1.2$.

The system is then equilibrated by running it in the NVT ensemble for 10^7 time steps. To ensure that an equilibrium state is reached, I measure the mean-square end-to-end distance of chain segments of length n along the polymer backbone

$$\langle \mathbf{R}^2 \rangle(n) = \left\langle \frac{1}{N_n} \sum_{|i-j|=n}^{N_n} (\mathbf{r}_i - \mathbf{r}_j)^2 \right\rangle \text{ .}$$

Here, $\langle . \rangle$ indicates an average over all polymers. This mean square internal distance (MSID) has a signature peak at intermediate n that vanishes when equilibration is reached [4]. Figure 2.4 shows the MSID at different equilibration run lengths $N_{\Delta t}$ for a short-chain system. One can see a characteristic peak around $n = 10$, which reduces with increasing run time. After 10^7 time steps the MSID does not change any more and the system has reached equilibrium.

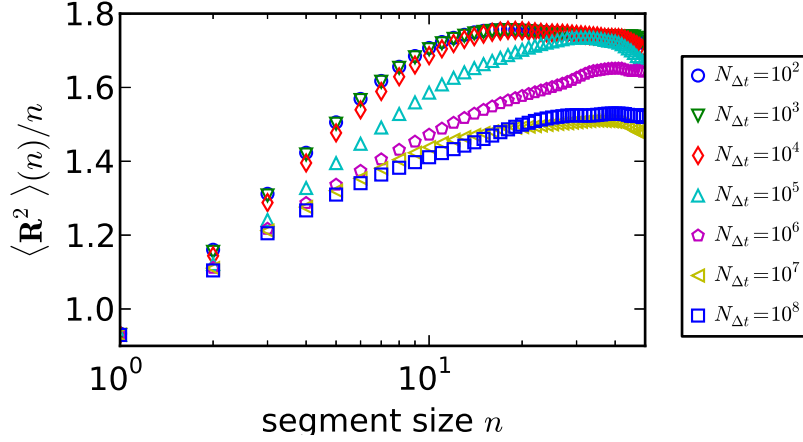


Figure 2.4: Mean square internal distance at different times during the equilibration run, as indicated in the legend.

Glasses at different temperatures and ages The polymer glass is created from the melt via a rapid quench to below the glass transition temperature at constant volume and quench rate $\dot{T} = -6.7 \cdot 10^{-4}$. The glass transition temperature for the energy-shifted model (chapters 3, 4) is $T_g \simeq 0.35$ [76]. For the force-shifted model (chapters 5, 6) $T_g \simeq 0.4$ is estimated from the temperature dependence of the pressure during cooling, see also fig. 1.1(b). To study the temperature dependence of measured quantities, glasses at different final temperatures are created, and a list of all temperatures used in this thesis is given in table 2.2.

As discussed above, the density is chosen for different target temperatures such that the hydrostatic pressure is close to zero at the end of the quench. In a final step after the quench, the simulation is switched to the NPT ensemble using a barostat (see above) and the pressure is quickly ramped to zero over the time period 37.5. The resulting system is what I call an “as quenched” or “newly quenched” glass in the quiescent state. To study the effects of non-equilibrium dynamics, the system can then be evolved to different ages by simulating it at zero pressure in the NPT ensemble for the desired time period.

2.5 Interpreting simulation results

There are two fundamental problems in correctly interpreting results from these simulations. The first challenge is: how can one ensure that the numerical model accurately simulates the physical glass? Fully atomistic simulations with quantum-mechanical detail are computationally very expensive and restrict the system size to a few hundred atoms. As explained in the introduction, glassy dynamics can be found in many diverse physical systems that stretch many orders of length scales. Glassy physics is therefore not critically dependent on microscopic details, but is instead driven by the interaction of many particles in a crowded environment and without an accessible ordered ground state. As mentioned above, the bead-spring polymer model has been successfully used in other studies [8, 70, 76, 94, 99] to explore the glass state. To ensure that my simulations capture the glassy physics, I have checked that the key signatures of glassy dynamics (see introduction) are present in the simulation. I identified the expected power-law age dependence of the relaxation time and logarithmic aging of structural properties (chapter 3), as well as dynamical heterogeneity (chapter 4).

The second fundamental problem is the numerical accuracy of the predicted dynamics. MD simulations are based on Newton's equations of motion, and temperature as well as pressure are controlled via well established techniques. Although this work is not aiming at characterizing a specific physical system with high numerical detail, but rather to explore general characteristics, trends and dependencies of glassy dynamics, it is nonetheless crucial to accurately estimate the equations of motion in order to successfully simulate the physical processes that drive glassy dynamics. The key numerical approximation of MD is the discretization of time and a typical time step is of order 10^{-14} s. Although computational resources are growing exponentially, it is currently only possible to simulate on time scales up to $\sim \mu$ s. In contrast to this, at the viscosity threshold for the glass transition structural relaxation happens on time scales ~ 100 s. In order to use MD techniques to study glasses, it is therefore necessary to choose a model that exhibits glassy behavior on the computationally accessible, rather than realistic time scales. Furthermore, to simulate experimental perturbations like mechanical deformation and cooling, one has to increase the rate of change by 4-8 orders of magnitude. These non-physical rates, which are used in this study, are a common and legitimate cause of concern for numerical studies of glasses and there is no simple solution for this problem. The “accelerated dynamics” that is

introduced via the simple bead-spring model might equalize the disparity between physical and simulated perturbation rates, i.e., the system is deformed much faster than in the laboratory, but due to the faster than physical dynamics it can respond in kind and in a physically correct way. Validation of the simulation results again relies on a comparison with experimental results. The project discussed in chapter 3 was designed in close relation to a recent experimental study, and our results for the structural relaxation time all the qualitative features identified by the experiment. Despite the challenges of simulating glassy dynamics with MD there is a large body of computational work that study binary [50, 81, 82, 98] and polymeric glasses [38, 70, 74, 99], supercooled liquids [21, 101] and granular media [19, 20] using MD.

2.6 Hop detection

A key measurement used in this thesis is the detection of hops, see caging effect in section 1.2.1. The detection is based on an adaptation of an algorithm proposed by Candelier et al. [19]. The algorithm measures the average squared distance between two adjacent parts of the trajectory, and a hop is detected when this distance is bigger than a threshold, which is related to the height of the caging regime plateau in the MSD [19, 20] (see fig. 1.2 in section 1.2.1). The method was successfully used in studies of agitated granular media [19, 20], a supercooled liquid in 2D [21] and more recently in a cyclically sheared glass in 3D [73].

The original algorithm is based on a recursive scheme on saved trajectories, and my adaptation is to run the detection “on-the-fly” in the spirit of a running average. This adaptation is an important technical contribution of this thesis, because it allows the measurement of hops with much better temporal resolution.

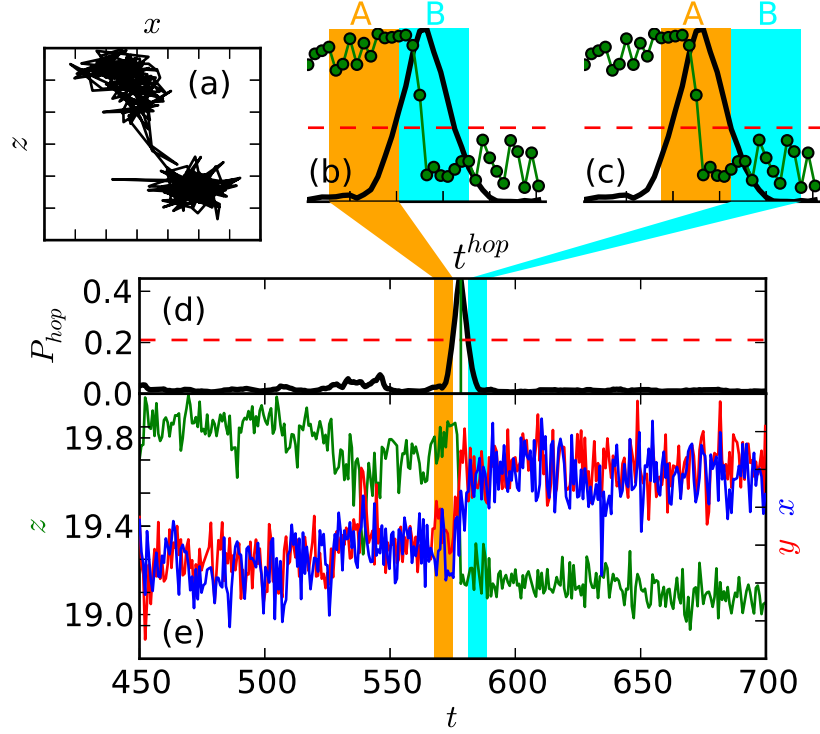


Figure 2.5: Sample trajectory of a particle and hop identifier function P_{hop} . (a) shows the localization into two cages and the 'hop' is marked by rapid changes in the trajectory (e). Corresponding to this, P_{hop} in (d) is sharply peaked at the transition and the maximum defines the hop time t_{hop} . Plots (b) and (c) are overlays of P_{hop} and the trajectory just before and after the hop (z-comp. only for better visibility). The colored fields (A and B) in both plots indicate the evaluation window for P_{hop} [see eq. (2.5)]. Initial and final positions are calculated from time averages of the trajectory parts that are highlighted as zoom, i.e., (b) initial position (orange) and (c) final position (cyan).

2.6. Hop detection

During the simulation run the most recent section of the trajectory of a particle is stored in $N_{hist} = 20$ data points, and every $N_{obs} = 100$ time steps the oldest point is replaced by the current position. This gives access to a time window $t_{eval} = N_{obs} N_{hist} \Delta t = 15$ (the parameter choices are discussed below), and the trajectory is separated into two parts A ($t - t_{eval}, t - t_{eval}/2$] and B ($t - t_{eval}/2, t$] of equal size. A *hop identifier function*

$$P_{hop} \left(t - \frac{t_{eval}}{2} \right) = \sqrt{\langle (\mathbf{r}^A - \bar{\mathbf{r}}^B)^2 \rangle_A \cdot \langle (\mathbf{r}^B - \bar{\mathbf{r}}^A)^2 \rangle_B} \quad (2.5)$$

is calculated every N_{obs} time steps that measures the averaged squared distance between the mean position in part A , $\bar{\mathbf{r}}^A$, and all trajectory points in part B , \mathbf{r}^B , and vice versa. It is large when the trajectory changes rapidly at $t - t_{eval}/2$, and a hop is detected when P_{hop} exceeds a temperature dependent threshold $P_{hop} > P_{th}$. The thresholds used in this thesis are given in table 2.3 and the parameter choices are discussed further below.

In Figs. 2.5(a) and (e) I show a sample trajectory of a particle together with the calculated P_{hop} , fig. 2.5(d). A hop is clearly identified and the algorithm records particle id, hop time t_{hop} and position of the particle before and after the hop \mathbf{r}_{init} and \mathbf{r}_{final} . The hop time is defined at the maximum of P_{hop} , and the locations are calculated from averages as the threshold is crossed: before the peak $\mathbf{r}_{init} = \langle \mathbf{r} \rangle_A$ [see fig. 2.5(b)] and after the peak $\mathbf{r}_{final} = \langle \mathbf{r} \rangle_B$ [see fig. 2.5(c)]. Using this algorithm on each particle via a parallel implementation in LAMMPS [72] allows the monitoring of all hops in the system for the full duration of the simulation.

Irreversible hops In the projects discussed in chapters 5 and 6, I use an additional evaluation step in order to exclude back-and-forth hops of a particle between the same two positions. This is implemented as a post-processing procedure at the end of the simulation. All hops of a single particle are read from the output of the hop detection algorithm, and two consecutive hops are removed, if the final position of the second hop is within a distance of $\sqrt{P_{th}}/2$ of the initial position of the first hop. With this adaptation, the remaining hops give a full map of the irreversible structural rearrangements measured during the simulation. To assess the robustness of this procedure, the results in chapter 5 were recalculated with a distance threshold $\sqrt{P_{th}}$, and no significant changes were found.

2.6. Hop detection

T	0.2	0.25	0.3	0.4
P_{th}	0.15	0.18	0.21	0.27

Table 2.3: Hop identifier function thresholds used for the different target temperatures in the glass state.

Parameter choices Candelier et al. [19] used a threshold P_{th} that was somewhat bigger than the plateau height in the MSD, which I denote as a_c^2 . I reduce the ambiguity in the choice of P_{th} by measuring a histogram of peak-heights in the hop identifier function. If one assumes that a particle in a glass has only two well defined modes of movement: vibration around a fixed mean position (caged) and instant jump by a distance $> a_c$ (hop), then the hop detection would only pick up peaks of height $> a_c^2$.

In fig. 2.6 the \diamond data (standard time window parameters, see below) is the measured histogram. We find a distribution of peak heights that is largest at small heights, with a long exponential tail towards larger peaks. The small peaks are due to shifts of the mean particle position within the cages. This is expected, because each member of the surrounding shell that form the cage is not fixed in space, but moves within a small area (its own cage). Cages are therefore not static, but instead change slightly over time. The measured distribution shows a relatively sharp transition to an exponential tail, which indicates the existence of an additional source of larger peaks, the cage-escapes or hops. I therefore use the crossover point as the threshold, and based on the data shown in fig. 2.6 for the polymer glass at temperature $T = 0.3$ the threshold is $P_{th} = 0.21$ (dashed line). For comparison, the inset shows the mean square displacement and the horizontal line indicate P_{th} . Analog measurements were performed for the other glass temperatures and all thresholds used in this thesis are given in table 2.3.

The time window $t_{eval} = N_{hist} N_{obs} \Delta t$ used in the algorithm is defined by two parameters, the number of stored trajectory points N_{hist} and the frequency in time steps N_{obs} at which the trajectory is updated and P_{hop} recalculated. The update frequency used in this thesis is $N_{obs} \Delta t = 0.75$, which is the mean time between particle collisions indicated by the onset of the caging plateau in the inset of fig. 2.6 (dotted line). This also sets the maximal temporal resolution for the hop time. The time window t_{eval} is the main influence on the detection algorithm. It sets the maximal resolution of

2.6. Hop detection

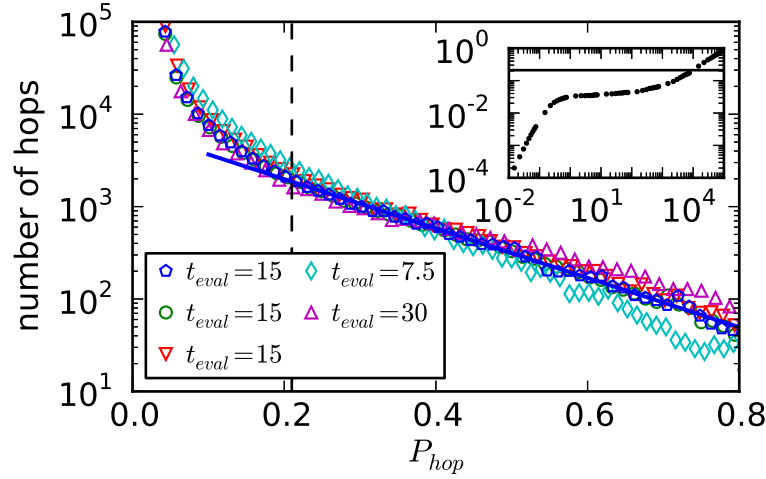


Figure 2.6: Histograms of hop identifier P_{hop} peak heights calculated at glass temperature $T = 0.3$ and time window parameters (order of legend): $(N_{hist}, N_{obs}) = (20, 100), (40, 50), (10, 200), (10, 100), (40, 100)$. The data for the three parameter sets with $t_{eval} = 15$ are nearly identical (blue \diamond overlay other markers). The solid line is an exponential fit of the distribution tail and the dashed line indicates the resulting parameter choice P_{th} . The inset shows the mean square displacement as function of time and P_{th} is indicated by the horizontal line.

two consecutive hops ($t_{eval}/2$) and also acts as an upper limit for the duration of a hop. To maximize the resolution but also ensure that meaningful averages are possible [see eq. (2.5)], I choose $N_{hist} = 20$ and therefore $t_{eval} = 15$. In fig. 2.6 I illustrate the impact of this parameter. Note that the histogram for the present parameter values (\diamond) coincides with two other parameter sets with equal t_{eval} (histograms are nearly identical and therefore difficult to distinguish). This shows that only the window size has a direct impact on the hop detection. Consequently, a smaller time window yields the detection of more peaks with small height, and a larger t_{eval} results in fewer small peaks, but also in a lower resolution.

2.7 Vibrational modes and the softness field

The low energy vibrational spectrum is used to calculate a *softness field* that quantifies the participation of particles in quasi-localized vibrational modes, see discussion in section 1.2.4. During the simulation run, snapshots of the system are stored in logarithmically spaced time intervals. The softness field at time t is measured in four steps:

1. Starting with a snapshot of the system at time t , a combination of gradient descent and damped dynamics (FIRE [15]) algorithms are used to minimize the forces present in the system. Both algorithms are implemented in LAMMPS [72]. The resulting spatial configuration of the particles is the inherent structure.
2. The Hessian [see eq. (1.1)] is calculated with the model potentials and the inherent structure. The result is a $3N$ by $3N$ symmetric sparse matrix.
3. The low energy vibrational spectrum is calculated by partially diagonalizing the Hessian using ARPACK [87]. I am using the solver for a real symmetric matrix in the shift-inverted mode with shift parameter set to zero. Arpack is an implementation of the Implicitly Restarted Lanczos Method [87], which is a numerically reliable algorithm for the estimation of eigenmodes that is based on the power method for finding eigenmodes. It exploits the idea that the result of repeated multiplication $\mathbf{x}_n = \mathbf{A} \cdot \mathbf{x}_{n-1}$ of an initially random vector \mathbf{x}_0 with the matrix \mathbf{A} converges to the eigenvector of the largest eigenmode of \mathbf{A} .
4. The N_m lowest energy eigenmodes with non-zero eigenvalues are used to calculate the softness field. The definition of the softness field is explained in detail below.

An analysis of the maximal cross-correlation (see eq. (5.1) in chapter 5) between hops and softness field (see eq. (2.6) below) as a function of N_m reveals a broad and weak maximum between $300 > N_m > 900$ (1-3% of the modes). For the results discussed in chapters 5 and 6 I use $N_m = 600$. Already $N_m = 300$ yields 95% of the quantitative accuracy.

Softness field definition The softness of a particle is defined as the superposition of the participation fractions in the low energy vibrational modes [68, 102, 103],

$$\phi_i = \frac{1}{N_m} \sum_{j=1}^{N_m} |\mathbf{e}_j^{(i)}|^2. \quad (2.6)$$

Here, the polarization vector $\mathbf{e}_j^{(i)}$ is the projection of the eigenvector of mode j on the degrees of freedom of particle i , see section 1.2.4 for more details. The softness field ϕ depends on a single parameter, the number of included low energy modes N_m , and the scaling factor is added to make the softness an intensive quantity in terms of N_m . A particle i is considered “softer” the larger ϕ_i is, and it is used to rank the particles according to their relative softness. The absolute value of ϕ is not in itself meaningful, since the participation fractions are normalized quantities, i.e., $\sum_{i=1}^N |\mathbf{e}_j^{(i)}|^2 = 1$. The softness of a particle therefore describes its average participation fraction in the N_m lowest energy vibrational modes.

It is worth pointing out that the contribution of each mode should be weighted by its energy. A particle that is involved in a low energy mode requires less energy to be excited to the same extent than a particle with identical projection $|\mathbf{e}^{(i)}|^2$ in a higher frequency mode. However, I find that this weighting does not improve the predictive strength of the softness field for the present system, since the frequency does not vary strongly for the contributing modes. More details about the effect of this weighting as well as alternative definitions of softness are discussed below.

Direction of the softness field Directional information can be added to the scalar softness field in a similar superposition scheme. The eigenvector of mode j defines the mode direction for particle i via the polarization vector $\mathbf{e}_j^{(i)}$. This vector is defined up to its sign due to the harmonic nature of the description. In order to find the dominating direction in the N_m modes, I calculate nematic tensors from the unit length projection vectors $(Q_j^{(i)})_{\alpha,\beta} = \left(\frac{3}{2} \hat{e}_{j,\alpha}^{(i)} \hat{e}_{j,\beta}^{(i)} - \frac{1}{2} \delta_{\alpha,\beta} \right)$ and perform a weighted average

$$\mathbf{Q}_\phi^{(i)} = \frac{\sum_{j=1}^{N_m} |\mathbf{e}_j^{(i)}|^2 \mathbf{Q}_j^{(i)}}{\sum_{j=1}^{N_m} |\mathbf{e}_j^{(i)}|^2}.$$

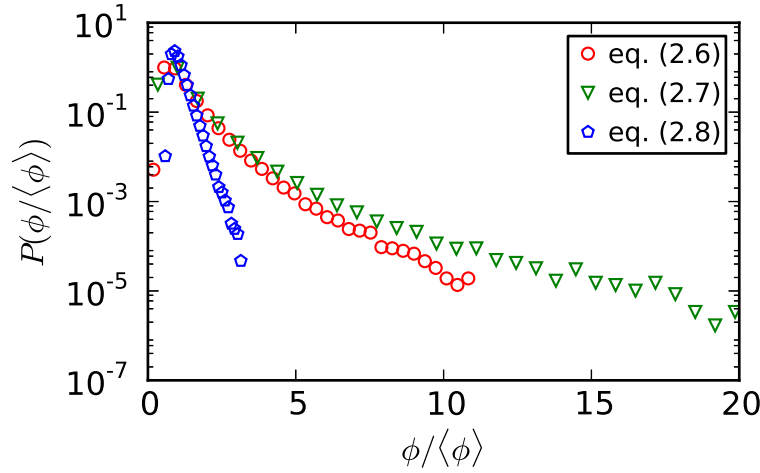


Figure 2.7: Distribution of softness in the system $T = 0.3$, $t_{age} = 750$ for three definitions of the softness field. The softness is rescaled in terms of the mean softness to allow an easier comparison.

The eigenvector of the largest eigenvalue of $\mathbf{Q}_\phi^{(i)}$ then defines the direction of the softness field $\mathbf{e}_\phi^{(i)}$. The direction of the softness of a particle therefore indicates the mean direction of the N_m lowest energy vibrational modes.

2.7.1 Alternative definitions

The definition of a field that quantifies the participation of particles in soft modes is not unique. The superposition of participation fractions used here and in several other studies [68, 102, 103] essentially measures the average potential energy of the particles. To see this, note that the participation fractions distribute the total potential energy $\langle U_j \rangle$ of mode j over particles i so that $\langle U_j^{(i)} \rangle = \langle U_j \rangle |\mathbf{e}_j^{(i)}|^2$, and $\langle \dots \rangle$ denotes a thermal rather than disorder average. The softness field defined in eq. (2.6) is therefore proportional to the *mean potential energy* of particle i in the N_m lowest energy modes, assuming equipartition of the mode energies. However, as mentioned above, participation in lower energy modes should be more important than in higher energy modes, since less energy is needed to displace a particle from its inherent structure position. In this view, the softness of a particle becomes proportional to its *mean squared vibrational amplitude* $\langle x_j^{(i)2} \rangle = 2\langle U_j^{(i)} \rangle / m\omega_j^2$, and

the softness field becomes

$$\phi_i = \frac{1}{N_m} \sum_{j=1}^{N_m} \frac{|\mathbf{e}_j^{(i)}|^2}{m\omega_j^2} . \quad (2.7)$$

Finally, one may ask why the mean squared vibrational amplitude should be considered rather than the *mean absolute* or root-mean-squared amplitude. This leads to a third alternative for the softness field

$$\phi_i = \frac{1}{N_m} \sum_{j=1}^{N_m} \frac{|\mathbf{e}_j^{(i)}|}{\sqrt{m\omega_j^2}} . \quad (2.8)$$

Figure 2.7 compares the distributions of softness resulting from these three alternative definitions. The weighting w.r.t. mode energy given in eq. (2.7) stretches the distribution obtained from eq. (2.6) without changing it qualitatively. Using the average displacements as measures on the other hand yields a qualitatively different, purely exponential distribution of softness. This exponential form reminds of the self-part of the van Hove function, which measures the distribution of particle displacements over a fixed time window. A signature of dynamical heterogeneity is the non-Gaussian, exponential tail found in the van Hove function, and the softness field based on eq. (2.8) seems to hold a fingerprint of this characteristic feature of glassy dynamics. I also compared the spatial and directional correlation of the softness based on eqns. (2.6)-(2.8) to hops. The results are remarkably insensitive qualitatively as well as quantitatively, with eq. (2.8) yielding a slightly better spatial correlation. I chose to use the definition in eq. (2.6) for ease of comparison with previous studies in other systems.

Chapter 3

Recovery from mechanical deformation¹

This first project studies the complex interplay between physical aging and mechanical deformation in glasses, specifically the phenomenon called mechanical rejuvenation. A detailed explanation is given in section 1.2.2, in summary: aging leads to a slowing of the molecular mobility, which can be measured as an increasing bulk structural relaxation time τ_α with growing age. One can therefore think of τ_α as an internal “material clock”. Mechanical deformation decreases τ_α and this reversal of the aging effect results in a system that is dynamically equivalent to a younger glass. Whether the deformed glass is truly comparable to a younger glass is still an open question [64], with computational studies of the potential energy landscape [54, 62] suggesting that deformation drives the system into a state that is different from a glass of less age.

A recent experiment [58] explored the behavior of polymer glasses in the recovery regime after the end of a creep deformation. A fluorescence microscopy technique was used to observe changes of the molecular mobility over time and the results in the recovery regime were compared to the aging behavior of a quiescent glass without deformation history. The experiment found that pre-yield deformation results in a transient reduction of τ_α followed by a quick return to pre-deformation behavior, while the molecular mobility of a glass after deformation far in the post-yield regime is comparable with an as quenched glass.

This project uses computer simulations to give a complementary picture of glasses in the recovery regime. The glass was simulated in the aging regime at the temperature $T = 0.2$, which is far below the glass transition temperature $T_g \sim 0.35$ [76]. In addition to the molecular mobility I monitor structural as well as energetic quantities to clarify whether deformation drives glasses to a state that is comparable to a younger glass without deformation

¹Large parts of this chapter have been published in ref. [84]

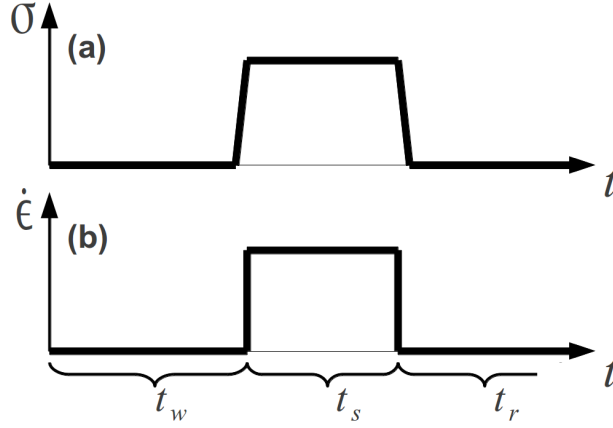


Figure 3.1: Schematic protocol of the simulation with waiting time period t_w , uniaxial tensile creep (a) or fixed strain rate (b) deformation period t_s , and recovery period t_r .

history. In analogy to the experiment, the simulations are designed in three stages, shown in fig 3.1(a): The newly quenched glasses are aged at zero pressure in the quiescent state for a waiting time t_w . This is followed by a creep period t_s at constant tensile stress σ , and the recovery regime t_r after unloading. At the beginning and end of the creep period, the stress is quickly ramped up and down to avoid unphysical discontinuities. I study the quasi-adiabatic limit of negligible aging during deformation by restricting the deformation time to $t_s < t_w$. To study the effect of deformations beyond the yield point at strains $\epsilon \sim 6\%$, I also use the constant strain rate $\dot{\epsilon}$ protocol shown in 3.1(b).

3.1 Immediate impact of creep

When tensile stress is applied to a glass, the material reacts first with an elastic response followed by plastic deformation. In fig. 3.2(a) I show the plastic part of the creep compliance

$$J(t, t_w) = \frac{\epsilon(t, t_w)}{\sigma}$$

of the glass for a range of imposed stress amplitudes σ . The engineering strain $\epsilon = \Delta L/L$ is calculated along the z-direction and the values at $t_s =$

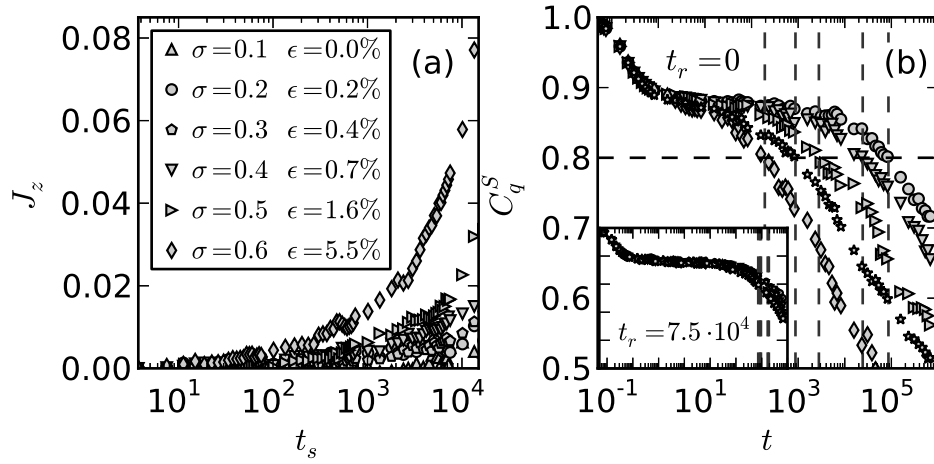


Figure 3.2: Panel (a) shows the creep compliance of a glass with age $t_w = 75000$ for different external stresses σ . The indicated strains are calculated at $t_s = 15000$. Panel (b) shows the intermediate scattering function C_q^S of the perturbed glasses shown in (a) in the recovery regime together with a just-quenched glass (\star). The main graph shows C_q^S just after unloading ($t_r = 0$) and the inset is calculated at $t_r = 75000$. The dashed lines define the α -relaxation time.

3.2. Recovery of the relaxation time

15000 are given in the legend. It is clearly visible that larger stress yields a much larger creep compliance, indicating a non-linear response. Figure 3.2(a) shows results for a glass with age $t_w = 75000$, and for increasing wait times I observe (not shown here) the well known double logarithmic shift towards smaller compliance as discussed for instance in ref. [99].

Figure 3.2(b) shows the self part of the intermediate scattering function (ISF)

$$C_q^S(t, t_a, t_r) = \langle \exp(i\mathbf{q} \cdot [\mathbf{r}(t + t_a + t_r) - \mathbf{r}(t_a + t_r)]) \rangle,$$

which is a standard measure of relaxation times in aging glasses [50]. Here, the average is performed over all beads at a certain time, $\mathbf{r}(t)$ is the position of a bead at time t and the wave vector $\mathbf{q} = 2\pi\mathbf{e}_z$ corresponds to a displacement of a along the deformation axis. The glass age after unloading is given by $t_a = t_w + t_s$. In glasses, the ISF shows three regimes that are identical to those discussed for the mean square displacement in section 1.2.1: A ballistic regime at very small time scales is followed by a caging plateau at intermediate times, and the decay at large times indicates the diffusive regime. Aging increases the intrinsic time scale of the glass, and the resulting lengthening of the plateau is visible by comparing the inset and main plot of fig. 3.2(b). I define the structural relaxation time τ_α as the time when the ISF has decayed below the caging-plateau or $C_q^S(\tau_\alpha, t_a, t_r) = 0.8$. In fig. 3.2(b), this is indicated by dashed lines.

The main graph in fig. 3.2(b) shows the ISF measured immediately after unloading at $t_r = 0$ for the systems in panel (a) that were deformed at stresses $\sigma = 0.2, 0.4, 0.5, 0.6$. Additionally, the ISF of a newly quenched glass is shown (★). The mechanical perturbation yields a shortening of the caging plateau and a corresponding shift of τ_α towards smaller times, which agrees with previous studies [48, 88, 99]. The relaxation curve for $\epsilon = 5.5\%$ indicates that this glass relaxes even faster than the just-quenched glass. The reason for this is that the later already has an effective age of $\sim 10^3$, which it acquires during the quench. The inset shows that the differences in the relaxation behavior disappear after a long recovery period. In the following, I clarify whether the impact of mechanical perturbation is transient or permanent by studying the path of recovery.

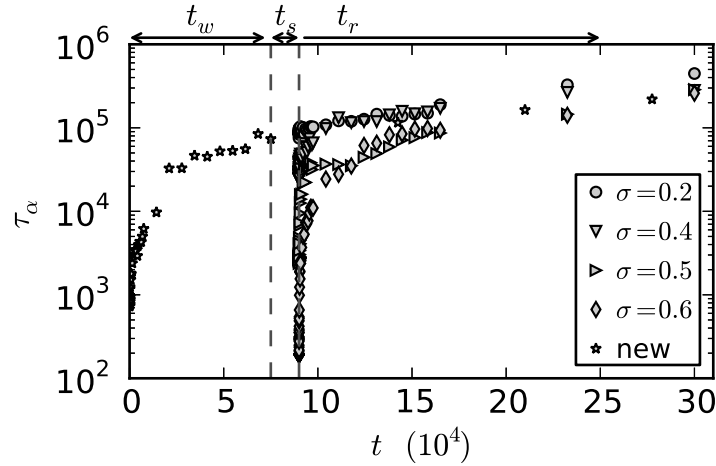


Figure 3.3: Evolution of α -relaxation time of a just-quenched “new” glass compared to those of mechanically perturbed glasses in the recovery regime. The glasses are identical in the initial aging regime $t_w = 75000$, the creep time is $t_s = 15000$, and the time regimes are indicated by the dashed lines. Other results from simulations with these parameters are shown in fig. 3.2.

3.2 Recovery of the relaxation time

The evolution of the α -relaxation time after unloading holds key information about the change in the aging dynamics. Lee and Ediger showed experimentally that τ_α measured in the recovery regime can be shifted onto the relaxation time of an unperturbed sample [58], and this behavior was associated with mechanical rejuvenation. Furthermore, they repeated the experiment with a sample deeper in the glass phase and found merely transient changes. The relaxation time did not behave like that of a new glass, but rather returned to the original unperturbed evolution after a short time. In fig. 3.3 I show the relaxation time of an unperturbed glass together with τ_α in the recovery regime after mechanical perturbation with several stress amplitudes. In all cases I find that the relaxation time immediately after unloading decreases with increasing stress amplitude. For $\sigma < 0.5$ my results show a rapid return to the unperturbed evolution, which suggests a non-permanent change of the aging dynamics. In agreement with ref. [58], τ_α for larger stresses $\sigma \geq 0.5$ exhibits dynamics very similar to a just-quenched glass but shifted in time.

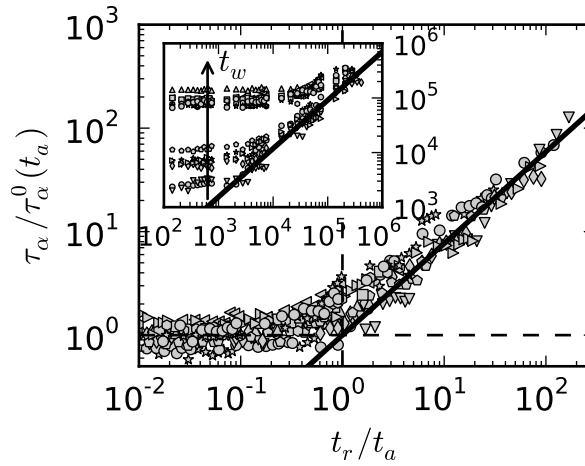


Figure 3.4: Relaxation time dynamics of unperturbed glasses with a range of wait times $10^3 \leq t_w \leq 10^5$ in a double logarithmic plot. The continuous black line is the “generic” aging dynamics τ_α^0 and in the inset (axes: τ_α over t_r) I show the shift of τ_α with increasing t_w . The main graph shows a data collapse with t_r measured in units of glass age $t_a = t_w$ and τ_α being rescaled by $\tau_\alpha^0(t_a)$. The dashed lines are guides to the eye.

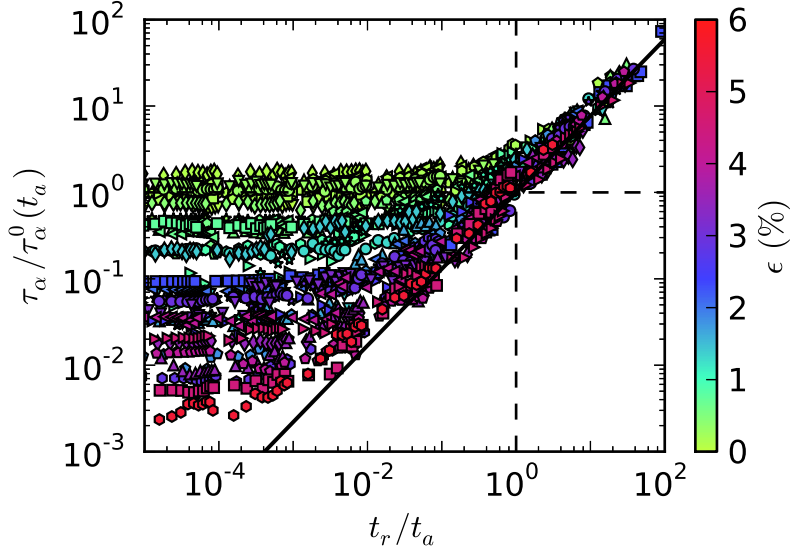


Figure 3.5: Relaxation time of mechanically perturbed glasses in the recovery regime. The coloring represents the total strain at time of unloading. The continuous line indicates the generic aging dynamics and the dashed lines are guides to the eye.

To illuminate this transition from transient to permanent change, I compare the recovery paths of perturbed glasses in a wide parameter range to those of unperturbed control samples. I calculate the τ_α dynamics of a just-quenched glass by averaging results of six simulations. I find the known power law behavior with aging exponent $\mu \simeq 0.89$ and refer to it as the “generic” aging scenario $\tau_\alpha^0 \propto t_w^\mu$ [26, 50] (⁰ indicates generic behavior). In fig. 3.4 the generic aging is indicated as a continuous black line and the inset shows the relaxation time of unperturbed glasses: The initial value depends on the wait time and the power law behavior is seen for $t > t_w$. In the main graph I collapse this data by rescaling with the total age $t_a = t_w + t_s$ and τ_α^0 at this age. The dashed lines are guides to the eye and illustrate the ideal path of unperturbed glasses until the power law behavior is resumed at their intersection. Changes introduced by mechanical perturbation can therefore be seen as departure from this expected path. The applied rescaling allows me to compare glasses of all ages and with varying time intervals of stress application t_s .

3.2. Recovery of the relaxation time

In fig. 3.5 I show the evolution of the relaxation time of mechanically perturbed glasses in the recovery regime. The results were gathered from simulations with parameters $10^3 \leq t_w \leq 10^5$ and $0.1 \leq \sigma \leq 0.6$. I find that the magnitude of change from the unperturbed behavior is best characterized by the total strain ϵ at the end of creep - not the stress amplitude. Note that the further away τ_α is from the horizontal dashed line, the stronger the impact of the perturbation, and the larger the corresponding strain. Indeed one can identify three recovery behaviors in fig. 3.5 which are indicated by coloring: The green curves ($\epsilon \leq 1\%$) are in close proximity to the dashed line and the relaxation time stays constant at timescales smaller than the glass age t_a . This means that creep with small total strain has little impact on the glass and the behavior essentially equals that of an unperturbed sample. At intermediate strains $1\% \leq \epsilon \leq 3\%$ (blue curves) the initial τ_α is at a lower value but it begins to evolve *before* reaching the black line. The merger with the generic glass behavior however, only takes place at the intersection of the dashed lines. This indicates timescales around the original glass age and the implications are discussed in the next paragraph. Finally, the red curves indicate that the largest strains $\epsilon \geq 3\%$ yield the lowest τ_α . Remarkably, the relaxation times of these strongly perturbed glasses do not begin to evolve immediately but stay approximately constant until reaching the generic aging dynamics which is then followed. This is the behavior that is expected for a younger glass, i.e., I observe mechanical rejuvenation.

To better understand the recovery behavior observed in fig. 3.5, I show a sketch of idealized paths in fig. 3.6. As before, the diagonal black line indicates the generic aging dynamics and path (o) would be followed by an unperturbed glass. I have shown that mechanical perturbation results in a shift towards lower τ_α , which is the starting point of possible recovery scenarios: path (a) is a fast return to the original (unperturbed) aging trajectory. This is an idealized example of a memory effect and not observed in the simulations. The glass *remembers* its age and the appropriate relaxation time is recovered on timescales that are small compared to the aging dynamics. Path (b) also exhibits dynamics on smaller timescales, but it merges with the original aging trajectory at a later time. Indeed the intersection is at times of the order of the glass age, whereupon the power law behavior is resumed. This timing shows that the original age is still remembered by the perturbed glass. By comparing fig. 3.5 and fig. 3.6 it is easy to see that glasses with intermediate total strain (blue) follow this path. Similarly, the recovery from large strains (red) is found to follow the third idealized trajectory (c). The

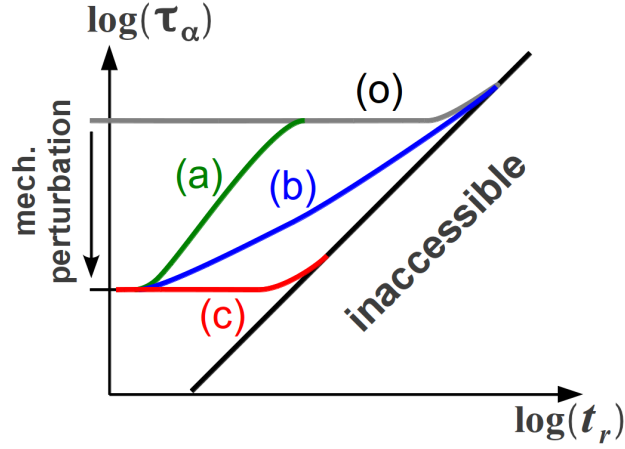


Figure 3.6: Sketch of possible recovery paths of the α -relaxation time. Line (o) is the path of an unperturbed glass and lines (a)-(c) are possible paths of glasses after mechanical perturbation. The diagonal black line indicates the generic aging dynamics.

relaxation time essentially stays constant until the generic aging behavior is reached. The merger happens at times that are smaller than the original age, which apparently indicates a loss of memory, i.e., mechanical rejuvenation. However, it is important to realize that no curve in fig. 3.5 truly enters the region to the right of the black line. The reason for this lies in the non-equilibrium nature of glasses. The evolution of τ_α is driven by the relaxation towards equilibrium and a given value can only become stable when thermodynamic equilibrium is reached. Since for an ideal glass this state is never reached, the black line acts as an upper time limit for the impact of memory effects, which is the recovery of remembered age and corresponding τ_α . Furthermore, dynamics on very small timescales (ballistic regime) can not alter the relaxation time, because collective motion is required. This means that a lower initial τ_α gives the glass less time to act on its memory. As a result, a strongly perturbed glass that has a small initial relaxation time but that still remembers its original age behaves very similar to a truly rejuvenated glass when viewed only from this dynamical perspective.

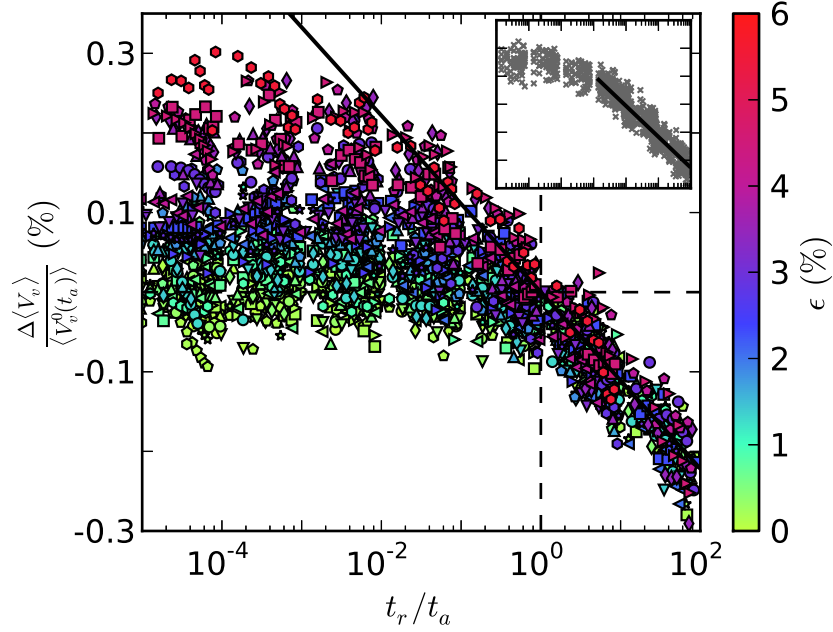


Figure 3.7: Percentage change of the rescaled average Voronoi cell volume with respect to the “generic” value $\Delta\langle V_v \rangle = \langle V_v(t) \rangle - \langle V_v^0(t_a) \rangle$ at glass age $t_a = t_w + t_s$. Shown in the main graph is the evolution of mechanically perturbed glasses in the recovery regime. The coloring represents the total strain at time of unloading. The continuous line indicates the generic aging dynamics and the dashed lines are guides to the eye. The inset shows the evolution of the average cell volume for just-quenched glasses and the black line is a logarithmic fit that yields the generic aging dynamics.

3.3 Recovery of the local structure

Identifying structural quantities that are equally sensitive to aging has proven to be difficult. No power-law behaviors similar to that of the α -relaxation time are known. I am, however, able to find measures of the local structure with logarithmic dependencies on the glass age. I calculate a variety of such quantities to better characterize the recovery path after deformation and the underlying thermodynamic state. Similar to the relaxation time analysis, I approximate the “generic” aging behavior (indicated via superscript ⁰) and compare this to the evolution after deformation. To perform a combined analysis for varying stress amplitudes and glass ages (see section 3.2 for parameter ranges) I use the same rescaling approach as for τ_α . Note that in the case of logarithmic dependencies, the rescaling yields a change of the generic aging slope (continuous black line in fig. 3.7 and following). I still use the approach, however, because the evolution during aging and therefore the change of the slope is small.

I first study the decrease of local volume during aging in the NPT ensemble by performing a Voronoi tessellation on configuration snapshots and calculating the average cell volume $\langle V_v \rangle$ [78]. The Voronoi tessellation divides space into cells around the particle locations, and each cell is that part of space that is closest to a single particle. In the main graph of fig. 3.7 I show the recovery paths after creep for the same simulations as in fig. 3.5. As before, the horizontal dashed line indicates the expected path of an unperturbed glass until the intersection with the continuous black line, which indicates the generic aging behavior. The calculation of the generic aging $\langle V_v^0 \rangle$ is shown in the inset of fig. 3.7 and this is exemplary for all quantities with logarithmic dependency on the glass age: I combine the simulation data of six just-quenched glasses and fit for the slope of the emerging logarithmic behavior. In the main graph, the coloring again indicates the total strain at time of unloading. One can clearly see that the deviation from the unperturbed path increases with increasing strain, which agrees with the results from the dynamical perspective. I also observe the merger of red (large strains) recovery paths with the continuous line at timescales smaller than t_a , indicating erasure of memory.

In the absence of long range order, which is the case for glasses, the local spatial order is important for the characterization of the thermodynamic state. I calculate three measures of the local structure that are sensitive to aging and their recovery paths are shown in fig. 3.8. Since I focus on

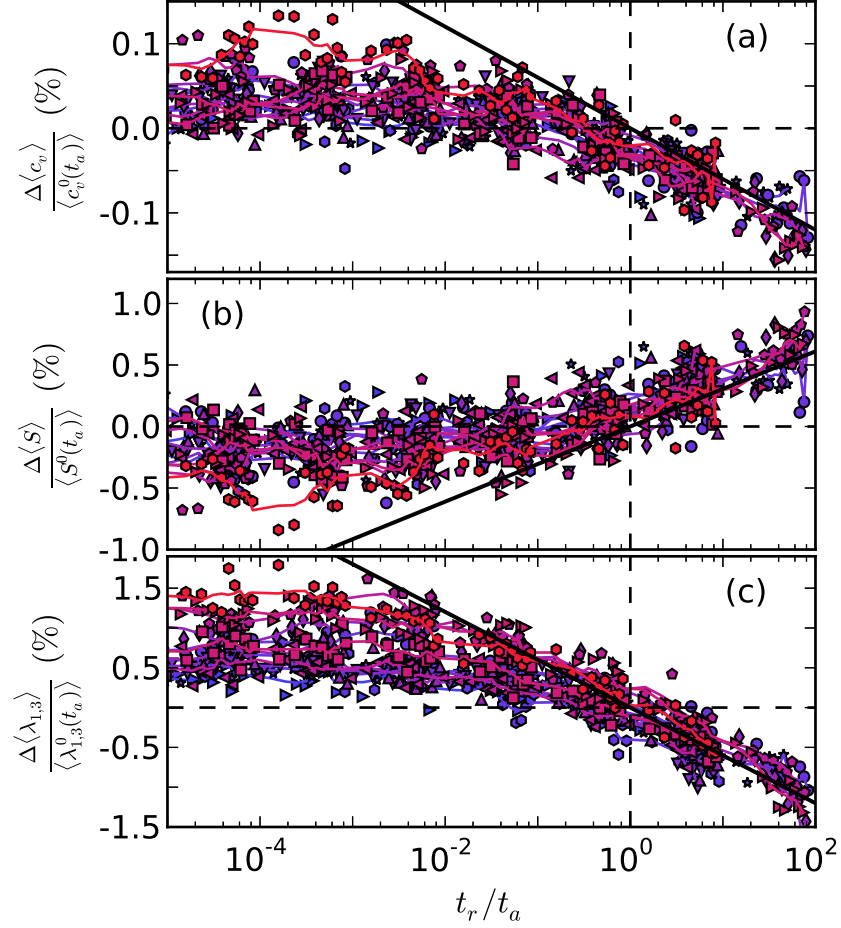


Figure 3.8: (a) Difference in the coordination number $\Delta\langle c_v \rangle = \langle c_v(t) \rangle - \langle c_v^0(t_a) \rangle$, (b) triangulated surface order parameter $\Delta\langle S \rangle = \langle S(t) \rangle - \langle S^0(t_a) \rangle$, and (c) evolution of the eigenvalue difference $\Delta\langle \lambda_{1,3} \rangle = \langle \lambda_{1,3}(t) \rangle - \langle \lambda_{1,3}^0(t_a) \rangle$. All three quantities are rescaled percentage changes with respect to the “generic” value at glass age $t_a = t_w + t_s$. The coloring represents the total strain at time of unloading (see e.g., fig. 3.7). The continuous line indicates the generic aging dynamics and the dashed lines are guides to the eye.

mechanical rejuvenation and because the data is relatively noisy, only the results for strains $\epsilon \geq 2.5\%$ are shown. In panel (a) one can see the evolution of the average coordination number $\langle c_v \rangle$, i.e., the number of beads that form the nearest neighbor shell which is calculated using the Voronoi tessellation. I find that the number of participating beads is decreasing with increasing glass age and that an increase in strain leads to larger coordination numbers. In panel (b) I show the recovery paths of the triangulated surface order parameter

$$S = \sum_q (6 - q) \nu_q,$$

which is sensitive to short range order and often used in the study of amorphous metals [82, 99]. Here q is defined for each bead in the coordination shell as the number of nearest neighbors that are also part of the shell, and ν_q is the number of beads in the shell that have the same q . This order parameter decreases during aging, which is a sign of increasing order and packing fraction. I find that $\langle S \rangle$ is larger after mechanical deformation and that the recovery path for large strains is similar to that of younger unperturbed glasses. The third structural quantity that is shown is the averaged difference between the biggest and the smallest eigenvalue of the moment of inertia tensor of the cages $\langle \lambda_{1,3} \rangle = \langle \lambda_1 - \lambda_3 \rangle$. The Voronoi tessellation identifies the cage for each bead and after setting the origin of the coordinate system to the position of the central bead, I calculate the tensor using the positions of all beads that form the cage. I find that all eigenvalues decrease with glass age, and more importantly that all *differences* exhibit a logarithmic dependency as well. This means that the aging dynamics manifest in a change of the cages towards a more spherical shape. In fig. 3.8(c) I only show the evolution of $\langle \lambda_{1,3} \rangle$ and the just discussed “generic” aging behavior is again indicated by the continuous black line. The observed paths resemble the expected behavior of younger unperturbed glasses, which indicates mechanical rejuvenation. All of these measures of local order show the now familiar dependence on strain, i.e., increase in strain yields further distance from the unperturbed aging path.

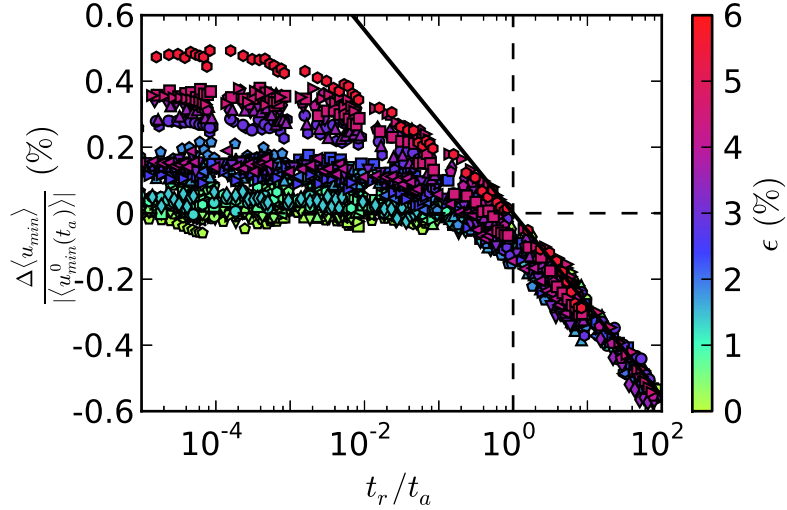


Figure 3.9: Percentage change of the difference between the minimized potential energy of a mechanically perturbed glass $\Delta\langle u_{min} \rangle = \langle u_{min}(t) \rangle - \langle u_{min}^0(t_a) \rangle$ and the “generic” behavior at glass age $t_a = t_w + t_s$. Shown is the evolution of the potential energy landscape in the recovery regime. The coloring represents the total strain at time of unloading. The continuous line indicates the generic aging dynamics and the dashed lines are guides to the eye.

3.4 Recovery in the potential energy landscape

The potential energy is another quantity that is sensitive to aging, and the depth of the occupied minima in the potential energy landscape has been the focus of previous studies [54, 62, 92]. I explore this third perspective on the recovery paths by investigating the evolution of the inherent structure energy $\langle u_{min} \rangle$ in the recovery regime. The inherent structure is the particle configuration in the zero temperature limit. The calculations are performed using a gradient descent algorithm on spatial configuration snapshots, which yields results in agreement with the potential energy after a very fast quench to zero temperature. In analogy to the analysis of the local structure (see section 3.3), I calculate the “generic” aging behavior $\langle u_{min}^0 \rangle$ and rescale the recovery paths of simulations with varying stress amplitudes and glass ages

to allow a direct comparison.

In fig. 3.9 I show the recovery of the inherent structure energy of mechanically perturbed glasses after unloading. As before, the horizontal dashed line marks the expected path of an unperturbed glass and the continuous black line is the generic aging behavior. The shown energies are calculated solely from contributions of non-bonded beads, since the stiff springs between bonded monomers do not age. I find that the depths of the minima decrease with increasing total strain, which is indicated by color code. The green curves ($\epsilon \leq 1\%$) closely follow the horizontal dashed line and cross over to the generic behavior at times of the order of the glass age. This indicates that the mechanical perturbation was too weak to yield changes in the aging dynamics. For intermediate strains $1\% < \epsilon < 5\%$ (blue and purple) I observe a decreased initial depth of the minima $\langle u_{min} \rangle$ and the onset of dynamics at times smaller than t_a . However, in agreement with the relaxation time dynamics and the evolution of the local structure, I find that the merger with the generic dynamics takes place at timescales similar to the glass age. The recovery paths at larger strains (red) resemble the expected paths of younger unperturbed glasses: An initially constant behavior is followed by the crossover to the generic aging at timescales *smaller* than the original age of the glass, suggesting mechanical rejuvenation.

3.5 Recovery after constant strain rate deformation

Deformations in the creep protocol are restricted to around the yield point, because the onset of flow introduces numerical instabilities in the barostat, see also section 2.3. I extend the range of analyzed strains by deforming at a constant strain rate as shown in fig. 3.1(b), and results in the recovery regime are shown in fig. 3.10. In close analogy to fig. 3.5, the α -relaxation time in panel (a) decreases with increasing total strain. Although results for different strain rates and wait times again collapse for the same amount of strain, I note that the α -relaxation time begins to change noticeably only for strains greater than $\sim 2\%$. This observation points to some differences between the two deformation protocols that require further investigation.

Focusing on the regime of strains larger than 6%, I find that the recovery paths saturate and cannot enter the region to the right of the generic aging

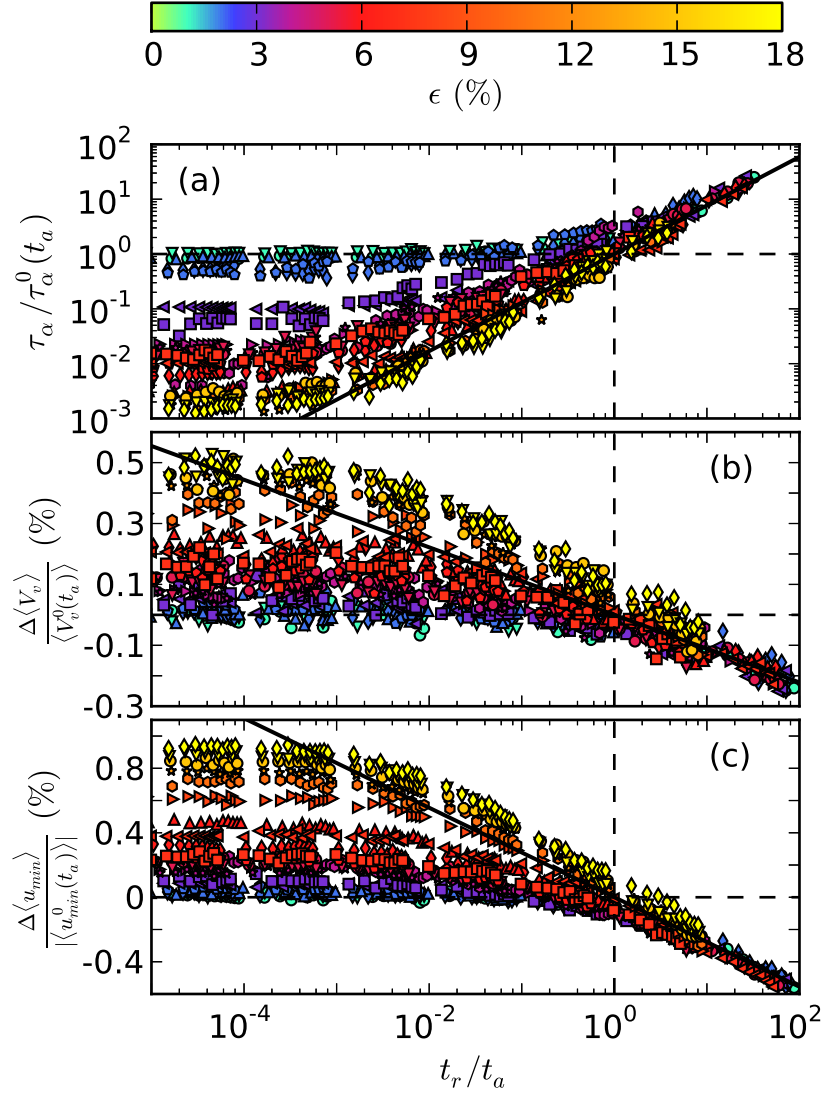


Figure 3.10: Evolution of (a) α -relaxation time, (b) Voronoi cell volume, and (c) inherent structure energy in the recovery regime after deformation with constant strain rates $\dot{\epsilon} = 10^{-5}$ and 10^{-6} and two waiting times (glass age $t_a = t_w + t_s$). (b) and (c) are percentage changes as defined in fig. 3.7 and fig. 3.9, and the coloring represents the total strain at time of unloading. The continuous lines indicate the generic aging dynamics and the dashed lines are guides to the eye.

curve (thick solid line) as explained before. By contrast, I show in panel (b) that the Voronoi volume can be driven beyond the range covered by unperturbed aging dynamics. This is clearly visible for strains $\epsilon > 12\%$, as the recovery paths overshoot the generic aging curve. It signifies that I find cell volumes at time scales at which unperturbed aging would have relaxed them to smaller sizes. With regard to the parameters describing local order (see fig. 3.8), I find a similar overshoot in the recovery curves of the eigenvalue differences, but not for the coordination number and triangulated surface order parameter (not shown). I suspect that these quantities would also begin to show overshoots for even larger deformations.

Finally, the inherent structure energy shown in panel (c) also exhibits a recovery path that enters the regime inaccessible to unperturbed aging. This crossing of the generic aging behavior indicates that strongly perturbed glasses ($\epsilon > 12\%$) remain at a point in the potential energy landscape for a time period that would be sufficient for an unperturbed system to relax to a lower energy minimum. This implies that the state after deformation is distinct from that of a younger glass.

3.6 Conclusions

I investigate the recovery of polymer glasses from uniaxial tensile creep deformation via molecular dynamics simulations. The impact of mechanical perturbation on the aging dynamics is analyzed by comparing the recovery paths after deformations of different duration and stress amplitude to the behavior of unperturbed control samples. The evolution of α -relaxation time, inherent structure energy and measures of local spatial order are monitored, and they give three different perspectives on perturbed glasses. In the regime of negligible aging during deformation, all the data suggests that the impact of deformation on the aging behavior is described solely by the total engineering strain ϵ at the end of the deformation, i.e. an increase in strain yields a recovery path further away from the unperturbed control path. I find a clear progression from seemingly no impact at $\epsilon \leq 1\%$ to transient changes at $1\% \leq \epsilon \leq 3 - 5\%$ and finally permanent alterations of the glass history at larger strains. This transition from “transient rejuvenation” to full “erasure” of aging is *continuous* and the onset of permanent changes is around the yield strain [76].

I propose to distinguish between transient and permanent changes of the

3.6. Conclusions

glass memory by identifying the timescale at which a perturbed glass recovers the aging behavior known from unperturbed samples. If this timescale is around the full age $t_a = t_w + t_s$, then the glass has preserved its memory. On the other hand, if the timescale is smaller than t_a , then the glass history has been altered. I visualize this measure of memory effects in fig. 3.6. For samples deformed via tensile creep to strains of 3–6%, all quantities indicate permanent rejuvenation as defined above. This agreement of dynamical, structural, and energetic criteria suggests that the underlying thermodynamic state is indeed similar to that of a younger glass. Simulations at constant strain rate were used to perform deformations beyond the yield strain. The results for the recovery after post-yield deformation show a distinct behavior: The evolution of the α -relaxation time still suggest rejuvenation and a state equivalent to a younger glass. Structural and energetic quantities, however, can be driven beyond the range accessible to younger glasses. This indicates that a distinct thermodynamic state is reached after deformations in the post-yield regime.

The creep deformation protocol used here closely followed that of recent experimental studies [58]. The results are in agreement with earlier studies in so far, as in observing transient changes of the aging dynamics in the sub-yield regime and permanent changes in the post-yield regime. Additionally, I show that the transition towards permanent mechanical rejuvenation is continuous, and that its only control parameter is the total strain at the end of the deformation. This finding supports an earlier study that reports the importance of strain in describing accelerated dynamics during deformation [100].

Chapter 4

Spatio-temporal correlation of structural relaxation events²

This second project explores dynamical heterogeneity (DH) in polymer glass, and this central feature of glassy dynamics is discussed in detail in section 1.2.3. The dynamical activity in glasses is heterogeneously distributed, with some regions undergoing rapid structural rearrangements, while other regions remain structurally mostly static. The heterogeneity manifests in cooperative motion of rearranging particles [33, 51], and four-point correlation functions have been used to quantify DH in terms of a dynamical susceptibility χ_4 [9, 53], which is proportional to the volume within the glass that exhibits correlated dynamics.

This study gives a new, spatially resolved perspective on DH by reducing the particle motion to local structural relaxation events. As discussed in section 1.2.1, the particle dynamics in glasses is dominated by vibrations in metastable cages that is interrupted by rearrangements of the local structure. In section 2.6 I introduce a new algorithm that detects rapid changes in the particle trajectories, which is the signature of cage escapes or *hops*. Using this algorithm I can record a list of all hops that happen during a simulation run. Each hop is characterized by a time, the initial and final position of the particle (see section 2.6 for definitions) and the particle index. In fig. 4.1(a) I show a snapshot of the whole system followed in fig. 4.1(b) by a reduced picture where only particles are shown that hop at that time step. The comparison highlights the sparseness of the effective dynamics, showing a reduction from 50000 to four particles. By merging all hops that were detected in a time window of $3000\tau_{LJ}$ I directly reveal in fig. 4.1(c) the heterogeneous distribution of hops and their grouping into clusters, i.e. I directly show the dynamical heterogeneity in the glass resolved to individual structural relaxation events.

The study focuses on glasses in the quiescent state at three tempera-

²Large parts of this chapter have been published in ref. [85]

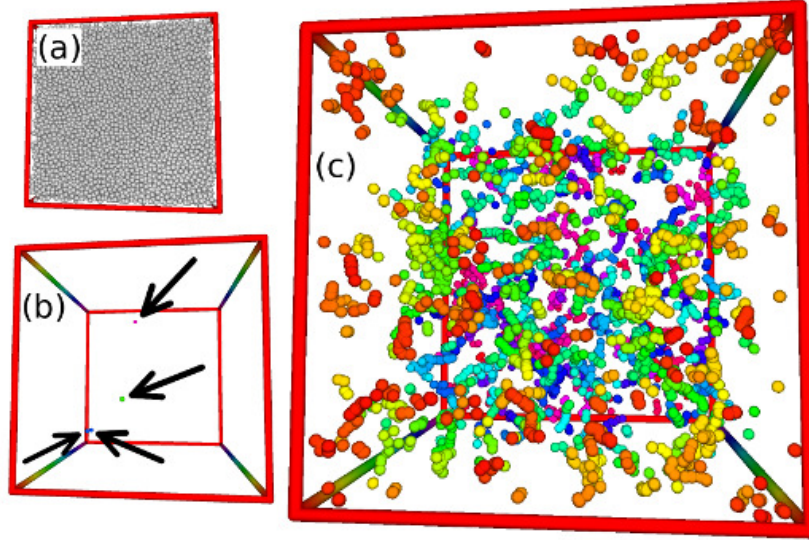


Figure 4.1: Snapshots of a single configuration showing (a) all particles and (b) only those particles that are in the middle of a hop. There are only four hops at that time step and their positions are highlighted by arrows. (c) shows all hops that are detected in a time window of $3000\tau_{LJ}$. The configurations are taken from a glass at $T = 0.2$ and age $t_a = 20000$.

tures $T = 0.2, 0.25, 0.3$ ($T_g \simeq 0.35$ [76]) in the aging regime. To increase the accuracy of the analysis I performed 11 independent simulation runs for temperatures $T = 0.25, 0.3$ and I report averaged results with error bars indicating the standard error. The results are separated into two parts. In the first section, I analyze the hop statistics and the dependence on temperature and age. Hop frequency, persistence time in cages, hop distance as well as direction are discussed, and a comparison to earlier studies is made that used different detection algorithms and monitored hops on subsets of the particles in the simulation. The main result of this section is the calculation of the spatio-temporal density-density correlation of hop events. I furthermore quantify collaborative motion in the polymer glass and identify temperature- and age-dependence. In the second part, I focus on DH in the aging regime. This regime has only recently been explored using three- and four-point correlators [17, 71], finding indications for an increase of dynamical correlation with age. On the basis of our hop detection, I calculate the four-point dynamical susceptibility χ_4 as the standard measure for correlated dynamics

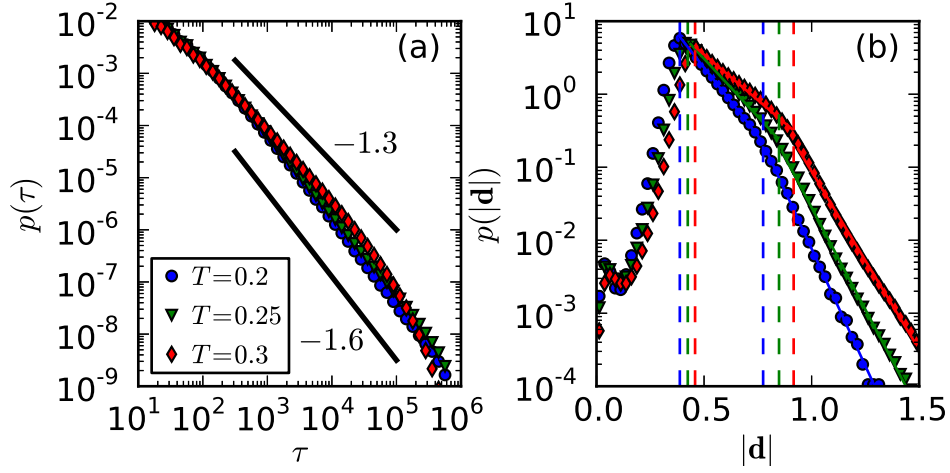


Figure 4.2: (a) Distribution of persistence time τ of cages at three temperatures. The solid lines indicate power laws. (b) Distribution of hop distances $|d|$, i.e., the distance between old and new cage. Exponential fits are indicated by the solid lines and the vertical dashed lines indicate $\sqrt{P_{th}}$ and $2\sqrt{P_{th}}$ for the respective temperatures; see legend in panel (a). Error bars in both plots are smaller than the markers and are omitted for visibility.

and directly compare it with the aggregation of hops into clusters, which is the manifestation of DH in the hop picture. With this spatial resolution of DH I calculate the full volume distribution of hop clusters and give a measure of their compactness.

4.1 Statistical properties of hops

The non-equilibrium nature of glasses gives rise to a continuously slowing structural relaxation with increasing age. The caging plateau in the mean squared displacement, see section 1.2.1, extends to longer times with increasing age, which suggests an increasing time that a particle remains in its cage. This *persistence time* is measured as the time between two consecutive hops of the same particle. Aging is caused by a broad distribution of persistence times and previous studies have found a power law $p(\tau) \propto \tau^\mu$ with exponent $-1 > \mu > -2$ in simulations of polymer glasses and binary mixtures [98]. In a very recent study this broad distribution was also found in simulations of a strong glass former [97], although with exponent $-0.3 \geq \mu \geq -1$.

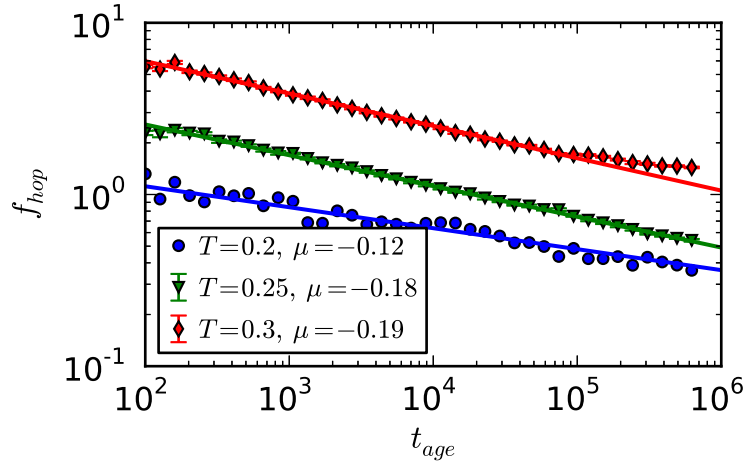


Figure 4.3: The hop frequency f_{hop} in units $1/\tau_{LJ}$ over the duration of the simulation run in a log-log plot. Solid lines indicate power-law fits with exponents μ given in the legend.

In fig. 4.2(a) I show the persistence time distribution for quiescent glasses at three temperatures $T = 0.2, 0.25, 0.3$. I find a power-law behavior with $\mu \simeq -1.5$ insensitive to the glass temperature, which agrees well with the previously found value for polymer glasses of -1.23 [98]. The slightly smaller value is probably due to the increased sensitivity of the detection algorithm, which increases the likelihood of shorter persistence times. The shortened tail observed for $T = 0.3$ indicates that persistence times in this system are sampled from a finite distribution and hence the system will equilibrate at long times (see also ref. [97]). However, since the turnover happens at times of the order of the total simulation time, during the observation time window the system is still well within the aging regime.

During a hop, the particle moves from one metastable local configuration to another, i.e., from one cage to the next. The detection algorithm estimates both locations \mathbf{r}_{init} , \mathbf{r}_{final} and I can therefore calculate the hop distance

$$|\mathbf{d}| = |\mathbf{r}_{final} - \mathbf{r}_{init}|. \quad (4.1)$$

In panel (b) of fig. 4.2 the distribution of the hop distance is shown for three temperatures. For each glass, the main peak is located at $\sqrt{P_{th}}$ (the first vertical dashed line), which is the minimal distance that the detection algorithm sets for the separation of two ideal cages. I find an exponential

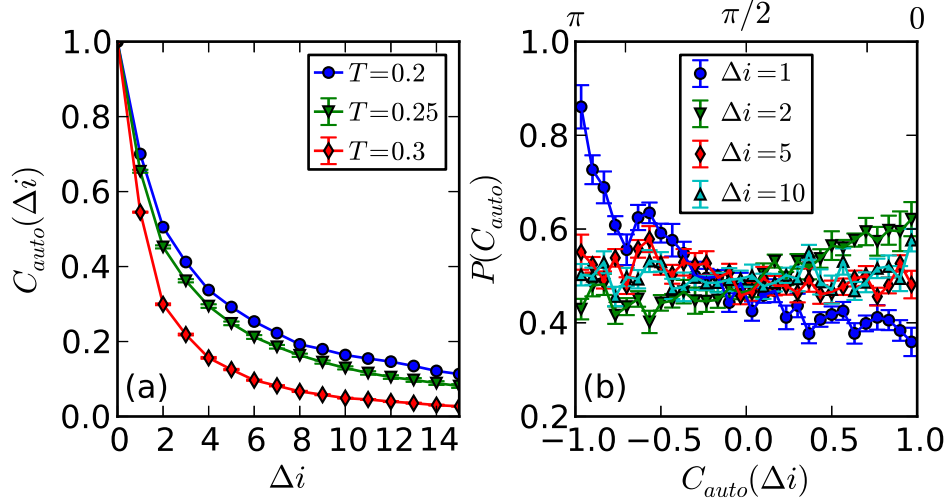


Figure 4.4: Hop displacement autocorrelation for three glass temperatures at age $t_{age} = 10^5$ (a) as function of number of hops separation and (b) as histogram, that is calculated using normalized displacement vectors ($T = 0.25$ and age as above) and reveals an anisotropy in the direction of consecutive hops. The lines are guides to the eye.

decay following the peak, with a transition to a faster exponential decay at around $2\sqrt{P_{th}}$. The transition is expected, because at distances $> 2\sqrt{P_{th}}$ it is possible for the detection algorithm to separate the particle motion into two hops, if the particle briefly stabilizes at an intermediate distance. The form of the distribution is qualitatively unchanged for varying temperatures, suggesting that the hop process is unchanged inside the glass state. Indeed, in simulations of a strong glass former [97] a comparable distribution was found, indicating a similar role of the hop process.

In fig. 4.3 I show the hop frequency of the glass, i.e. the number of hops per time τ_{LJ} . I observe about six times more hops at $T = 0.3$ compared to $T = 0.2$. Furthermore, I find that the frequency decreases as a weak power law with age. Aging is accelerated at higher temperatures, which indicates that the phase space is explored more quickly. Indeed, for the glass closest to the glass transition ($T = 0.3$), I observe a flattening of the curve, i.e. the simulation reaches timescales close to the end of the aging regime.

I can further characterize the hop process by calculating the autocorrela-

tion

$$C_{auto}(\Delta i) = \frac{\langle \mathbf{d}_i \cdot \mathbf{d}_{i+\Delta i} \rangle}{\langle \mathbf{d}_i \cdot \mathbf{d}_i \rangle} \quad (4.2)$$

of the displacement vector \mathbf{d} [see eq. (4.1)]. The average in the numerator is taken over all hop-pairs i of a particle with a separation Δi , the average hop direction is zero and the denominator is the variance of \mathbf{d} with zero mean. Simple mean-field trap models [67] assume a solely temperature driven escape from the cage, which yields independent hops, and a previous study indeed found a vanishing autocorrelation after about two hops [98]. Although the earlier study used a different hop detection algorithm with lower sensitivity, our results shown in fig. 4.4(a) principally agree with these findings. We observe a correlation that decreases below 0.2 after at most seven hops, with a more rapid decline at higher temperatures. The decay is slower than previously found, because the detection algorithm used here is able to separately pick up back-and-forth hops of a particle between the same two cages. I confirm this observation with the autocorrelation histogram in fig. 4.4(b), where the displacement vectors were normalized to unit length. This isolates the directional correlation of the hops and one can clearly see a pronounced anisotropy. For consecutive hops I find that angles close to 180° are clearly favored, indicating that the particle is more likely to return to the location where it came from. Furthermore, there is an increased probability for a following third hop to be in the same direction as the first, indicating a back-and-forth between the two cages. The anisotropy is subdued with increasing separation of hops and vanishes at $\Delta i = 5$ for a glass at $T = 0.25$.

Up to this point the results took advantage of the increased sensitivity and greater number of detected hops. However, since all particles are tracked, I am able to directly measure the spatio-temporal correlation of hops. In fig. 4.5 I present surface plots that visualize probable temporal and spacial distances between hops. I calculate the density-density correlation of hops along the lines of the normalized distinct part of the van Hove function [41]

$$G_d^{hop}(r, t) = \frac{1}{N'} \left\langle \delta \left(r - |\mathbf{r}_{init}^{(i)}(t') - \mathbf{r}_{init}^{(j \neq i)}(t' + t)| \right) \right\rangle. \quad (4.3)$$

Here the average is taken over all N' hop pairs that involve two distinct particles, and using the initial positions, i.e. the initial cages. Figure 4.5(a) shows an example probability distribution. I find a dominating peak at times close to zero and at a distance $\simeq 1$, which is caused by hops in the surrounding shell of particles. The accumulation of near-simultaneous hops is a direct

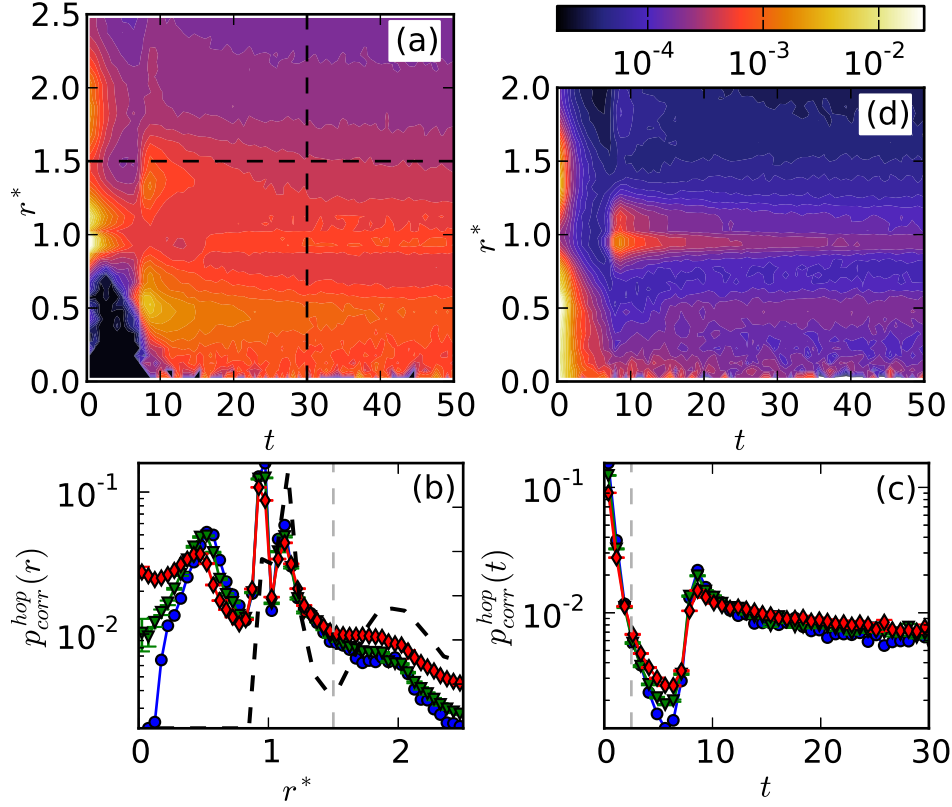


Figure 4.5: (a) Probability density surface for spatio-temporal separation of two different hopping particles based on Eq. (4.3) for a glass at $T = 0.25$ and $t_{age} = 10^5$. The color scale is logarithmic (scale at the top-right corner) and the dashed lines indicate integration limits used to calculate the one-dimensional probability functions (b,c). Center plots show the probability function of (b) separation and (c) time delay between hops for $T = 0.2$ (blue \bigcirc), $T = 0.25$ (green ∇), and $T = 0.3$ (red \diamond) at the same age. The gray vertical dashed lines in (b,c) illustrate the correlation ranges and the black dashed curve in (b) indicates the radial distribution function. (d) Probability density surface following Eq. (4.3) for the same glass as the left panel, but with r^* calculated from initial position (at the origin) to the final position of the second particle after the hop. The color scale is again logarithmic.

indicator of the cooperative nature of the hop process. The area $r \lesssim 0.7$ and $t \lesssim 7$ is empty, which is an effect of the excluded volume of the hopping particle at the origin. A secondary, at least an order of magnitude weaker peak is located around $r = 1/2$ and $t = 10$. It is caused by particles that hop after having entered the space that was vacated by the particle at the origin. A comparison of density-density correlations calculated at various ages (not shown) indicate that aging effects are minimal. To highlight the dependence on temperature I partially integrate eq. (4.3) from the origin to the dashed lines, which are chosen such that the main features are included. In fig. 4.5(b) I show the spatial correlation $p_{corr}^{hop}(r) = \int_0^{30} dt G_d^{hop}(r, t)$ for three temperatures. One can see that the main features are found at all temperatures and that an increased temperature weakens the sharpness of the peaks, which is due to the increased vibrational motion of the particles. Apart from the first peak at $r = 1/2$ (see above), I find peaks at positions that coincide with the static shell structure of the glass as indicated by the radial distribution function (black dashed curve). The splitting of the peak at around $r = 1$ is due to the different mean distance between particles that are neighbors in the same polymer backbone and particles that are not directly bonded to each other. The existence of the double peak shows that both pairs take part in cooperative rearrangements. Figure 4.5(c) shows the temporal correlation $p_{corr}^{hop}(t) = \int_0^{1.5} dr G_d^{hop}(r, t)$. A sharp decay at small times is followed by a peak at around $t = 9$, which is due to the immediate re-hopping of particles; the back-and-forth hopping that is also discussed in connection with the hop autocorrelation (see above). The position of the peak, i.e. the secondary peak in the probability density surface is directly linked to the maximal resolution of two consecutive hops, which is $t = 7.5$ for the used parameters (see sec. 2.6). I find only a very weak temperature dependence in the temporal correlation, suggesting that the fundamental mechanisms of cooperativity are the same over the temperature range studied here. The data also does not show any clear indication for Poisson processes like those found for supercooled liquids and granular matter [19, 21]. Based on the sharp drop following the main peak in the spatial probability distribution, I infer a correlation range of $r_{corr} = 1.5$ [fig. 4.5(b), vertical dashed line], i.e., the correlation does not extend beyond the nearest neighbor shell. From the temporal probability distribution I determine a correlation range of $t_{corr} = 2.5$ [fig. 4.5(c), vertical dashed line], which is the time at which the initial peak has decayed to values below the close to constant region after the second peak. These ranges

therefore restrict “correlated” hops to near-simultaneous hops of neighboring particles, as indicated by the primary peak in the density-density correlation.

Knowledge of the final position of hopping particles also allows me to explore the direction of correlated hops. The probability distribution surface in fig. 4.5(d) shows a density-density correlation very similar to the one on the left. Again I use eq. (4.3), but the distance is now calculated between initial cage at the origin and the *final* position of other hopping particles $\mathbf{r}_{final}^{(j \neq i)}$. Therefore, high probability regions indicate where the particles end up after a correlated hop. By comparing the surfaces, I find that hops that started in the first shell (the primary peak in left plot) mostly end at $r \lesssim 1/2$, see the primary peak in the right plot. Indeed this peak extends all the way to $r \simeq 0$, indicating that it is possible for the cage at the origin to stay largely intact with a new particle taking the place of the last one. This suggests the string-like motion that was previously observed in a binary LJ mixture [33]. We also find a secondary peak at a distance $r \sim 1.5$, which suggests that some hops from the first shell are directed away from the cage at the origin. Please note that the color scale in the plot is logarithmic, and that this second *hop destination* is at least one order of magnitude less likely than the first one. The secondary feature in fig. 4.5(d) at $t \sim 10$ is located around $r = 1$, confirming that the accumulation of hops at this time lag are due to back-hops of particles that return to the first shell after having hopped into the vacated volume closer to the center of the cage (origin).

The correlation ranges $r_{corr} = 1.5$ and $t_{corr} = 2.5$ allow me to identify “co-operatively rearranging” groups of particles and I perform a cluster analysis to measure their size. Two particles are in the same cluster if they are closer in space and time than r_{corr} and t_{corr} , which is in close analogy to Candelier et al.’s study [19]. In fig. 4.6 I show the measured cluster size distributions, which exhibit initial exponential decays with stretched tails that approach a power law. In the main panel I show results for a single temperature and varying age, and one can see that as the age increases the distribution flattens and becomes more exponential-like. In an older glass the hop-activity is reduced (see hop frequency in fig. 4.3), and therefore the constant clustering time (t_{corr}) used here results in a lower likelihood of finding larger clusters with growing age. Varying temperature at the same age has a similar effect: as temperature increases, I observe a broadening of the distribution away from exponential and towards a power-law form.

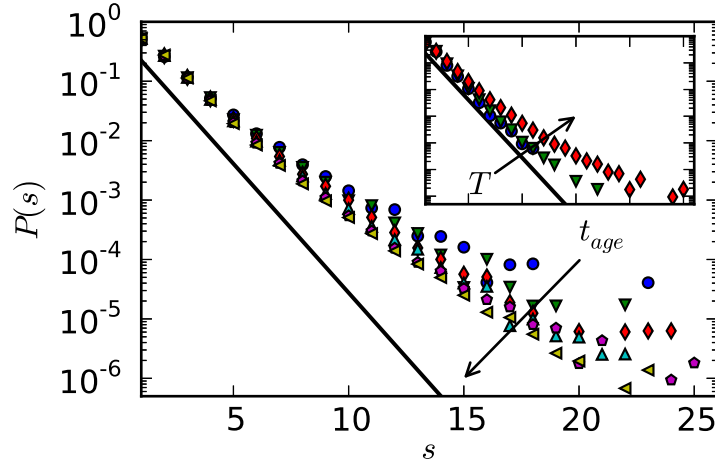


Figure 4.6: Size distribution of cooperatively rearranging particles. The main panel shows distributions at six ages for a glass at temperature $T = 0.3$; see legend in fig. 4.7. The inset shows the size distribution of three glasses at age $t_{age} = 10^5$ and temperatures $T = 0.2$ (blue \circ), 0.25 (green ∇), 0.3 (red \diamond). Both plots have the same axes ranges, and the solid black lines indicate $P(s) \propto \exp(-s)$.

4.2 Dynamical heterogeneity and clustering of hops

In previous studies the heterogeneous dynamics in glasses and supercooled liquids were mainly probed with four-point correlation functions. A standard approach is to measure the number of particles that remain approximately stationary as a function of time using overlap functions [53]. The variance of this quantity over a multitude of independent simulations is the four-point dynamical susceptibility χ_4 , which quantifies how many particles are moving substantially from their initial position in the same time window. The dynamical susceptibility exhibits a peak at the time of maximal dynamical correlation in the system. The peak height is connected to the number of particles with correlated dynamics, and the increase of that height when approaching the glass transition signifies growing dynamical length scales. With knowledge of the location and time of all hops in the system, I can provide a new perspective on the correlated dynamics. Specifically, I am

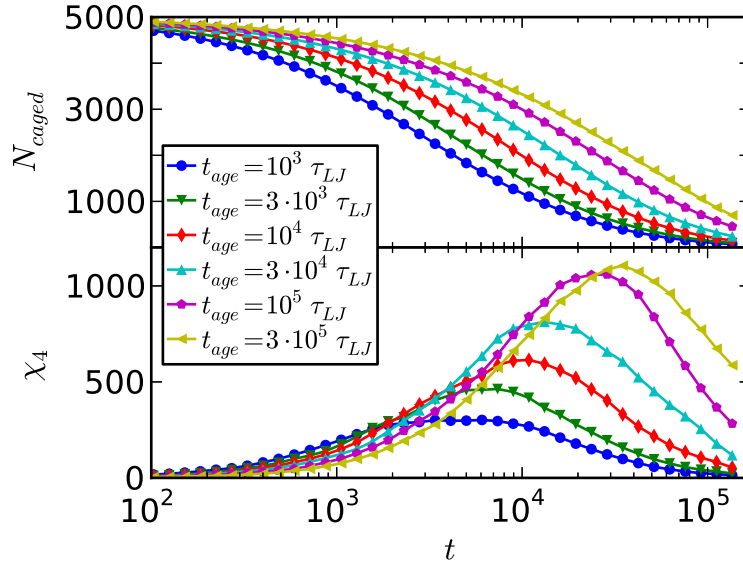


Figure 4.7: The top panel shows the number of caged, i.e. not yet hopped, particles N_{caged} averaged over independent simulations as a function of time for six glass ages. The four-point susceptibility χ_4 shown in the bottom panel is calculated from the variance of N_{caged} , eq. (4.4).

able to spatially resolve the clustering of hops, directly revealing the heterogeneous dynamics, and to study the cluster distribution as a complementary perspective to χ_4 . For this part of the study I focus specifically on the aging regime, for which few studies exist. The results shown below are calculated from a glass at $T = 0.3$, yet an equivalent analysis for $T = 0.25$ (not shown) confirms our findings further inside the aging regime.

In a first step, I calculate the number of particles that have *not* hopped directly from the hop data

$$N_{caged}(t, t_{age}) = \sum_i^N b_i(t, t_{age}) \quad (4.4)$$

where $b_i(t, t_{age}) = 0$ if particle i has hopped in the time window $[t_{age}, t_{age} + t]$ and $b_i(t, t_{age}) = 1$ otherwise. In the upper panel of fig. 4.7, I show results for six ages. I employed simulations of $N = 5000$ particles that are otherwise equivalent to the usual simulations with $N = 50,000$ particles. I had to downscale the system, because converged measurements of χ_4 required 300

4.2. Dynamical heterogeneity and clustering of hops

independent runs. As mentioned above, the four-point dynamical susceptibility is proportional to the variance of N_{caged} [53]

$$\chi_4(t, t_{age}) = \frac{\beta V}{N^2} (\langle N_{caged}^2 \rangle - \langle N_{caged} \rangle^2) , \quad (4.5)$$

with V being the simulation box volume, and $\langle \cdot \rangle$ representing an average over independent realizations of the system. The bottom panel of fig. 4.7 shows χ_4 as function of time for the same six ages. In an earlier study, Parsaeian and Castillo [71] investigated four-point correlations in the aging regime of a binary LJ glass, and I observe the same main features in fig. 4.7: a shift of the peak towards larger times with increasing age and an increase in height, indicating a larger volume of correlated dynamics.

To obtain a complementary picture of the *spatially resolved* dynamics, I perform a spatial cluster analysis on the subset of hops in the same time window $[t_{age}, t_{age} + t]$ that is used for the calculation of N_{caged} . I use a standard single-linkage cluster criterion, i.e., hops i and j are part of the same cluster, if the distance between the initial positions is below a threshold

$$|\mathbf{r}_{init}^i - \mathbf{r}_{init}^j| < r_{cl} .$$

If a hop k is already in a cluster with i , then hops j and k will belong to the same cluster even if they don't fulfill the above criterion. As a threshold I use the spatial correlation range that is obtained from the density-density correlation $r_{cl} = r_{corr} = 1.5$ (see previous section). As the time window is increased, I include more hops into the analysis and the clusters grow and merge.

In fig. 4.8 I illustrate the observed growth via snapshots of an example cluster at increasing time t . The cluster first consists only of a few hopping particles and successively grows into an extended structure. An animation of the growth of a single cluster over time reveals periods of near stagnation interrupted by large bursts which are due to the merging of simultaneously existing clusters. The plot in fig. 4.8 illustrates this intermittent growth process. It shows the cluster volume of 15 example clusters as a function of time. I define the volume of a cluster as the total correlated space of all hops that comprise the cluster

$$V_{cl} = \cup_i V_{sp}(r_{init}^i, r_{corr}) .$$

Each hop contributes a spherical volume V_{sp} with radius equal to the correlation range $r_{corr} = 1.5$ centered around the initial position of the particle. In

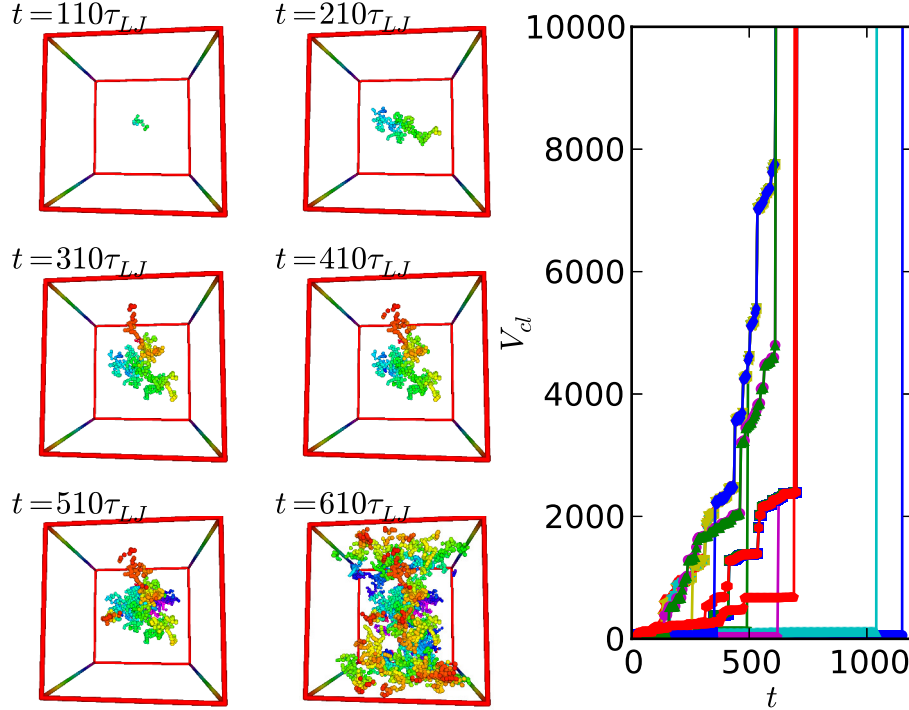


Figure 4.8: Snapshots of the growth of a single cluster over time. The particles are visualized at their initial positions (before the hop) and the coloring indicates depth. The plot on the right shows the cluster volume of 15 example clusters as a function of time. Examples were recorded at glass age $t_{age} = 10^5$.

other words, with each hop I associate the volume of the entire cage and the cluster volume is the union of all cages that have rearranged. To calculate this joined volume, I use a voxel technique, i.e. I partition the simulation box into small cubes (voxels) and count the number of voxels with a center closer than r_{corr} to any hop of a given cluster.

To explore the cluster configurations near the χ_4 peak I calculate the mean volume and number of clusters as a function of time, and results for six ages are shown in fig. 4.9. In the upper panel one can see that at long times I observe a single cluster that spans the simulation box, and its formation is shifted in time with increasing age. In the inset I show the same data with a time axis that is rescaled by the time of the χ_4 peak, which collapses the data onto a single master curve. Note that the dominating cluster emerges just

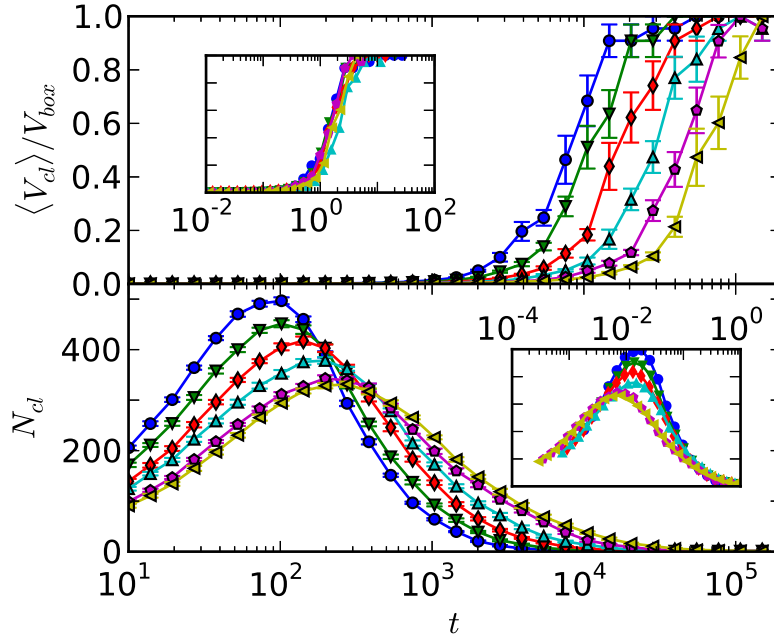


Figure 4.9: Mean cluster volume (top) given as a fraction of the total simulation box volume and the number of simultaneous clusters (bottom) as a function of time. Results for six ages are shown, see legend in fig. 4.7. The insets show data collapse when time is rescaled by the time of the χ_4 peak.

when the four-point susceptibility reaches its peak. The success of the scaling collapse indicates that aging merely delays, but does not otherwise alter the formation of this dominating cluster. The amount of clusters (bottom panel) peaks at much earlier times, and the rescaled data in the inset also shows an approximate collapse with age. Additionally, I find an age dependence of the peak height, showing that the maximal number of clusters decreases with increasing age.

To gain a more complete picture of the formed structures, I also measure the extent of the regions where no hops are detected. To quantify these “holes,” I use the same voxel partition and perform a nearest neighbor cluster analysis on the subset of voxels that does *not* lie inside the volume of any cluster. In fig. 4.10 I show the mean volume of the holes (top panel) and the number of holes (bottom panel) as a function of time. I find that with increasing time window, the size of the holes shrinks, which is of course due

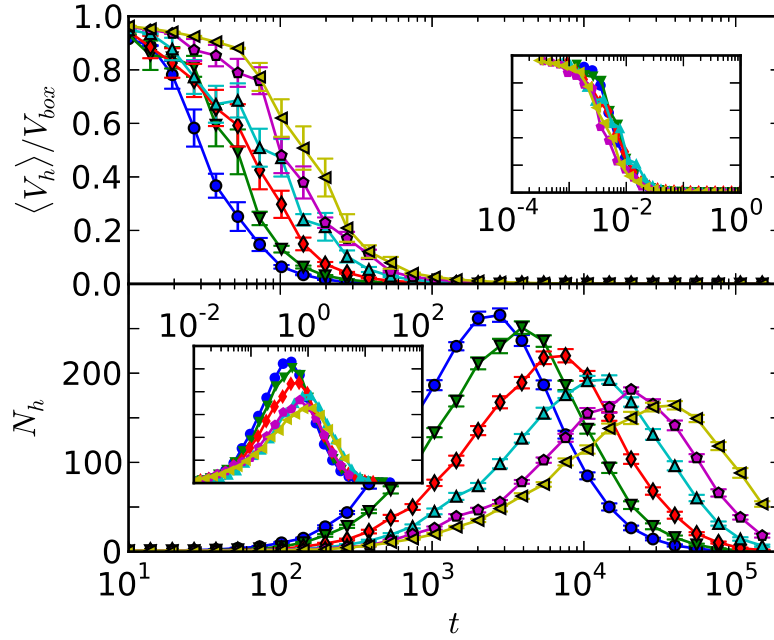


Figure 4.10: Mean hole volume (top) given as a fraction of the total simulation box volume and the number of simultaneous holes (bottom) as a function of time. Results for six ages are shown, see legend in fig. 4.7. The insets show data collapse when time is rescaled by the time of the χ_4 peak.

to the growing hop clusters. Again, I observe a shift with glass age towards larger times, and the inset in the top panel reveals that the break up of the single dominating hole happens just when the number of clusters is largest (both at $\sim 10^{-2}$ in rescaled time). In analogy, I find that the number of holes N_h is maximal just when the mean cluster volume diverges and therefore when χ_4 reaches its peak (see bottom panel inset). The maximum in N_h appears when the probability of *closing* a hole by placing a new hop into the system becomes larger than the probability of *splitting* a hole with a new hop. Therefore, the majority of the holes have shrunk to a size on the order of a single cage at the time of the χ_4 -peak. The time of this crossover shows the same age-dependence as χ_4 , yet I also find that the maximal number of holes decreases with age. The scaling behavior of the hole volumes with age mirrors the behavior of the cluster volumes, and further supports the interpretation that the geometry of DH is unchanged by aging.

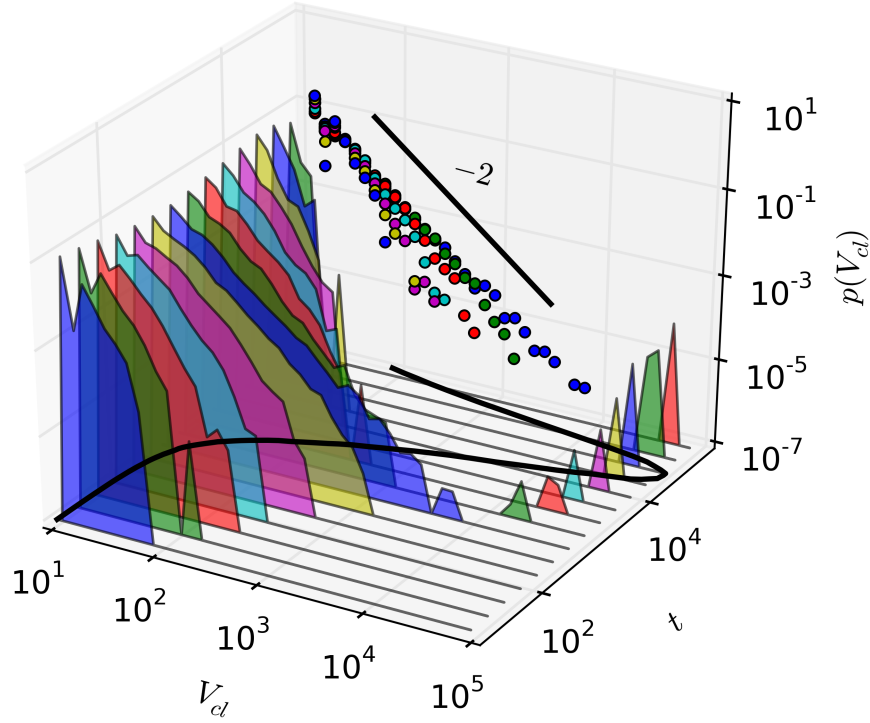


Figure 4.11: Collection of cluster volume distributions of a glass at age $t_{age} = 10^5$ measured at various times in double-log scale. Each distribution is plotted in the V_{cl} - $p(V_{cl})$ plane and placed along the t axis according to the size of the time window used for the cluster analysis. The back wall shows an overlay of distributions at small times in a single plane. I include data at times $\lesssim 10^3$ (up to and including the second blue distribution) and the same colors as the separate distributions are used to indicate the origin of the data points. The solid line on the back wall indicates a power law with exponent -2 . The black solid curve on the floor wall indicates χ_4 as a function of time.

The mean cluster volume already suggests a single, dominating cluster in the system when χ_4 is maximal. I gain further insight by directly studying the full distribution of cluster volumes. In fig. 4.11 I show its evolution for a single glass age, where the distributions for increasing time windows $[t_{age}, t_{age} + t]$ are stacked along the t axis. One can clearly see how the distribution lengthens over time until $\sim 10^3$. At this time (blue to green) the dominating cluster is formed, indicated by a detached peak at large volume and the successive shortening of the remaining distribution. The solid black curve on the floor wall indicates χ_4 as a function of time, and as the large cluster grows, so does χ_4 . The peak is reached when the dominating cluster essentially covers the whole volume. Furthermore, I analyzed the form of the distributions, which prior to the emergence of the dominating cluster follow a power law. On the back wall of fig. 4.11 I show an overlay of these early distributions (see caption) in a single plane. The overlay shows that the cluster volume distribution lengthens until a power law with exponent of approximately -2 is reached.

From the snapshots in fig.4.8, one can see that the clusters are not compact, but have a complex geometry. Parsaeian and Castillo investigated DH in an aging binary LJ glass using four-point correlators [71]. By assuming that the height of the χ_4 peak was proportional to the correlated volume and using an identified correlation range ξ , they found a scaling of $\chi_4^{peak} \propto \xi^b$ with $b = 2.89 \pm 0.03$. Our access to spatially resolved clusters allows us to directly calculate their fractal dimension and compare to this scaling result.

I use the box counting method [36], in which one covers the cluster with successively smaller cubes, counting each time how many boxes are needed. Here, a cluster is represented by its correlated volume, i.e., the union of spheres with radius 1.5 centered at each hop. The dimensionality of the cluster is then calculated via power-law fit

$$N_l \propto l^{d_f} ,$$

where l is the side length of the cube and N_l the cube count. In fig. 4.12 I show the fractal dimension as a function of time for six ages. I find a mean fractal dimension around 2.88 for short and intermediate times and an increase to 3 for long times. The inset shows that this increase happens as χ_4 peaks and from the discussion of the volume distribution above, I know that the peak is accompanied by the emergence of a system spanning cluster. Since such a cluster has the dimensionality of the simulation box, the increase

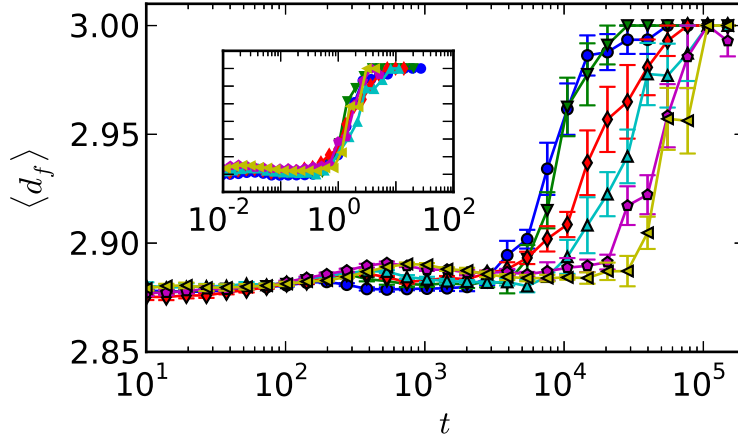


Figure 4.12: Main panel shows the mean fractal dimension of the hop clusters over time for six ages, see legend in fig. 4.7. The inset shows data collapse when time is rescaled by the time of the χ_4 peak.

to $d_f = 3$ is not surprising and it is clearly a finite size effect. Therefore, the found value of $\langle d_f \rangle = 2.88$ agrees remarkably well with the above mentioned result that was solely based on four-point correlators.

4.3 Conclusions

The microscopic structural relaxation is studied in quiescent polymer glasses at three temperatures in the aging regime. A refined version of a detection algorithm initially introduced by Candelier et al. [19] was used to measure the relaxation events defined as particle hops everywhere in the system and on-the-fly for the full duration of the simulation. An evaluation of the distribution of persistence times, hop distance, and hop autocorrelation at three temperatures showed good agreement with previous studies that used other methods [97, 98]. Since the detection algorithm allows hop detection for the full system, I was able to directly analyze the spatio-temporal density-density correlation between relaxation events. A strong correlation was observed between near-simultaneous hops of neighboring particles, which indicates cooperative motion of groups of particles. I estimated correlation ranges and used these to analyze the size of the collaborative rearrangements as a function of temperature and age. I found distributions that first have an exponen-

4.3. Conclusions

tial shape and then transition over to a power-law tail that becomes flatter during aging. An increase in temperature broadened the power law, and this trend connects well to the power-law distributions seen by Candelier et al. [19] in agitated granular media, where a very similar definition for the rearranging groups was used. An earlier study of a binary LJ-glass in the aging regime on the other hand showed power-law distributions [96], both for various temperatures and ages. I believe that this disagreement is due to the very different hop-time resolution, that was about three orders of magnitude smaller than what was used in this work.

In the second part of this study, I compared the standard χ_4 measure of dynamical heterogeneity (DH) with a direct geometric analysis of hop clusters, which gives a spatially resolved picture to complement the bulk averaged χ_4 . My results show that χ_4 reaches its peak when a single dominating cluster is developed that extends throughout the system and is accompanied by mostly single-cage-sized pockets of inactive particles. I also observed a delayed cluster aggregation in older glasses that mirrored the shift of the χ_4 peaks towards larger times with increasing age. Therefore, the geometric formation of DH is continuously slowed but otherwise unchanged by physical aging. We furthermore observed increasing χ_4 peak heights, which indicate a growing dynamical correlation range during aging. Both the shift of χ_4 with increasing age and the increasing χ_4 peak height were also reported by Parsaeian and Castillo [71] in simulations of a binary LJ mixture. Recently, further evidence for growing dynamical correlations was obtained via experimental measurements of the nonlinear dielectric susceptibility in glycerol by Brun et al. [17]. Parsaeian and Castillo also identified a power-law scaling between an estimated growing correlation range and the χ_4 -peak height, which is connected to the total correlated volume. I showed that this scaling is in excellent agreement with the fractal dimension of the hop clusters. The mean cluster volume did not directly reveal the aging correlation range, as it is not proportional to χ_4 in the range of its peak, yet a clear age dependence was observed for the maximal number of clusters and inactive regions (holes).

The shape of the evolving distribution of hop cluster volumes helps to understand the somewhat surprising success of mean-field models of aging. Despite the presence of heterogeneous dynamics, aging continuous time random walk descriptions [98] based on the trap model of aging [67] are very successful in capturing the evolution of mean squared displacements, dynamical structure factors and van Hove functions while entirely neglecting DH. My measurements of the cluster volume distribution prior to the merging

4.3. *Conclusions*

into a single dominating cluster (fig. 4.11) showed a power-law form with exponent ≤ -2 . This observation indicates that fluctuations in the size of the DH are sufficiently small that average quantities such as mean cluster size do not behave anomalously.

Chapter 5

Soft modes predict structural relaxation³

This third project investigates the link between heterogeneous dynamics (DH) and local structure in polymer glasses. In other words, which structural feature determines whether the particles in a certain region are dynamically active and undergo substantial rearrangements, while other regions are structurally static? Recent studies [63, 102] indicate that so called soft modes, low energy vibrational modes in disordered solids that are spatially localized, could provide the key to answering this question, and section 1.2.4 discusses soft modes in great detail.

So far, quantitative evidence for the correlation between soft modes and structural rearrangements is restricted to studies of model metallic glasses in 2D under deformation [63, 81]. This project quantifies the correlation in a 3D polymer glass in the quiescent state and I investigate temperature and age dependence. Participation of particles in soft modes is measured in the form of a softness field and the definition as well as implementation details are given in section 2.7. I use the force-shifted model potential discussed in section 2.1, since differentiable forces are required for the calculation of the Hessian. The Hessian is used to find the low-energy vibrational spectrum and I use a system size of $N = 10,000$ for numerical efficiency. Structural rearrangements are measured as irreversible hops as discussed in section 2.6.

In addition to the spatial correlation of softness field and hops, the direction of hops is found to directly correlate to the direction of soft modes. I furthermore quantify the lifetime of the softness field and compare it to time scales of structural relaxation. Two glasses are investigated in the aging regime, at temperatures $T = 0.2, 0.3$, and one system at $T = 0.4$. At this latter temperature, the relaxation times are short enough so that the system reached equilibrium shortly after the quench and it is therefore a supercooled liquid. To evaluate aging effects, I analyzed the glass at $T = 0.3$ at three

³Large parts of this chapter have been published in ref. [86]

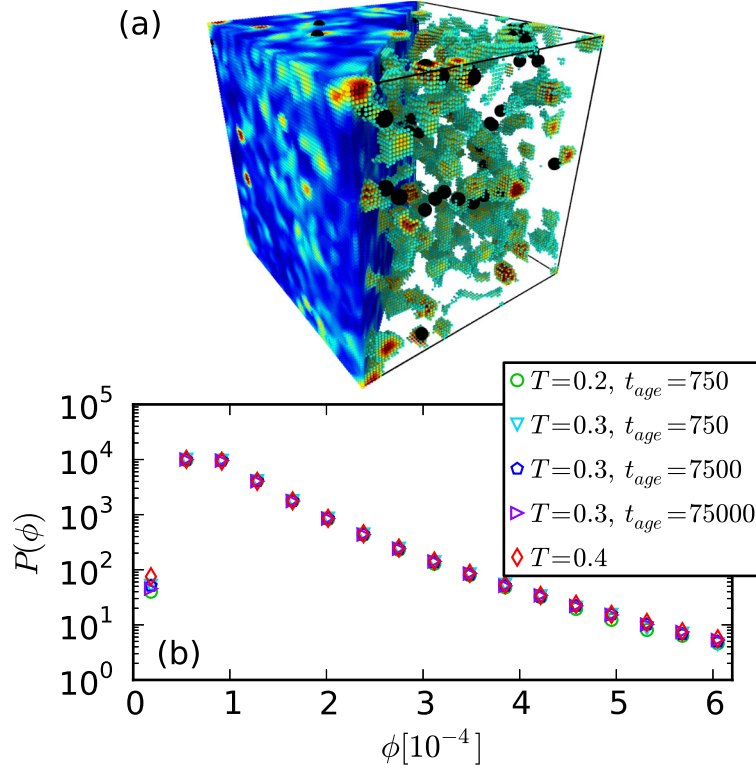


Figure 5.1: (a) Snapshot of the softness field. The right side shows only the 10% softest regions and the solid black spheres (size equals particles) indicate the first 100 hopping particles detected after the measurement of the softness field. (b) Distribution of the softness field for three temperatures and three ages. Error bars are omitted and smaller than the symbols.

ages: $t_{age} = 7.5 \cdot 10^2, 7.5 \cdot 10^3, 7.5 \cdot 10^4$. The results shown below are averaged over 20 realizations of each system with independent initial configurations and error bars indicate the standard error.

5.1 Softness field

In fig. 5.1(a) I show an example snapshot of the softness field. One can clearly see the heterogeneous spatial distribution of soft regions across the simulation box. The black spheres are the first 100 hopping particles detected

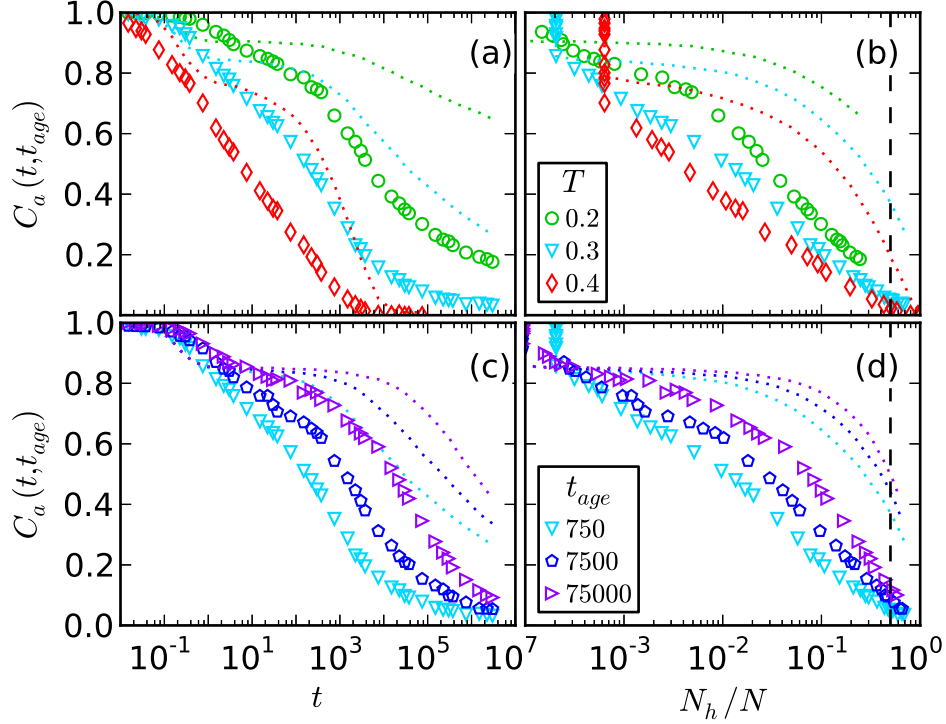


Figure 5.2: Autocorrelation of the softness field for three temperatures (a-b) and three ages (c-d). Panel (a)[(c)] shows C_a as function of time, and the dotted lines indicate the ISF for the same temperatures [ages]. Panel (b)[(d)] shows C_a as function of number of hopped particles N_h , with dotted lines again indicating the ISF and dashed lines mark when 50% of the system has hopped. Error bars are omitted and smaller than the symbols.

immediately after the measurement of the softness field, and some overlap is visible between hops and soft areas. The following sections are dedicated to a quantitative analysis of this correlation, yet I first focus on characteristics of the softness field itself. Fig. 5.1(b) shows the softness distribution in the entire polymer sample for different temperatures and ages. I find that the distributions feature a strong peak at small values and a rapid, yet slower than exponential decay. The results show that the structural heterogeneity is remarkably similar for all studied systems.

In order for the softness field ϕ to represent the molecular structure in terms of “soft” and “hard” or stable and unstable regions, the lifetime of

5.1. Softness field

ϕ must be of order of the structural lifetime. I measure the lifetime of the softness field via the decay of its autocorrelation function

$$C_a(t, t_{age}) = \left\langle \frac{[\phi(t_{age}) - \bar{\phi}(t_{age})] [\phi(t_{age} + t) - \bar{\phi}(t_{age} + t)]}{\sigma_{\phi(t_{age})} \sigma_{\phi(t_{age} + t)}} \right\rangle$$

Here, the average is over all particles, $\sigma_{\phi(t)}$ is the standard deviation of the softness field $\phi(t)$, and $\bar{\phi}(t)$ is its average. In fig. 5.2 I show the autocorrelation for three temperatures (a-b) and three ages (c-d). All systems in the glass state exhibit an initial plateau in the ballistic regime, followed at intermediate times by a shoulder that becomes more pronounced at lower temperature and with increasing age. The final decay to zero has stretched exponential form and the autocorrelation reaches over many orders of magnitude in time. These characteristics are also found in the self-intermediate scattering function (ISF)

$$C_q^S(t, t_{age}) = \langle \exp [i\mathbf{q} \cdot (\mathbf{r}_j(t_{age} + t) - \mathbf{r}_j(t_{age}))] \rangle ,$$

which is the standard measure of structural lifetime [41]. Here, the average is over all particles and I use $\mathbf{q} = (0, 0, 2\pi)$. A value of $C_q^S(t, t_{age})$ close to zero means that most particles have moved further than their diameter away from their initial position. In fig. 5.2(a),c the ISFs are indicated as dotted lines, and I observe two main differences when compared to C_a : First, the plateau and associated shoulder of the ISF are more pronounced and reach further in time. Second, the ISF decays to zero at later times than the autocorrelation.

Before these differences are discussed in detail, I clarify the role of temperature and age on the autocorrelation of the softness field: Panel 5.2(a) shows that the decay-time becomes larger with decreasing temperature, as C_a shifts to the right. This is accompanied by the development of a shoulder at intermediate times, which is not present in the supercooled state ($T = 0.4$) but develops as the system becomes more glassy. This mimics the temperature dependence of the ISF, although a shoulder is already present in the supercooled state. In panel 5.2(b) I show how much of the system has undergone rearrangements as C_a decays by re-parametrizing time in terms of the fraction of particles that have hopped at least once. I observe that complete decorrelation of ϕ occurs for $T = 0.3, 0.4$ after $\gtrsim 50\%$ of particles have rearranged, and extrapolation suggests that this also holds true for $T = 0.2$. Panel 5.2(c) shows the autocorrelation for three ages at $T = 0.3$. I observe

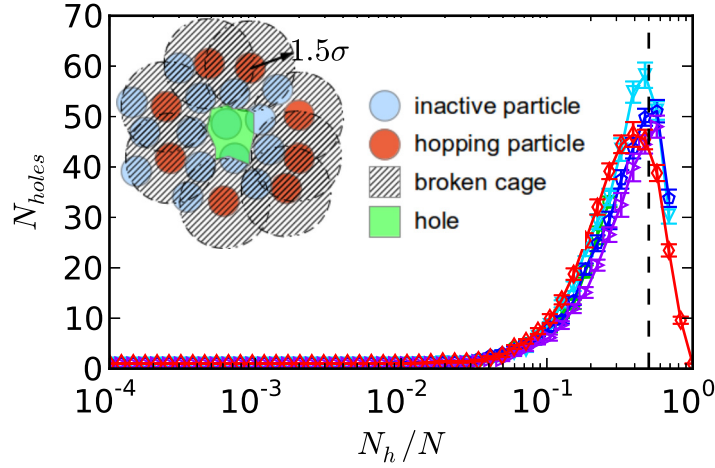


Figure 5.3: Number of holes as a function of the fraction of hopped particles. The sketch illustrates the definition of a hole: a continuous volume (green) that is surrounded by the union of spheres that approximates the cages that hopping particles have escaped and are “broken”. The dashed line indicates 50% of the system has undergone rearrangements, and the solid lines are guides to the eye. See fig. 5.1 for a legend.

that an increase in age results in a shift of C_a towards larger times via lengthening of the shoulder. The ISFs are shown as dotted lines and one can see a similar shift with increasing age. In panel 5.2(d) one can see that total decorrelation of ϕ again occurs when $\gtrsim 50\%$ of the system has undergone rearrangements, independent of the glass age.

A key difference between autocorrelation C_a and ISF is that the decorrelation of the softness field begins as soon as particles hop, whereas the ISF remains at a high value for much longer. However, this is not surprising, since the ISF can only change after a substantial part of the particles has moved. The structurally soft regions on the other hand may very well only require a few hops to transition into a more stable local configuration, which could explain the faster decay of C_a at intermediate times. It is also important to realize that the mean hop distance is of order half a particle diameter, while with a wavevector magnitude $q = 2\pi$ the ISF is sensitive to displacements of order one particle diameter. A particle therefore has to undergo multiple relaxation events to fully decorrelate the ISF, and in this sense the ISF decay provides an upper bound on the structural relaxation time.

Why does the softness field decorrelate after $\gtrsim 50\%$ of particles have hopped? To answer this question, I first note that a particle that hops by escaping its own local cage changes the local configuration of all the neighboring particles at the same time. To measure how much of the system has been affected by hops in this way, I place a sphere around each hopping particle with radius 1.5σ . This distance is the position of the first peak in the pair correlation function and the sphere therefore approximates the cage around each hopping particle. I then count the number of unconnected holes in the union of all spheres. The sketch in fig. 5.3 visualizes this: a hole is a continuous volume that is not part of any of the cages that are “broken” by the hopping particles. In the main panel of fig. 5.3 I show the number of holes as function of the fraction of hopped particles. When only a few particles have hopped, then there is only a single hole. As more particles hop, the spheres form clusters [85], interconnect and eventually percolate, leading to a subdivision into many holes. A maximum is reached when the probability of splitting a hole in two by including an additional sphere is equal to the likelihood of destroying a hole. In other words, the maximum is reached when the size of the holes is of the order of single cages. I find that this transition occurs when $\sim 50\%$ of the particles have hopped (indicated by the dashed line). At this time the total volume of the holes has dropped to $\sim 5\%$ of the system size. Therefore, the decorrelation of the softness field at $\gtrsim 50\%$ coincides with the change of the local configuration of nearly all particles.

5.2 Spatial correlation

In fig. 5.1(a) I show hops as black spheres together with the softness field, and one can see that hops appear at the center of soft regions as well as in the space between them. Before analyzing the overlap of individual hops with the softness field, I focus on the DH of the whole system. How well does a single measurement of a softness field reflect the distribution of regions with high/low rearrangement activity? I create a map of DH by accumulating hop events in a binary list h_i of all particles. The map changes as the time-window $[t_{age}, t_{age} + t]$ of included hops grows. The similarity of DH and the softness field is then quantified with the cross-correlation

$$C_{DH}(t, t_{age}) = \frac{\sum_{i=1}^N (h_i(t, t_{age}) - \bar{h}(t, t_{age})) (\phi_i(t_{age}) - \bar{\phi}(t_{age}))}{N\sigma_h\sigma_\phi}. \quad (5.1)$$

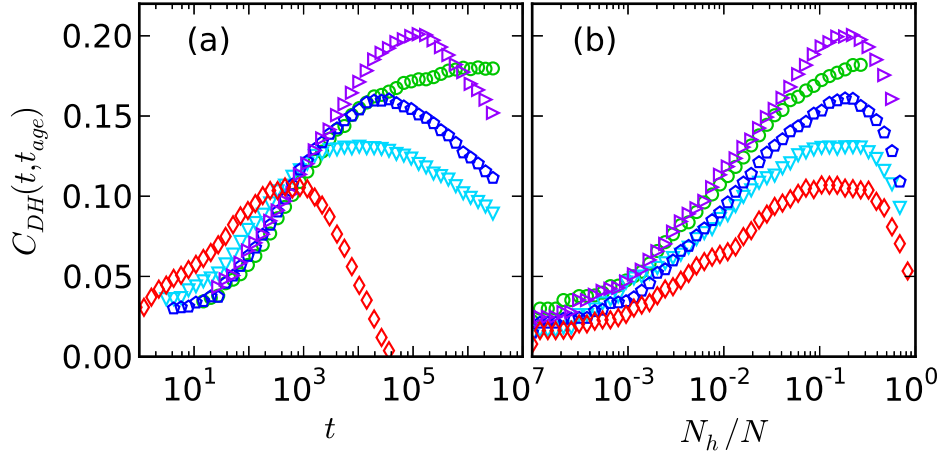


Figure 5.4: Cross-correlation between softness field and cumulative map of hopped particles (a) as function of time and (b) as function of number of hopped particles. See fig. 5.1 for a legend, and error bars are omitted and are smaller than the symbols.

Here \bar{h} , $\bar{\phi}$ are averaged over all particles and σ_h , σ_ϕ are standard deviations. In fig. 5.4(a) I show the cross-correlation as a function of elapsed time after the ϕ measurement. A maximum is observed at times that grow with increasing age and decreasing temperature. The re-parametrization in terms of number of hopped particles in fig. 5.4(b) collapses the maxima at $\sim 20\%$ rearrangement of the system. The degree of agreement is given by the maximum value of the correlation, ranging from 0.11 for the supercooled system to 0.21 for the oldest glass at $T = 0.3$. The absolute value of the correlation is not very high, which can be expected from thermal systems. Simulations in the iso-configurational (IC) ensemble [101] reduce the impact of kinetics on the map of DH by averaging over many realizations of a single configuration with randomly assigned velocity distributions. I performed such an analysis on a single configuration of the system $T = 0.3, t_{age} = 75000$ and found a cross-correlation between the softness field and $\langle h_i \rangle_{IC}$ that is twice as strong at the peak. A systematic analysis using this technique, however, is beyond the scope of the present study.

The temperature and age dependence reveal the importance of the soft modes especially in the glass state. The increase of C_{DH} with age shows that the non-equilibrium state is important for the link between structure

5.2. Spatial correlation

and dynamics. From the perspective of the potential energy landscape [43] (PEL): As the glass moves down the PEL towards more arrested, lower energy configurations, the soft modes increasingly dominate the dynamics of the glass. In the supercooled state I observe a lower correlation, indicating that higher temperature increasingly washes out the effect of structural heterogeneity defined by the soft modes. A lower temperature therefore yields a higher correlation. For the investigated temperature and age range both effects are of comparable magnitude. The largest correlation was observed in the oldest $T = 0.3$ glass, which was aged for two orders of magnitude longer than the $T = 0.2$ glass.

In fig. 5.5 I show two approaches that quantify the spatial correlation of relaxation events and softness field in greater detail: panel 5.5(a) shows the probability for a particle of given softness to undergo a hop at times immediately after the ϕ measurement, rescaled by the total hop probability

$$\Omega(\phi) = \frac{N_h(\phi)}{N(\phi)} \frac{\int d\phi N(\phi)}{\int d\phi N_h(\phi)}.$$

Here $N(\phi)$ indicates the number of particles with given softness and $N_h(\phi)$ is the subset of those particles that have hopped at least once. I observe a clear increase of the hop probability with increasing softness for all temperatures and ages. Starting from a value below one at very low ϕ (hard region), the probability monotonically rises to a saturation plateau of up to 7 times the average probability of relaxation events. The correlation is temperature dependent, being much more pronounced in the aging regime ($T = 0.2, 0.3$) than in the supercooled system ($T = 0.4$), where the soft regions undergo rearrangements with three times the average probability. Furthermore, increased age yields a stronger correlation between soft modes and relaxation events.

I explore an alternative view on the spatial correlation by binarizing the softness field into a soft spot map, where the fraction of particles f with largest softness are assigned a softness of $\phi_i^{(b)} = 1$ and all other particles have a softness of zero. I then define the predictive success rate Θ of a softness field as the fraction of the first $N_h = 100$ hopping particles that are part of a soft spot, or

$$\Theta(f) = \frac{\sum_{i=1}^N \phi_i^{(b)} h_i}{N_h}$$

with $h_i = 1$ if particle i is one of the first N_h particles to hop after the measurement of the softness field, and $h_i = 0$ otherwise.

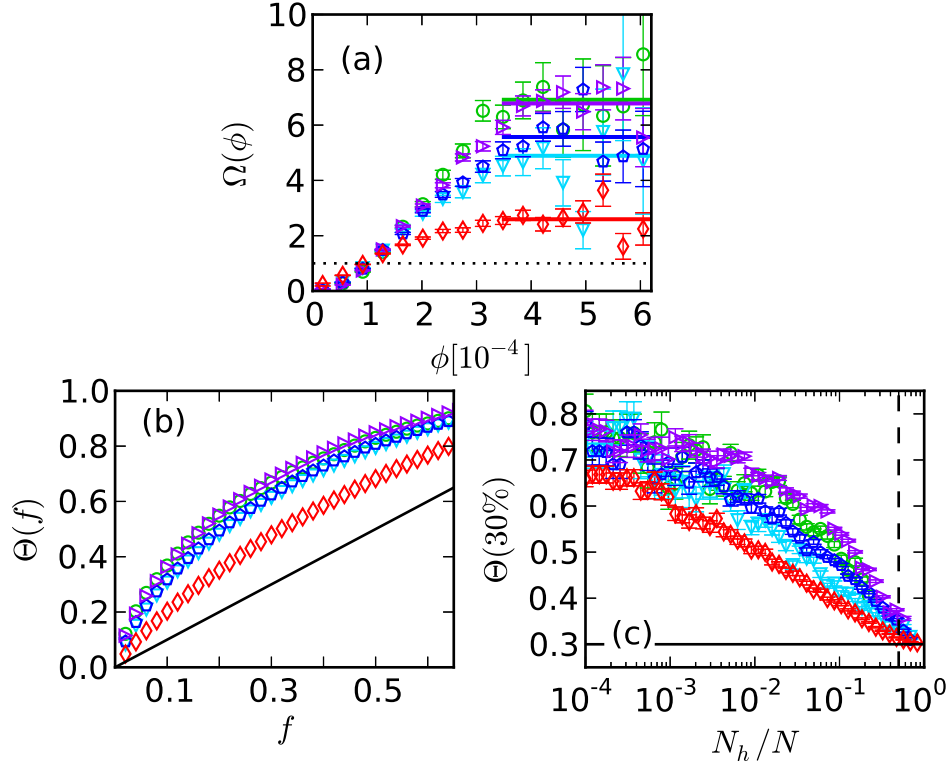


Figure 5.5: (a) Probability of a particle to hop as function of its softness, rescaled by the average hop probability. The solid lines indicate the averaged saturation probability and the dotted line is a guide to the eye. Success rate of predicting hops to occur in the softest regions of the system Θ (b) as function of coverage fraction of the softest region f and (c) as function of time rescaled to the number of hopped particles at constant coverage fraction of $f = 30\%$. The solid lines in (b,c) indicate the success rate based on randomly chosen regions and the dashed line indicates 50% of the system has undergone rearrangements. To evaluate (a) and (b) the first 100 (1%) hopping particles after the softness field measurement were used. See fig. 5.1 for legend, and error bars are omitted when smaller than symbols.

Panel 5.5(b) shows the predictive success rate as function of the coverage fraction and a comparison with a randomly chosen subset of the system as soft spots is indicated by the solid line. Clearly, the softness field is a much better predictor, with the absolute difference being maximal at around 30% coverage fraction. Here, up to 70% of the first 100 hopping particles are predicted. Again, I find that systems at lower temperature show a stronger correlation and that increasing age also improves the predictive strength of the softness field. In panel 5.5(c) I show how the spatial correlation develops as a function of time between the ϕ measurement and hops, i.e., the predictive success rate for 30% coverage fraction. Time is rescaled in terms of the number of particles that have hopped at least once, identical to the rescaling in fig. 5.2 and fig. 5.4. The correlation is long-lived, decays logarithmically and decorrelates only when $\gtrsim 50\%$ of the system has undergone structural relaxation events.

5.3 Directional correlation

The direction of the softness field, which is the average direction of the soft modes, contains information about the *dynamics* of the relaxation events. More precisely, the direction of the hops align with the direction of the softness field in soft regions. I quantify this correlation via the second Legendre polynomial

$$C_d = \left\langle \frac{3}{2} \left(\hat{\mathbf{d}} \cdot \mathbf{e}_\phi \right)^2 - \frac{1}{2} \right\rangle ,$$

where $\hat{\mathbf{d}} = (\mathbf{r}_{final} - \mathbf{r}_{init})/|\mathbf{r}_{final} - \mathbf{r}_{init}|$ is the unit vector between final and initial position of a hopping particle, and \mathbf{e}_ϕ is the direction of the softness field for the same particle (see section 2.7). The average is taken over all hopping particles. A value of $C_d = 1$ means full alignment of hop and softness field direction, while $C_d = 0$ indicates that a random orientation with respect to each other. In fig. 5.6(a) I show the correlation immediately after the measurement of ϕ as function of softness. The alignment grows with increasing ϕ for all temperatures and ages until a saturation plateau is reached. Similar to the spatial correlation discussed above, increased temperature weakens the link between the soft modes and the hops. The saturation value reaches from 0.4 for the supercooled system to 0.8 for the glass at $T = 0.2$, indicating that hops in soft regions are nearly perfectly aligned with the softness field direction at low temperatures. The effect of aging, however, seems to

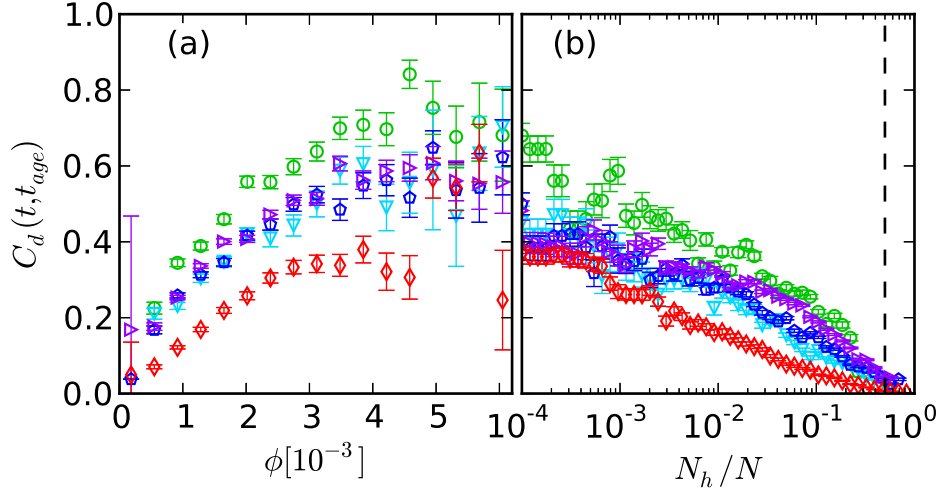


Figure 5.6: Directional correlation between softness field and hops (a) as function of softness and (b) as function of time rescaled to the number of hopped particles. The dashed line indicates 50% of the system has undergone rearrangements and the hop direction is measured as the vector between initial and final position of the particle. To evaluate (a) the first 100 (1%) hopping particles after the softness field measurement were used. See fig. 5.1 for a legend.

be negligible for the strength of the directional correlation. This behavior is qualitatively different from the age-dependent spatial correlation, which grows with increasing age. Our finding implies that the direction of molecular relaxation events is independent of the position on the PEL, because the latter is changed during aging. In other words, the non-equilibrium nature of the glass has no direct impact on the alignment of soft modes and hops. Temperature on the other hand acts as noise and reduces the degree of alignment.

In panel 5.6(b) I show the mean directional correlation as function of number of hopped particles since the measurement of ϕ . I observe a slow logarithmic decay of the correlation that vanishes only after $\gtrsim 50\%$ of the system has hopped at least once, for all temperatures and ages. A close inspection reveals that at increased age, the decay curve develops a small shoulder around 1%–10% hopped particles. This behavior does not indicate a direct age-dependence, but rather is a consequence of the longevity of

the softness field itself. The autocorrelation data discussed in section 5.1 shows how aging leads to an increased stability of ϕ in the range of $< 50\%$ hopped particles. The decay curves for the directional correlation reflect this longevity, showing that the softness field direction has predictive strength over the direction of hops until the local configuration of nearly all particles has changed.

5.4 Conclusions

The correlation between soft modes and structural relaxation events was quantified in a quiescent polymer glass at two temperatures below T_g in the aging regime and one temperature above T_g in the supercooled regime. One system in the aging regime was analyzed at three ages and I identified the impact of temperature as well as aging on the correlation. The structural relaxation events were identified as hops in the particle trajectories, and the participation of particles in soft modes is quantified in terms of a *softness field* ϕ , which was constructed from a superposition of low energy vibrational eigenmodes [102]. The softness field is closely related to the binary soft spot approach introduced by Manning and Liu [63], but here the sole adjustable parameter is the number of included modes.

For all temperatures and ages the softness field was found to be heterogeneous, with small regions of large softness. I showed that a strong correlation exists between the softness of a particle and its likelihood of undergoing a structural relaxation event. Starting from a much decreased probability at small ϕ , I found that with growing softness the hop probability increases to up to 7 times the average value. The spatial correlation is stronger at lower temperature and also grows with increasing age. I showed that a binary soft spot map based on ϕ with 30% coverage fraction predicts up to 75% of the hops immediately following the ϕ -measurement. The predictive strength was found to decrease slowly with increasing time separation between ϕ -measurement and hops. The correlation vanishes for all temperatures and ages only after $\gtrsim 50\%$ of the polymer glass has undergone rearrangements, which coincides with the decay of the softness autocorrelation function. The softness field and the binarized soft spots that can be derived from it are therefore long lived features that capture the heterogeneity of the amorphous structure.

In addition to the *spatial* correlation of hops to soft regions in the glass,

5.4. Conclusions

I showed that the soft modes also correlate to the dynamics of relaxation events. The *direction* of hops, measured as displacement vector between initial and final position of the particle, are correlated to the soft mode directions. I find an increasing alignment with increasing softness that reaches values of 70% for the lowest temperature glass. The correlation is again stronger at lower temperature, yet it appears to be independent of the glass age. An older soft spot will attract more hops and hence has a larger spatial correlation than a younger soft spot, but hops actually occurring on a soft spot follow the soft directions independent of age.

The findings are in good quantitative agreement with a recent study [81] on a sheared 2D binary mixture at finite temperature. This study found rearrangements to be 2-3 times more probable at soft spots than at random locations. A detailed analysis of the individual soft spot dynamics showed that they are robust structures that reach lifetimes of up to the bulk structural relaxation time scale, which agrees with my analysis of the ϕ autocorrelation function. In the driven systems, there is a closer relationship between self-intermediate scattering function and soft spot decay as in the present quiescent case. This may be due to extremely long local persistence times which here are not bound by an imposed external drive. Both spatial and directional correlations were furthermore identified in a recent study [77] that investigated the role of soft modes at the crossover between ordered to disordered systems. Soft modes were observed to predict the direction and location of rearrangements in a hierarchy of systems: from a crystal with a single dislocation, to a polycrystal and a binary glass in 2D.

Chapter 6

Soft modes and local plastic events during deformation

In this final project, I extend the analysis of the correlation between soft modes and particle rearrangements to polymer glasses under deformation. The previous chapter verified a strong correlation in the quiescent state, and discussed temperature- as well as age-dependence. For the case of mechanically driven systems, this link between local structure and plastic events was only quantified in metallic glasses in 2D [63, 81]. These studies showed that local plastic deformation is concentrated at so called soft spots, which are defined from a binarized superposition of quasi-localized soft modes.

This project focuses on two questions: First, do soft modes predict the location and direction of individual plastic events during mechanical deformation in polymer glasses? In analogy to the methods used in chapter 5, plastic events are measured as irreversible particle hops using the detection algorithm introduced in section 2.6, and I use the softness field definition given in section 2.7 to measure the participation of particles in soft modes. Uniaxial tensile deformation is simulated at a constant strain rate and I analyze the correlation at different stages during the deformation.

Second, does the correlation quantitatively change with the extent of the deformation, and is this change in agreement with the concept of mechanical rejuvenation? From the study presented in the last chapter, it is known that the spatial correlation between softness field and hops increases during aging. Furthermore, the analysis in chapter 3 showed that mechanical deformation in the pre-yield regime leads to a transient rejuvenation of the system in terms of dynamical as well as structural quantities, which becomes a permanent erasure of history at around the yield point. In this project, I first age a glass at $T = 0.3$ in the quiescent state for a time $7.5 \cdot 10^6$ and it is then deformed using the constant strain rate protocol discussed in section 2.3 at a rate $\dot{\epsilon} = 10^{-5}$. The deformation ends at a final engineering strain of $\epsilon = \Delta l_z / l_0 = 4$, with Δl_z being the change in the simulation box length

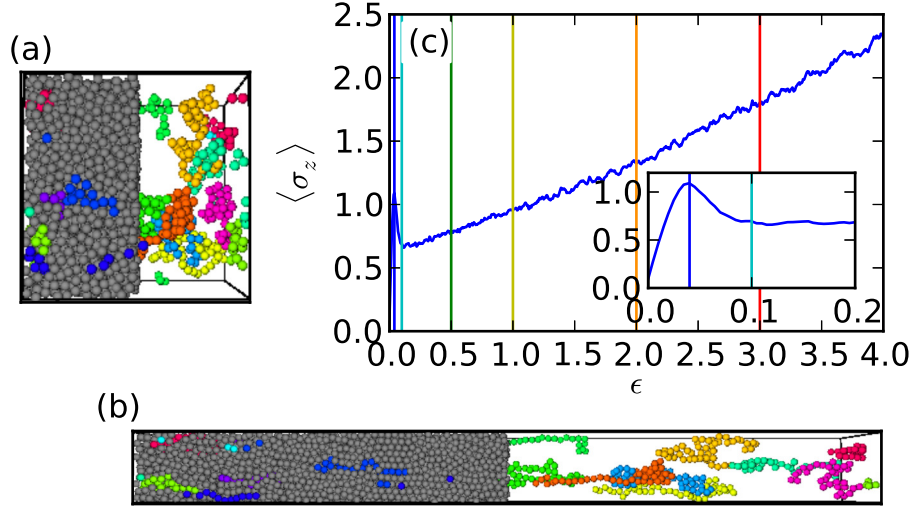


Figure 6.1: Snapshots of the system are shown at beginning (a) and end (b) of the deformation. To better visualize polymer configurations, 15 polymers are colored separately and only beads that belong to these polymers are displayed on the right side of the simulation box. (c) Stress along the deformation axis as function of total strain. Vertical colored lines indicate the investigated deformation states $\epsilon = 0.0, 0.04, 0.1, 0.5, 1.0, 2.0, 3.0, 4.0$ and the inset shows the peak at the yield point in more detail.

along the deformation axis and l_0 is the box length before the deformation. All results shown below are averages of 20 independent simulation runs and I use the force-shifted model potential discussed in section 2.1 to ensure that the forces are differentiable, which is required for the calculation of the Hessian. In analogy to the study discussed in chapter 5 I use a system size of $N = 10,000$ for numerical efficiency.

The snapshots in fig. 6.1 show the system at the beginning (a) and end (b) of the deformation. In fig.6.1(c) I show the stress along the deformation axis as function of total engineering strain. The deformation is separated into three regimes: After an elastic deformation at very small strains, the stress reaches a maximum at the yield strain $\epsilon = 0.04$ (see inset). This is followed by a strain softening regime, where the stress decreases until at $\epsilon \sim 0.1$ a plateau is reached and the stress remains constant until $\epsilon = 0.2$. At this

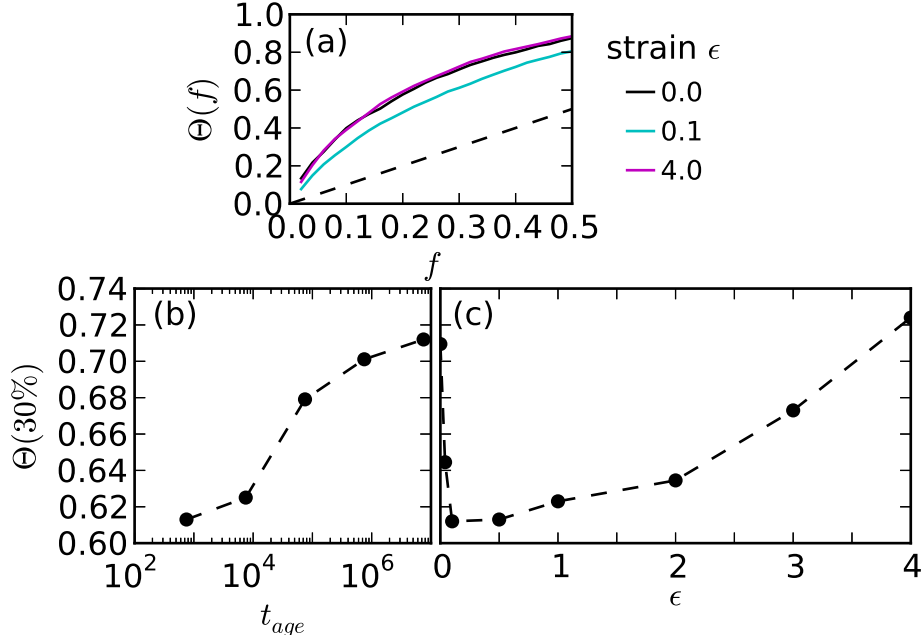


Figure 6.2: (a) Fraction of hops in soft spots as function of the coverage fraction of soft spots measured in three deformation regimes: elastic ($\epsilon = 0.0$), strain softening ($\epsilon = 0.1$), and strain hardening ($\epsilon = 4.0$). The dashed line indicates no correlation. The evolution of the predictive success rate reached at $f = 0.3$ is shown during aging (b) and during deformation (c) - the dashed lines are guides to the eye.

point, the stress starts to increase with strain, a polymeric effect known as strain hardening, and at the end of the deformation at $\epsilon = 4.0$ the stress has increased to about twice the yield stress.

6.1 Correlation between hops and softness field

The spatial correlation between softness field and hops is quantified as the predictive success rate Θ that is also used in chapter 5. Here, the softness field is binarized into a soft spot map by assigning a softness of one to the fraction f of particles with largest softness and zero to the other particles. I

6.1. Correlation between hops and softness field

then calculate the fraction of the first $N_h = 100$ hopping particles that are part of a soft spot, or

$$\Theta(f) = \frac{\sum_{i=1}^N \phi_i^{(b)} h_i}{N_h}$$

with $h_i = 1$ if particle i is one of the first N_h particles to hop after the measurement of the softness field, and $h_i = 0$ otherwise.

Figure 6.2(a) shows the predictive success rate measured at three different strains during the deformation, and the dashed line indicates Θ for randomly distributed soft spots (no correlation). For all deformation regimes, I find a positive correlation between softness field and the occurrence of hops. Compared to the strong correlation in the elastic regime, measured immediately upon loading at $\epsilon = 0.0$, the correlation is decreased in the post-yield strain softening regime at $\epsilon = 0.1$. Interestingly, however, in the strain hardening regime at $\epsilon = 4.0$ the correlation is again at a value comparable to the elastic regime.

I furthermore calculated the directional correlation between softness field and hops (not shown) in analogy to the analysis presented in section 5.3. I find that the alignment found in the quiescent state is also present during deformation and that it is unchanged by the extent of the deformation.

To explain the striking change in the spatial correlation, from decrease in the pre-yield and strain softening regime to an increase in the strain hardening regime, I first compare to the evolution of the correlation during aging. To simplify the analysis I focus on the predictive success rate at a coverage fraction of 30%. This is the fraction where the difference between measured Θ and uncorrelated value (dashed line) is maximal. In fig. 6.2(b) I show $\Theta(30\%)$ at five ages. In agreement with the results reported in chapter 5, the correlation increases from 0.61 to 0.71 as the age grows by four orders of magnitude. The position in the potential energy landscape (PEL), which is changed in the direction of lower minima during aging, therefore plays an important role for the spatial correlation of soft modes and hops. Panel (c) shows the predictive success rate measured at different points during the deformation. One can see that the spatial correlation in the elastic regime at $\epsilon = 0$ is roughly equal to the value found in the quiescent state immediately prior to the deformation. At the yield strain $\epsilon = 0.04$ the correlation has decreased to 0.64 and at the end of the strain softening regime ($\epsilon = 0.1$) $\Theta(30\%)$ has reached the pre-aging value 0.61. This reversal of the aging effects is consistent with the picture of mechanical rejuvenation, which is

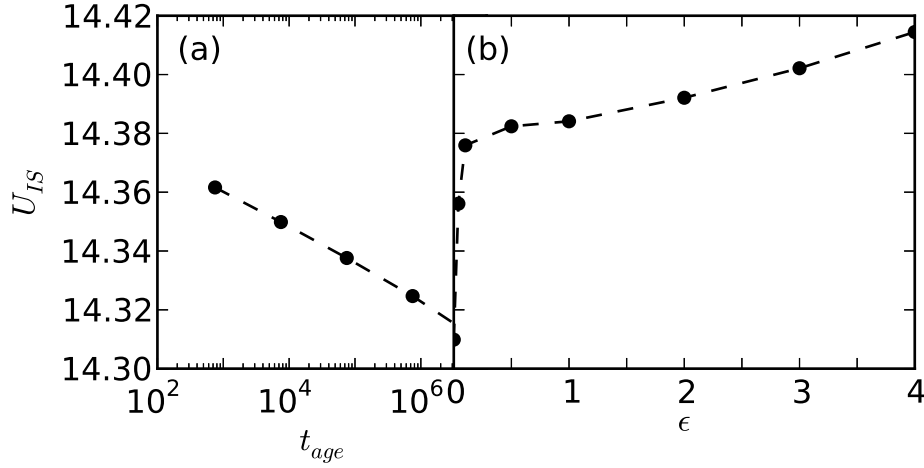


Figure 6.3: Mean inherent structure energy during aging (a) and (b) as function of strain during deformation.

discussed in much detail in chapter 3.

Interestingly, the spatial correlation does not remain constant upon further deformation in the strain hardening regime. Figure 6.2(c) shows that $\Theta(30\%)$ monotonically increases with growing strain. The increase in $\Theta(30\%)$ accelerates at large strains $\epsilon > 2$, reaching a value of 0.72 at $\epsilon = 4.$, which is above the predictive success rate measured in the quiescent state prior to the deformation. Is this strengthening spatial correlation the result of the same processes that drive the increase during aging?

6.2 Examining the strain hardening regime

Aging is the non-equilibrium evolution of the system towards lower energy states in the PEL, and it is discussed in detail in section 1.2.2. The position in the PEL can be measured by minimizing the energy in the zero temperature limit. The particle configuration at the minimum is called the inherent structure, and its potential energy U_{IS} , previously introduced in section 3.4, is measured during the calculation of the softness field. In fig. 6.3 I show the mean total inherent structure energy, the summation of pair and bond potential energy averaged over all particles, during aging [panel (a)] and mechanical deformation [panel (b)]. As expected, panel (a) shows that U_{IS} decreases logarithmically during aging. Other than the predictive success

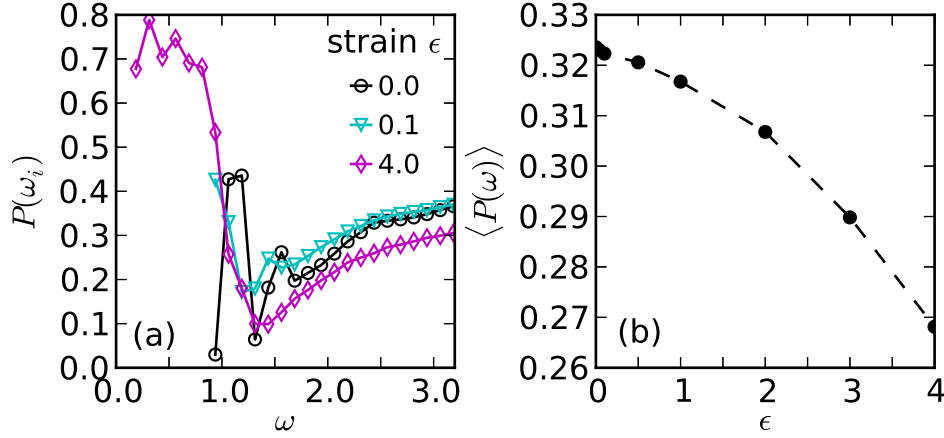


Figure 6.4: (a) Mean participation ratio as function of eigenfrequency. (b) Mean participation ratio of all N_m modes used for the softness field calculation as function of total engineering strain.

rate Θ , which depends on the first $N_h = 100$ hops after the softness field measurement, the inherent structure is an instantaneous quantity, and U_{IS} at time of loading ($\epsilon = 0.0$) is therefore identical to the quiescent state just prior to loading. At the yield strain, $\epsilon = 0.04$, U_{IS} has increased nearly to pre-aging values, and in the strain softening regime, $\epsilon = 0.1$, the increase of U_{IS} slows and full erasure of history (mechanical rejuvenation) is reached. Importantly, in the strain hardening regime, the inherent structure energy is found to increase with the extent of the deformation. In the PEL picture, this evolution is in the opposite direction than that occurring during aging, and “over-aging” can therefore not be the reason for the increase in spatial correlation.

To better understand why the softness field correlates more strongly with hops at large strain deformation, I investigate changes in the low energy vibrational spectrum, which is the basis for the softness field calculation. The extent of localization of a vibrational mode j can be calculated as participation ratio

$$P_j = \frac{\left(\sum_{i=1}^N (\mathbf{e}_j^{(i)})^2 \right)^2}{N \sum_{i=1}^N (\mathbf{e}_j^{(i)})^4}.$$

Here, $\mathbf{e}_j^{(i)}$ is the polarization vector of particle i , see also section 1.2.4. A

value of $P_j = 1$ means that all particles are participating equally in mode j , whereas a small value indicates that the mode is quasi-localized around a few active particles.

In fig. 6.4(a) I show the participation ratio $P(\omega)$ as function of mode frequency. Since the vibrational spectrum is a feature of the inherent structure, $P(\omega)$ at $\epsilon = 0.0$ is identical to that in the quiescent state at the same age. The participation ratios at the end of the strain softening regime ($\epsilon = 0.1$) are nearly unchanged, with a slight shift of the extended modes (large participation ratio) towards smaller frequencies. In the strain hardening regime at $\epsilon = 4.0$, the vibrational spectrum has changed in two ways: First, I find modes with large participation ratio at much smaller frequencies. This change is due to the large (400%) elongation of the simulation box along the deformation axis, which allows modes with larger wavelength to “fit” into the simulation volume. The participation ratios of these modes suggest that they are extended and do not scatter at the structurally weak regions in the glass. Second, the participation ratios of the modes near the boson peak $\omega \sim 2.0$ (see discussion in section 1.2.4) is *reduced* compared to the undeformed system. In fig. 6.4(b) I show the average participation ratio $\langle P(\omega) \rangle$ of all $N_m = 600$ modes used for the calculation of the softness field. In the strain hardening regime I find a reduction of the average participation ratio, indicating that the soft modes become more localized as the deformation grows. In the elastic and strain softening regime $\langle P(\omega) \rangle$ is nearly constant, which is also the behavior observed during aging (not shown).

The increase in predictive success rate in the strain hardening regime is well correlated with the decrease of the average participation ratio. To show this, I calculate the relative change of these quantities in the strain range $0.1 \leq \epsilon \leq 4.0$. For a measured quantity $O(\epsilon)$ the relative change is defined as

$$\Delta O(\epsilon) = \frac{O(\epsilon) - O(\epsilon = 0.1)}{O(\epsilon = 4.0) - O(\epsilon = 0.1)}.$$

In fig. 6.5 I compare the relative change of predictive success rate $\Theta(30\%)$ (black) and average participation ratio $\langle P(\omega) \rangle$ (red) in the strain hardening regime. Definition and scaling of the relative change sets the value at $\epsilon = 0.1$ to zero, while the final value at $\epsilon = 4.0$ is set to one. The spatial correlation increases slowly at smaller strains and more rapidly at larger strains. This increase is closely tracked by the change in the participation ratio. Localized (low participation ratio) soft modes, as discussed in more detail in section 1.2.4, are caused by the scattering of phonons at structurally weak

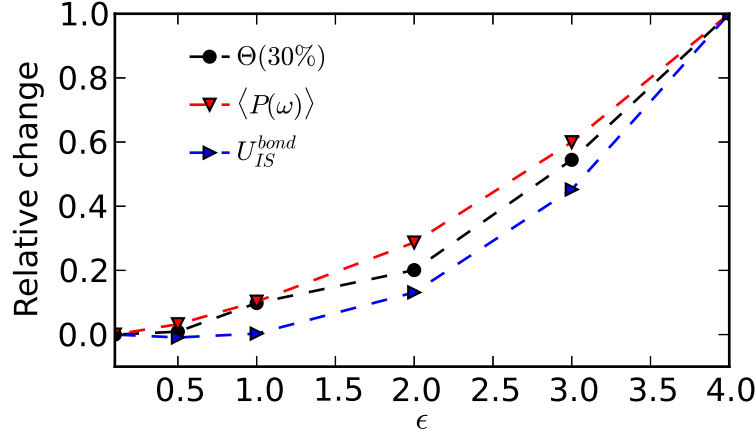


Figure 6.5: Relative change observed during deformation in the strain hardening regime. Lines are guides to the eye.

regions. That more strongly localized soft modes lead to a better predictive strength of the softness field is therefore not surprising. However, the interesting question must be: What process drives the increase of localization in the strain hardening regime?

Strain hardening is a polymeric effect, where elastic energy is stored in the covalent bond interaction along the polymer backbone. The stored energy increases with growing strain, which leads to larger external stresses. In fig. 6.5 I also show the relative change of the average covalent bond energy (blue) during strain hardening, calculated from the inherent structure. The bond energy is near constant until $\epsilon = 1.0$ and then increases more and more rapidly with growing strains. The evolution matches the behavior of participation ratio and predictive strength reasonably well, and there is a clear correlation between all three quantities. This correlation suggests that the process responsible for the increase in spatial correlation of softness field and hops might indeed be tied to the polymeric nature of the glass.

A known process that is present during the deformation of polymer glasses is the alignment of polymers along the deformation axis [32]. The extent of alignment can be calculated by projecting the bond orientations, that is the unit length vector connecting two bonded particles, on the deformation axis and averaging over all bonds in the system. I monitored the alignment of the polymer with the deformation axis over the full deformation (not shown) and

found that it does *not* correlate to the data shown in fig. 6.5. The polymer alignment starts to increase from zero immediately upon loading and grows most rapidly in the elastic and strain softening regime. It then continuously slows until reaching a value of 0.6 at strain $\epsilon = 4.0$ (zero means no correlation and one indicates full alignment). In addition to this, I investigated anisotropy effects in the softness field direction and hop direction during strain hardening, yet both quantities remain isotropically distributed.

6.3 Conclusions

The correlation between soft modes and local plastic events is quantified for a well aged polymer glass under uniaxial tensile deformation. A constant strain rate protocol was used and the correlation is analyzed at various points of the deformation: in the elastic regime, at the yield strain, during strain softening and far into the strain hardening regime with a maximum engineering strain of $\epsilon = 4.0$. The plastic events were monitored as hops in the particle trajectories, and the participation of particles in soft modes is quantified as a superposition of low energy vibrational eigenmodes [102] in a scalar softness field. The mean soft mode direction was calculated from a weighted average of the eigenvectors [86].

At all points of the deformation, I find a strong spatial correlation between large softness of a particle and the occurrence of plastic events. The correlation is quantified as the overlap between a binarized soft spot map [63, 81] of the softest particles with the occurrence of hops immediately after the softness measurement. At a coverage fraction of 30% soft spots, the location of 71% of hops is predicted immediately after loading in the elastic regime. The overlap decreases to 61% after yield in the strain softening regime. In the following strain hardening regime the overlap *increases*, and at a strain of $\epsilon = 4.0$ it has reached a value of 72%, indicating that the correlation has become stronger than in the pre-deformation polymer glass. In agreement with the results in chapter 5, I find that the direction of hops is well aligned with the direction of the soft modes in the soft spots, and deformation did not alter this directional correlation.

The study discussed in chapter 5 and published in ref. [86] showed that aging increases the spatial correlation of soft modes and particle hops. This study measured the increase in the overlap of soft spots and hops in the aging period prior to the deformation, and I directly show that the decrease

during deformation in the elastic and strain softening regime fully reverses the impact of prior aging. This erasure of history indicates mechanical rejuvenation and the results are consistent with the more detailed study of mechanical rejuvenation in polymer glasses discussed in chapter 3 and published in ref. [84].

I showed that the increase of overlap between soft spots and hops in the strain hardening regime is accompanied by a growing localization of the soft modes. I furthermore showed that this localization is correlated to the increase of elastic energy stored in the covalent bonds of the polymers. This is an indication for a polymeric effect, tied to the chain-topology of the polymer glass. However, what process is driving the localization could not be clearly identified from the gathered data. The alignment of polymers with the deformation axis [32] was found to not correlate to the increase in localization and no indications for anisotropy in the softness field direction or hop direction were found in the strain hardening regime. It is also possible that the increase in correlation is merely due to the change in box geometry during deformation, which as discussed above alters the vibrational spectrum. Resolving this question requires further study.

Chapter 7

Conclusions

The research presented in this thesis aims at creating a better understanding of the physical processes that govern plasticity in polymer glasses. Although a large amount of research has explored the physics of glasses [5, 12, 25, 35, 88], the challenge remains to connect the macroscopic effects of mechanical deformation with microscopic scale processes that are prevalent in glassy matter. This thesis uses large scale molecular dynamics simulations of a well known bead-spring polymer model [52] with documented glass forming capabilities [8, 38, 70, 76, 94, 99] to investigate key aspects of glassy physics in the industrially important case of polymer glass and to bridge the gap from microscopic scale to macroscopic plasticity. In four projects I studied physical aging, mechanical rejuvenation, dynamical heterogeneity and soft modes as the link between heterogeneous dynamics and local structure both in the quiescent state and during deformation.

The first project explored mechanical rejuvenation using bulk-averaged quantities that simultaneously captured the dynamical, structural and energetic state of post-deformation polymer glasses, which are compared to systems without deformation history. A key technical contribution of this work is the development of an effective algorithm for the detection of individual structural relaxation events called hops. The detection method was first used to spatially resolve dynamical heterogeneity in the second project. Building on these results, maps of hop events were then used to investigate signature features in the local structure of regions that undergo rearrangements in quiescent polymer glasses. Subsequently, the analysis was extended to mechanically deformed systems to study the structural origin of local plastic events. This link between local structure and plastic events was furthermore found to be sensitive to physical aging as well as to mechanical perturbation, substantiating the results on mechanical rejuvenation found using bulk-averaged quantities.

Mechanical rejuvenation The non-equilibrium nature of the glass drives a continuous evolution towards lower energy states, which causes an increase in yield stress as well as brittleness of polymer glasses with increasing age [88]. Mechanical deformation can reverse the impacts of physical aging, an effect known as mechanical rejuvenation [88]. Whether deformation and aging are indeed directly coupled is a matter of scientific controversy [64] with one central question: Is the state that the glassy system is driven into by mechanical deformation indeed comparable to the state of a younger glass? In a recent series of experiments Lee and Ediger showed that the molecular mobility, which decreases during aging, is increased after the application of mechanical stresses [57, 59]. Measurements in the recovery regime after the deformation, however, revealed two different impacts [58]: After deformation at a small stress amplitude, the molecular mobility quickly recovered its pre-deformation value, while the application of a much larger stress amplitude permanently altered the mobility and the system evolved in the recovery regime comparable to a younger glass without deformation history.

The study discussed in chapter 3 and published in ref. [84] was designed to complement these results with an experimentally inaccessible perspective of the evolution in the recovery regime (recovery path) by simultaneously monitoring the structural α -relaxation time, inherent structure energy and measures of local spatial order. In agreement with the experiment, my results show that after weak deformation in the pre-yield regime the recovery path returns to the aging behavior of an undeformed polymer glass of equal age. The perturbation of the recovery path becomes stronger with increasing total strain at the end of the deformation and the history of the polymer glass is permanently erased at around the yield strain. Here, structural, dynamical and energetic perspectives indicate a recovery path that is comparable with the aging behavior of a younger glass, i.e. permanent mechanical rejuvenation. After deformation in the post-yield regime, however, the three perspectives on the recovery path yield different indications on mechanical rejuvenation: While the α -relaxation time is consistent with that of a younger glass, the structural and energetic quantities reveal that the deformed system is driven into a state that is distinct from a quiescent polymer glass of any age. This observation supports the view of McKenna [64] that mechanical deformation does not only reset the internal clock of a glass, but that it can drive the system to a new thermodynamic state.

Furthermore, my results discussed in chapter 6 give an additional perspective on mechanical rejuvenation: The correlation between local plastic

events and soft modes was found to be sensitive to aging as well as mechanical perturbation. The correlation became stronger during aging, yet deformation up to the end of the strain softening regime resulted in a reset of the correlation to pre-aging values, indicating mechanical rejuvenation of this link between local structure and dynamics.

My results for the pre- and post-yield deformation therefore resolve the question of mechanical rejuvenation in the following sense: Mechanical deformation around the yield-point leads to a permanently altered glass state that is comparable to a younger glass without deformation history. If the deformation is limited to the elastic regime prior to the yield point, the system state is only transiently altered and the glass recovers quickly to the pre-deformation state. Deformation in the post-yield regime, beyond the end of strain softening as indicated by the results discussed in chapter 6, drives the glass to a new state that is structurally and energetically distinct from a younger glass without deformation history. My results furthermore show that, in the limit of no aging in the deformation period, the impact of deformation on the recovery path is controlled solely by the total engineering strain at the end of the deformation. This finding supports an earlier study [100] that reports the importance of strain in describing accelerated dynamics during deformation. It would be interesting to further explore the role of strain as deformation parameter, because it could provide more insight into the key components for models of plasticity in polymer glasses [25, 37].

Dynamical heterogeneity in the aging regime One of the defining characteristics of glassy physics is the emergence of dynamical heterogeneity (DH) near the glass transition [9, 24, 28, 34, 47, 51, 53]. In the glass state particle rearrangements are correlated on the molecular level, leading to cooperative motion of groups of particles [33, 51] and the partition of the system into transient regions of “faster” and “slower” structural relaxation. The study of DH has been concentrated on supercooled liquids, yet it is clearly important in understanding plasticity in polymer glasses. Recent studies that quantify DH via three- and four-point correlators indicate that dynamical correlation is increasing during physical aging [17, 71].

In the second project, discussed in chapter 4 and published in ref. [85], I analyzed the spatio-temporal distribution of structural relaxation in quiescent polymer glasses at various temperatures and ages. Relaxation events were detected as hops in the particle trajectories and I introduced an adap-

tation of an algorithm by Candelier et al. [19]. This detection algorithm is a key technical contribution of this thesis, because it allows the measurement of relaxation events with high spatio-temporal resolution on-the-fly for the full duration of the simulation. The technique allowed me to calculate the spatio-temporal density-density correlation and I found a strong correlation between near-simultaneous hops of neighboring particles. A cluster analysis was used to measure the size of cooperatively moving groups of particles, and I found an exponential distribution with power-law tail that becomes less pronounced during aging and at lower temperatures. The latter trend connects well with results for agitated granular media [19].

I furthermore used the map of relaxation events to spatially resolve DH as hop clusters, and I compare their growth and volume distribution with the simultaneously measured four-point dynamical susceptibility χ_4 as the standard measure of DH [9, 53]. In agreement with a study of a model metallic glass [71], I find a growing maximal dynamical correlation with increasing age that is shifted towards larger time scales during aging. A cluster analysis showed that the time of maximal correlation coincides with the formation of a single hop cluster that encompasses nearly the whole system, with only single cage sized pockets of particles that have not undergone structural rearrangements. The cluster volume distribution prior to the merging into a single dominating cluster follows a power-law with exponent -2 , which indicates that fluctuations are sufficiently small so that averaged quantities do not behave anomalously. This result helps explain the success of mean-field models of aging [98], which capture the evolution of dynamical quantities like the mean squared displacement while entirely neglecting DH.

I introduced an efficient hop detection algorithm, that allowed me to give a new perspective on dynamical heterogeneity by simultaneously measuring DH using the established dynamical susceptibility measure as well as the aggregation of hops into mesoscopic clusters. For the first time, I measured growing dynamical correlation and shift towards larger time scales during physical aging in a polymer glass, confirming recent results for model binary glasses. The time of maximal correlation was found to coincide with the formation of a single system spanning cluster of hops with only single-cage sized regions that did not undergo structural relaxation.

Link between local structure and particle rearrangements A key open challenge in developing a theory of plasticity in glasses is to understand

the link between the location of particle rearrangements and the local structure. Which structural feature determines the spatial distribution of DH and distinguishes regions with rapid structural relaxation from quasi-stable local configurations of particles? The goal of this inquiry is to find a coarse grained structural description for amorphous solids in the spirit of dislocations of crystalline solids. Recently, quasi-localized low energy vibrational modes have attracted much attention as a possible candidate [102, 103], and a strong correlation was quantified between these soft modes and particle rearrangements in a mechanically driven model metallic glass in 2D and at zero temperature [63]. My third and fourth projects were dedicated to verify this correlation in a thermal, three-dimensional polymer glass in the quiescent state and during mechanical deformation. Structural relaxation events, or elementary plastic events in the case of deformation, were spatio-temporally resolved as particle hops using the detection algorithm developed in the second project, and I used a simple superposition scheme to construct a softness field from the low energy vibrational spectrum [102].

In the third project, discussed in chapter 5 and published in ref. [86], I studied the correlation between softness field and hops in the quiescent state at three temperatures and during physical aging. My results show that hops occur up to 7 times more often than average in the softest regions of the system. This indicates a strong spatial correlation that increases during aging and decreases at higher temperatures. I furthermore found a strong directional alignment of hops in these soft regions with the mean direction of soft modes. These findings support a very recent study that investigated the role of soft modes at the crossover between ordered to disordered systems [77]. Soft modes were observed to predict the direction and location of rearrangements in a hierarchy of systems: from a crystal with a single dislocation, to a polycrystal and a binary glass in 2D. My analysis of the softness field autocorrelation showed that soft modes are long-lived structural features compared to vibrational time scales, and the autocorrelation only decays to zero when nearly the entire system has undergone structural relaxation. A very recent study of a sheared, thermal model binary glass in 2D supports this finding by tracking the lifetime of individual soft regions, called soft spots [81]. The study showed that the lifetime is correlated to the structural relaxation time and that individual soft spots can survive many individual rearrangements.

The final project, discussed in chapter 6, quantified the correlation in an aged polymer glass under uniaxial tensile deformation at various points of

the deformation. Measurements were analogous to the study of the quiescent case, and I verified the spatial and directional correlation of soft modes and hops in all deformation regimes. Interestingly, the spatial correlation, which increased during the aging period prior to the deformation, was found to decrease to the pre-aging value when the deformation reached the strain softening regime. This finding showed that the link between structure and dynamics in glasses is sensitive to mechanical rejuvenation as discussed in the first project. Monitoring of the position in the PEL confirmed this connection: After a decrease of the inherent structure energy during aging, the system was driven back towards higher energies by the deformation and the pre-aging value was reached in the strain softening regime, simultaneously with the resetting of the spatial correlation.

Measuring the correlation of soft modes and hops during deformation in the strain hardening regime revealed a novel effect with a link to the chain connectivity in polymer glasses: The spatial correlation was found to increase with increasing strain, reaching values higher than observed just prior to the deformation at a strain of $\epsilon = 4$. The increase in spatial correlation was shown to be tied with a growing localization of the soft modes as well as with the increase in potential energy stored in the covalent bonds, which is the mechanism causing strain hardening. The latter link suggests a polymeric origin of the effect. However, the orientation of polymers along the deformation axis did not correlate to the increase in localization, nor did I find anisotropies in the softness field direction or hop direction during the deformation.

My results show a strong link between quasi-localized soft modes and the location of particle rearrangements. For the first time, this correlation was quantified in a polymer glass and I studied the impact of temperature, physical aging as well as mechanical deformation. Beyond the spatial correlation I also showed that the direction of individual rearrangements are aligned with the polarization of the soft modes. Finally, I showed that the structural information encoded in the soft modes is long-lived compared to the vibrational time scale and that the correlations fully decay on the order of the structural relaxation time.

Outlook A growing body of research is indicating that soft modes are indeed linking irreversible rearrangements, plasticity and microscopic structure in amorphous solids. Evidence has been found in a diverse set of model sys-

tems mostly in 2D, and this thesis adds quantitative evidence in 3D: From binary supercooled liquids in the quiescent state [44, 102, 103], sheared binary glasses at zero temperature [63, 68, 90] and finite temperature [81], to polycrystals [77], lattice models [3] and the present quiescent as well as deformed polymer glass. Various measures for rearrangements have been used, ranging from the change of nearest neighbors [102], to maxima in the non-affine displacement field [81], and here hops in individual particle trajectories. Moreover, soft modes were quantified in different ways: correlations to rearrangements were identified w.r.t. individual modes [90], the binary soft spot field [63] and the superposition of participation fractions [102] used here.

A recent study used information theory to directly measure the extent of correlation between soft modes and the propensity of motion [49], which is the part of the particle motion that is determined by the structure alone and that can be isolated by averaging in the iso-configurational ensemble [13, 101]. The study quantified the difference between joined probability distribution of soft modes and propensity of motion and the factorized distribution (independent variables hypothesis), with a large difference indicating a strong correlation. Not surprisingly, the difference was maximal when the propensity was measured in a time interval on the order of the vibrational time scale and it decreased with increasing interval size. However, a significant difference was still present at time intervals of the order of the structural relaxation time proving that a correlation exists. Despite these variations in simulated models and analysis, the robustness of the correlation suggests that soft spots should play a prominent role in theories of plasticity for amorphous solids in general, and the practically important case of polymer glasses in particular.

A second approach to understand the cause of dynamical heterogeneity in amorphous solids has developed around the discovery of heterogeneously distributed local elastic moduli [66, 70, 91, 106]. Regions of small shear moduli were found to be prone to plastic rearrangements, whereas areas with high moduli tend to be more structurally stable. Both approaches are closely related as they are harmonic theories and some work has been done to understand the link between them [31]. It would be interesting to further explore the relationship between soft modes and local elastic moduli, and directly analyze both spatial distributions. Do soft spots indeed have a small shear modulus, and are the decay timescales of the heterogeneous distributions related?

The softness field analysis during deformation in the strain hardening

regime revealed a growing spatial correlation of hops to soft modes during strain hardening. Clearly identifying the process responsible for this increase is an interesting question emerging from this thesis and should be the topic of future work. To answer this question, it would be instrumental to understand the true cause for the increase in localization of the vibrational modes. Strain hardening introduces a stiffening of the polymer backbones, and it would be interesting to investigate more closely how this affects the vibrational modes. One possibility would be to model an amorphous solid as a random network of springs and to study the vibrational modes while increasing the stiffness of springs that are oriented along one dimension. Another possible avenue would be to investigate whether strain hardening has an impact on the distance to the glass transition in terms of molecular mobility. The third project showed that the spatial correlation is increasing with decreasing temperature, i.e. the correlation is stronger deep in the glass state, where the molecular mobility is very low. Does the stiffening of the polymer backbone lead to a slowing of molecular mobility? A fruitful starting point of a future study could be to measure the non-affine displacement, which excludes the displacement introduced by the change of the simulation box shape, and to compare it at different points during deformation in the strain hardening regime.

Recently, Fielding et al. [37] proposed a simple model that explains the impact of deformation-induced flow on the structural relaxation time in polymer glasses. The key idea is to separate relaxation events caused by the elastic energy stored in covalent bonds from those that relax the elastic field of neighboring but non-bonded monomers. This separation of “polymeric” and “solvent” degrees of freedom leads to a competition between these relaxation types during flow. The solvent relaxes on smaller time scales and increases the energy in the covalent bonds, until this forces polymeric relaxation events. It would be interesting to verify such an interplay in polymer glasses that are more complex than the dumbbell systems that were analyzed by the above authors. The hop detection technique could be instrumental in such an analysis.

Bibliography

- [1] M. Aichele, Y. Gebremichael, F. W. Starr, J. Baschnagel, and S. C. Glotzer. Polymer-specific effects of bulk relaxation and stringlike correlated motion in the dynamics of a supercooled polymer melt. *J. Chem. Phys.*, 119(10):5290–5304, September 2003.
- [2] Michael P. Allen and Dominic J. Tildesley. *Computer Simulation of Liquids*. Oxford University Press, 1989.
- [3] D. J. Ashton and J. P. Garrahan. Relationship between vibrations and dynamical heterogeneity in a model glass former: Extended soft modes but local relaxation. *The European Physical Journal E*, 30(3):303–307, November 2009.
- [4] Rolf Auhl, Ralf Everaers, Gary S. Grest, Kurt Kremer, and Steven J. Plimpton. Equilibration of long chain polymer melts in computer simulations. *J. Chem. Phys.*, 119:12718, 2003.
- [5] Jean-Louis Barrat. *Slow Relaxations and nonequilibrium dynamics in condensed matter*. Springer, August 2003.
- [6] U. Bengtzelius, W. Gotze, and A. Sjolander. Dynamics of supercooled liquids and the glass transition. *J. Phys. C: Solid State Phys.*, 17(33):5915, November 1984.
- [7] Christoph Bennemann, Claudio Donati, Jörg Baschnagel, and Sharon C. Glotzer. Growing range of correlated motion in a polymer melt on cooling towards the glass transition. *Nature*, 399(6733):246–249, May 1999.
- [8] Christoph Bennemann, Wolfgang Paul, Kurt Binder, and Burkhard Dünweg. Molecular-dynamics simulations of the thermal glass transition in polymer melts: α -relaxation behavior. *Phys. Rev. E*, 57(1):843–851, January 1998.

- [9] L. Berthier, C. Biroli, J. P. Bouchaud, L. Cipelletti, D. El Masri, D. L'Hôte, F. Ladieu, and M. Pierno. Direct Experimental Evidence of a Growing Length Scale Accompanying the Glass Transition. *Science*, 310(5755):1797–1800, December 2005.
- [10] Ludovic Berthier. Dynamic Heterogeneity in Amorphous Materials. *Physics*, 4:42, May 2011.
- [11] Ludovic Berthier and Giulio Biroli. Theoretical perspective on the glass transition and amorphous materials. *Rev. Mod. Phys.*, 83(2):587–645, June 2011.
- [12] Ludovic Berthier, Giulio Biroli, Jean-Philippe Bouchaud, Luca Cipelletti, and Wim van Saarloos. *Dynamical Heterogeneities in Glasses, Colloids, and Granular Media*. Oxford University Press, July 2011.
- [13] Ludovic Berthier and Robert L. Jack. Structure and dynamics of glass formers: Predictability at large length scales. *Phys. Rev. E*, 76(4):041509, October 2007.
- [14] Kurt Binder and Walter Kob. *Glassy Materials and Disordered Solids: An Introduction to Their Statistical Mechanics*. World Scientific, January 2011.
- [15] Erik Bitzek, Pekka Koskinen, Franz Gähler, Michael Moseler, and Peter Gumbsch. Structural Relaxation Made Simple. *Phys. Rev. Lett.*, 97(17):170201, October 2006.
- [16] Carolina Brito and Matthieu Wyart. Heterogeneous dynamics, marginal stability and soft modes in hard sphere glasses. *J. Stat. Mech.*, 2007(08):L08003, August 2007.
- [17] C. Brun, F. Ladieu, D. L'Hôte, G. Biroli, and J-P. Bouchaud. Evidence of Growing Spatial Correlations during the Aging of Glassy Glycerol. *Phys. Rev. Lett.*, 109(17):175702, October 2012.
- [18] U. Buchenau, C. Pecharroman, R. Zorn, and B. Frick. Neutron Scattering Evidence for Localized Soft Modes in Amorphous Polymers. *Phys. Rev. Lett.*, 77(4):659–662, July 1996.

- [19] R. Candelier, O. Dauchot, and G. Biroli. Building Blocks of Dynamical Heterogeneities in Dense Granular Media. *Phys. Rev. Lett.*, 102(8):088001, February 2009.
- [20] R. Candelier, O. Dauchot, and G. Biroli. Dynamical facilitation decreases when approaching the granular glass transition. *EPL*, 92(2):24003, October 2010.
- [21] R. Candelier, A. Widmer-Cooper, J. K. Kummerfeld, O. Dauchot, G. Biroli, P. Harrowell, and D. R. Reichman. Spatiotemporal Hierarchy of Relaxation Events, Dynamical Heterogeneities, and Structural Reorganization in a Supercooled Liquid. *Phys. Rev. Lett.*, 105(13):135702, September 2010.
- [22] Franco M. Capaldi, Mary C. Boyce, and Gregory C. Rutledge. Enhanced Mobility Accompanies the Active Deformation of a Glassy Amorphous Polymer. *Phys. Rev. Lett.*, 89(17):175505, October 2002.
- [23] David Chandler and Juan P. Garrahan. Dynamics on the Way to Forming Glass: Bubbles in Space-Time. *Annual Review of Physical Chemistry*, 61(1):191–217, 2010.
- [24] Pinaki Chaudhuri, Ludovic Berthier, and Walter Kob. Universal Nature of Particle Displacements close to Glass and Jamming Transitions. *Phys. Rev. Lett.*, 99(6):060604, August 2007.
- [25] K. Chen, E. J. Saltzman, and K. S. Schweizer. Segmental dynamics in polymers: from cold melts to ageing and stressed glasses. *J. Phys.: Condens. Matter*, 21(50):503101, December 2009.
- [26] Kang Chen and Kenneth S. Schweizer. Molecular Theory of Physical Aging in Polymer Glasses. *Phys. Rev. Lett.*, 98(16):167802, April 2007.
- [27] Ke Chen, M. L. Manning, Peter J. Yunker, Wouter G. Ellenbroek, Zexin Zhang, Andrea J. Liu, and A. G. Yodh. Measurement of Correlations between Low-Frequency Vibrational Modes and Particle Rearrangements in Quasi-Two-Dimensional Colloidal Glasses. *Phys. Rev. Lett.*, 107(10):108301, August 2011.
- [28] Luca Cipelletti and Laurence Ramos. Slow dynamics in glassy soft matter. *J. Phys.: Condens. Matter*, 17(6):R253, February 2005.

- [29] P. G. de Gennes. Reptation of a Polymer Chain in the Presence of Fixed Obstacles. *The Journal of Chemical Physics*, 55(2):572–579, July 1971.
- [30] Pablo G. Debenedetti and Frank H. Stillinger. Supercooled liquids and the glass transition. *Nature*, 410(6825):259–267, March 2001.
- [31] P. M. Derlet, R. Maaß, and J. F. Löffler. The Boson peak of model glass systems and its relation to atomic structure. *Eur. Phys. J. B*, 85(5):1–20, May 2012.
- [32] M. Doi. *The theory of polymer dynamics*. Clarendon Press ; Oxford University Press, Oxford [Oxfordshire] : New York, 1986.
- [33] Claudio Donati, Jack F. Douglas, Walter Kob, Steven J. Plimpton, Peter H. Poole, and Sharon C. Glotzer. Stringlike Cooperative Motion in a Supercooled Liquid. *Phys. Rev. Lett.*, 80(11):2338–2341, March 1998.
- [34] M. D. Ediger. Spatially heterogeneous dynamics in supercooled liquids. *Annu. Rev. Phys. Chem.*, 51(1):99–128, October 2000.
- [35] M. D. Ediger and Peter Harrowell. Perspective: Supercooled liquids and glasses. *The Journal of Chemical Physics*, 137(8):080901–080901–15, August 2012.
- [36] Kenneth Falconer. *Fractal Geometry: Mathematical Foundations and Applications*. John Wiley & Sons, December 2007.
- [37] S. M. Fielding, R. G. Larson, and M. E. Cates. Simple Model for the Deformation-Induced Relaxation of Glassy Polymers. *Phys. Rev. Lett.*, 108(4):048301, January 2012.
- [38] Ting Ge and Mark O. Robbins. Anisotropic plasticity and chain orientation in polymer glasses. *J. Polym. Sci. Part B*, 48(13):1473–1482, 2010.
- [39] Wolfgang Goetze. *Complex Dynamics of Glass-Forming Liquids*. Oxford University Press, December 2008.
- [40] L.E Govaert, H.G.H van Melick, and H.E.H Meijer. Temporary toughening of polystyrene through mechanical pre-conditioning. *Polymer*, 42(3):1271–1274, February 2001.

Bibliography

- [41] Jean-Pierre Hansen and I. R. McDonald. *Theory of Simple Liquids*. Academic Press, February 2006.
- [42] O.A Hasan and M.C Boyce. Energy storage during inelastic deformation of glassy polymers. *Polymer*, 34(24):5085–5092, December 1993.
- [43] Andreas Heuer. Exploring the potential energy landscape of glass-forming systems: from inherent structures via metabasins to macroscopic transport. *Journal of Physics: Condensed Matter*, 20(37):373101, September 2008.
- [44] Glen M. Hocky and David R. Reichman. A small subset of normal modes mimics the properties of dynamical heterogeneity in a model supercooled liquid. *The Journal of Chemical Physics*, 138(12):12A537, March 2013.
- [45] William Hoover. Constant-pressure equations of motion. *Phys. Rev. A*, 34(3):2499–2500, September 1986.
- [46] William G. Hoover. Canonical dynamics: Equilibrium phase-space distributions. *Phys. Rev. A*, 31(3):1695–1697, March 1985.
- [47] M. M. Hurley and Peter Harrowell. Kinetic structure of a two-dimensional liquid. *Phys. Rev. E*, 52(2):1694–1698, August 1995.
- [48] John M. Hutchinson. Physical aging of polymers. *Progress in Polymer Science*, 20(4):703–760, 1995.
- [49] Robert L. Jack, Andrew J. Dunleavy, and C. Patrick Royall. Information-Theoretic Measurements of Coupling between Structure and Dynamics in Glass Formers. *Phys. Rev. Lett.*, 113(9):095703, August 2014.
- [50] Walter Kob and Jean-Louis Barrat. Aging Effects in a Lennard-Jones Glass. *Phys. Rev. Lett.*, 78(24):4581–4584, June 1997.
- [51] Walter Kob, Claudio Donati, Steven J. Plimpton, Peter H. Poole, and Sharon C. Glotzer. Dynamical Heterogeneities in a Supercooled Lennard-Jones Liquid. *Phys. Rev. Lett.*, 79(15):2827–2830, October 1997.

- [52] Kurt Kremer and Gary S. Grest. Dynamics of entangled linear polymer melts: A molecular-dynamics simulation. *J. Chem. Phys.*, 92:5057, 1990.
- [53] N. Lačević, F. W. Starr, T. B. Schröder, and S. C. Glotzer. Spatially heterogeneous dynamics investigated via a time-dependent four-point density correlation function. *J. Chem. Phys.*, 119(14):7372–7387, October 2003.
- [54] Daniel J. Lacks and Mark J. Osborne. Energy Landscape Picture of Overaging and Rejuvenation in a Sheared Glass. *Phys. Rev. Lett.*, 93(25):255501, December 2004.
- [55] Brian B. Laird and H. R. Schober. Localized low-frequency vibrational modes in a simple model glass. *Phys. Rev. Lett.*, 66(5):636–639, February 1991.
- [56] Andre Lee and Gregory B. McKenna. The physical ageing response of an epoxy glass subjected to large stresses. *Polymer*, 31(3):423–430, March 1990.
- [57] Hau-Nan Lee and M. D. Ediger. Interaction between physical aging, deformation, and segmental mobility in poly(methyl methacrylate) glasses. *The Journal of Chemical Physics*, 133:014901, 2010.
- [58] Hau-Nan Lee and M. D. Ediger. Mechanical Rejuvenation in Poly(methyl methacrylate) Glasses? Molecular Mobility after Deformation. *Macromolecules*, 43(13):5863–5873, 2010.
- [59] Hau-Nan Lee, Keewook Paeng, Stephen F. Swallen, and M. D. Ediger. Direct Measurement of Molecular Mobility in Actively Deformed Polymer Glasses. *Science*, 323(5911):231–234, January 2009.
- [60] E. Leutheusser. Dynamical model of the liquid-glass transition. *Phys. Rev. A*, 29(5):2765–2773, May 1984.
- [61] Leslie S. Loo, Robert E. Cohen, and Karen K. Gleason. Chain Mobility in the Amorphous Region of Nylon 6 Observed under Active Uniaxial Deformation. *Science*, 288(5463):116–119, April 2000.

- [62] Alexey V. Lyulin and M. A. J. Michels. Time Scales and Mechanisms of Relaxation in the Energy Landscape of Polymer Glass under Deformation: Direct Atomistic Modeling. *Phys. Rev. Lett.*, 99(8):085504, 2007.
- [63] M. L. Manning and A. J. Liu. Vibrational Modes Identify Soft Spots in a Sheared Disordered Packing. *Phys. Rev. Lett.*, 107(10):108302, August 2011.
- [64] Gregory B McKenna. Mechanical rejuvenation in polymer glasses: fact or fallacy? *Journal of Physics: Condensed Matter*, 15:S737–S763, March 2003.
- [65] Simone Melchionna, Giovanni Ciccotti, and Brad Lee Holian. Hoover NPT dynamics for systems varying in shape and size. *Molecular Physics*, 78(3):533–544, February 1993.
- [66] Hideyuki Mizuno, Stefano Mossa, and Jean-Louis Barrat. Measuring spatial distribution of the local elastic modulus in glasses. *Phys. Rev. E*, 87(4):042306, April 2013.
- [67] Cécile Monthus and Jean-Philippe Bouchaud. Models of traps and glass phenomenology. *J. Phys. A: Math. Gen.*, 29(14):3847, July 1996.
- [68] Majid Mosayebi, Patrick Ilg, Asaph Widmer-Cooper, and Emanuela Del Gado. Soft Modes and Nonaffine Rearrangements in the Inherent Structures of Supercooled Liquids. *Phys. Rev. Lett.*, 112(10):105503, March 2014.
- [69] Shūichi Nosé. A molecular dynamics method for simulations in the canonical ensemble. *Mol. Phys.*, 52(2):255–268, 1984.
- [70] George J. Papakonstantopoulos, Robert A. Riggleman, Jean-Louis Barrat, and Juan J. de Pablo. Molecular plasticity of polymeric glasses in the elastic regime. *Phys. Rev. E*, 77(4):041502, April 2008.
- [71] Azita Parsaeian and Horacio E. Castillo. Growth of spatial correlations in the aging of a simple structural glass. *Phys. Rev. E*, 78(6):060105, December 2008.

- [72] Steve Plimpton. Fast Parallel Algorithms for Short-Range Molecular Dynamics. *J. Comput. Phys.*, 117(1):1–19, March 1995.
- [73] Nikolai V. Priezjev. Heterogeneous relaxation dynamics in amorphous materials under cyclic loading. *Phys. Rev. E*, 87(5):052302, May 2013.
- [74] Robert A. Riggleman, Hau-Nan Lee, M. D. Ediger, and Juan J. de Pablo. Free Volume and Finite-Size Effects in a Polymer Glass under Stress. *Phys. Rev. Lett.*, 99(21):215501, November 2007.
- [75] Robert A. Riggleman, Kenneth S. Schweizer, and Juan J. de Pablo. Nonlinear Creep in a Polymer Glass. *Macromolecules*, 41(13):4969–4977, 2008.
- [76] Jörg Rottler and Mark O. Robbins. Shear yielding of amorphous glassy solids: Effect of temperature and strain rate. *Phys. Rev. E*, 68(1):011507, July 2003.
- [77] Jörg Rottler, Samuel S. Schoenholz, and Andrea J. Liu. Predicting plasticity with soft vibrational modes: From dislocations to glasses. *Phys. Rev. E*, 89(4):042304, April 2014.
- [78] Chris H. Rycroft. Voro++.
- [79] Maria M. Santore, Randolph S. Duran, and Gregory B. McKenna. Volume recovery in epoxy glasses subjected to torsional deformations: the question of rejuvenation. *Polymer*, 32(13):2377–2381, 1991.
- [80] H. R. Schober and C. Oligschleger. Low-frequency vibrations in a model glass. *Phys. Rev. B*, 53(17):11469–11480, May 1996.
- [81] Samuel S. Schoenholz, Andrea J. Liu, Robert A. Riggleman, and Joerg Rottler. Understanding plastic deformation in thermal glasses from single-soft-spot dynamics. *arXiv:1404.1403 [cond-mat]*, April 2014.
- [82] Yunfeng Shi and Michael L. Falk. Atomic-scale simulations of strain localization in three-dimensional model amorphous solids. *Phys. Rev. B*, 73(21):214201, June 2006.
- [83] Hiroshi Shintani and Hajime Tanaka. Universal link between the boson peak and transverse phonons in glass. *Nat Mater*, 7(11):870–877, November 2008.

- [84] Anton Smessaert and Jörg Rottler. Recovery of Polymer Glasses from Mechanical Perturbation. *Macromolecules*, 45(6):2928–2935, March 2012.
- [85] Anton Smessaert and Jörg Rottler. Distribution of local relaxation events in an aging three-dimensional glass: Spatiotemporal correlation and dynamical heterogeneity. *Phys. Rev. E*, 88(2):022314, August 2013.
- [86] Anton Smessaert and Jörg Rottler. Structural relaxation in glassy polymers predicted by soft modes: a quantitative analysis. *Soft Matter*, 10(42):8533–8541, October 2014.
- [87] D.C. Sorensen, R.B. Lehoucq, C. Yang, and K. Maschhoff. ARPACK.
- [88] L. C. E. Struik. *Physical aging in amorphous polymers and other materials*. Elsevier Scientific Pub. Co., 1978.
- [89] L. C. E. Struik. On the rejuvenation of physically aged polymers by mechanical deformation. *Polymer*, 38(16):4053–4057, August 1997.
- [90] A. Tanguy, B. Mantsi, and M. Tsamados. Vibrational modes as a predictor for plasticity in a model glass. *EPL*, 90(1):16004, April 2010.
- [91] Michel Tsamados, Anne Tanguy, Chay Goldenberg, and Jean-Louis Barrat. Local elasticity map and plasticity in a model Lennard-Jones glass. *Phys. Rev. E*, 80(2):026112, 2009.
- [92] Marcel Utz, Pablo G. Debenedetti, and Frank H. Stillinger. Atomistic Simulation of Aging and Rejuvenation in Glasses. *Phys. Rev. Lett.*, 84(7):1471–1474, February 2000.
- [93] H.G.H. van Melick, L.E. Govaert, B. Raas, W.J. Nauta, and H.E.H. Meijer. Kinetics of ageing and re-embrittlement of mechanically rejuvenated polystyrene. *Polymer*, 44(4):1171–1179, February 2003.
- [94] F. Varnik, J. Baschnagel, and K. Binder. Reduction of the glass transition temperature in polymer films: A molecular-dynamics study. *Phys. Rev. E*, 65(2):021507, January 2002.
- [95] K. Vollmayr-Lee. Single particle jumps in a binary Lennard-Jones system below the glass transition. *J. Chem. Phys.*, 121(10):4781–4794, September 2004.

- [96] K. Vollmayr-Lee and E. A. Baker. Self-organized criticality below the glass transition. *EPL*, 76(6):1130, December 2006.
- [97] Katharina Vollmayr-Lee, Robin Bjorkquist, and Landon M. Chambers. Microscopic Picture of Aging in SiO_2 . *Phys. Rev. Lett.*, 110(1):017801, January 2013.
- [98] M. Warren and J. Rottler. Atomistic mechanism of physical ageing in glassy materials. *EPL*, 88(5):58005, December 2009.
- [99] Mya Warren and Joerg Rottler. Simulations of aging and plastic deformation in polymer glasses. *Phys. Rev. E*, 76(3):031802, 2007.
- [100] Mya Warren and Joerg Rottler. Deformation-induced accelerated dynamics in polymer glasses. *J. Chem. Phys.*, 133:164513, 2010.
- [101] Asaph Widmer-Cooper, Peter Harrowell, and H. Fynewever. How Reproducible Are Dynamic Heterogeneities in a Supercooled Liquid? *Phys. Rev. Lett.*, 93(13):135701, September 2004.
- [102] Asaph Widmer-Cooper, Heidi Perry, Peter Harrowell, and David R. Reichman. Irreversible reorganization in a supercooled liquid originates from localized soft modes. *Nat Phys*, 4(9):711–715, September 2008.
- [103] Asaph Widmer-Cooper, Heidi Perry, Peter Harrowell, and David R. Reichman. Localized soft modes and the supercooled liquid’s irreversible passage through its configuration space. *The Journal of Chemical Physics*, 131(19):194508, November 2009.
- [104] N. Xu, V. Vitelli, A. J. Liu, and S. R. Nagel. Anharmonic and quasi-localized vibrations in jammed solids—Modes for mechanical failure. *EPL*, 90(5):56001, June 2010.
- [105] Ning Xu, Matthieu Wyart, Andrea J. Liu, and Sidney R. Nagel. Excess Vibrational Modes and the Boson Peak in Model Glasses. *Phys. Rev. Lett.*, 98(17):175502, April 2007.
- [106] Kenji Yoshimoto, Tushar S. Jain, Kevin Van Workum, Paul F. Nealey, and Juan J. de Pablo. Mechanical Heterogeneities in Model Polymer Glasses at Small Length Scales. *Phys. Rev. Lett.*, 93(17):175501, October 2004.